

Hydro-Mechanical-Seismological Modeling of Fluid-Induced Seismicity in Fractured Nonlinear Poroelastic Media: Theory, Implementation and Capabilities

Lei Jin¹

¹Department of Geophysics, Stanford University

November 22, 2022

Abstract

Decoupled hydro-shearing has been a decades-long paradigmatic mechanism of fluid-induced seismicity. A surging alternative is coupled hydro-mechanical triggering, largely based on the theory of linear poroelasticity. Unfortunately, seismicity source fractures and their geometric and physical alterations to a canonical poroelastic system are rarely accounted for, and seismicity is typically forecasted using a Coulomb stress rate model without producing catalogs. Here, I present a new framework for modeling fluid-induced seismicity in arbitrarily fractured nonlinear poroelastic media. The hydro-mechanical triggering is modeled using our Jin & Zoback (2017, <https://doi.org/10.1002/2017JB014892>) computational model that resolves both fracture fluid storage and nonlinear flow in addition to full poroelastic coupling. Seismological modeling is achieved stochastically by generating stress drops based on the full inter-seismic poroelastic stressing history. The two steps are sequentially coupled and advanced in time via a new prediction-correction algorithm, allowing for fracture stress updating and synthetic event catalog assembly. To demonstrate model capabilities and effects of fractures and full coupling on overpressure, stress and seismicity, I perform three microseismic-scale numerical experiments by progressively adding fractures and poroelastic coupling into a diffusion-only base model. Some previously unknown mechanisms are elucidated. In contrast to existing models, my model produces repeaters and linear clustering of seismicity. Poroelastic coupling enhances the clustering, inhibits near-field seismicity over time while increasingly favoring remote triggering, and overall significantly reduces the event population. Meanwhile, some seismic source statistical characteristics including the Gutenberg-Richter scaling relation overall remain unaffected, and the curious -value elevation for microseismicity can be attributed to a mechanical origin.

1 **Hydro-Mechanical-Seismological Modeling of Fluid-Induced Seismicity in**
2 **Fractured Nonlinear Poroelastic Media: Theory, Implementation and**
3 **Capabilities**

4 **Lei Jin^{1*}**

5 ¹Department of Geophysics, Stanford University, California 94305

6 *Corresponding to: Lei Jin (leijin@alumni.stanford.edu)

7 **Key Points**

- 8 • I consider an arbitrarily fractured, fluid-solid fully coupled and nonlinear poroelastic medium for
9 modeling induced seismicity
- 10 • I propose a new framework coupling hydro-mechanical modeling with poroelastic stress path-based
11 seismological modeling
- 12 • Three numerical experiments demonstrate model capabilities and effects of fractures and full
13 coupling on overpressure, stress and seismicity

14 **Abstract**

15 Decoupled hydro-shearing has been a decades-long paradigmatic mechanism of fluid-induced seismicity.
16 A surging alternative is coupled hydro-mechanical triggering, largely based on the theory of linear
17 poroelasticity. Unfortunately, seismicity source fractures and their geometric and physical alterations to a
18 canonical poroelastic system are rarely accounted for, and seismicity is typically forecasted using a
19 Coulomb stress rate model without producing catalogs. Here, I present a new framework for modeling
20 fluid-induced seismicity in arbitrarily fractured nonlinear poroelastic media. The hydro-mechanical
21 triggering is modeled using our [Jin & Zoback \(2017, https://doi.org/10.1002/2017JB014892\)](https://doi.org/10.1002/2017JB014892)
22 computational model that resolves both fracture fluid storage and nonlinear flow in addition to full
23 poroelastic coupling. Seismological modeling is achieved stochastically by generating stress drops based
24 on the full inter-seismic poroelastic stressing history. The two steps are sequentially coupled and
25 advanced in time via a new prediction-correction algorithm, allowing for fracture stress updating and
26 synthetic event catalog assembly. To demonstrate model capabilities and effects of fractures and full
27 coupling on overpressure, stress and seismicity, I perform three microseismic-scale numerical
28 experiments by progressively adding fractures and poroelastic coupling into a diffusion-only base model.
29 Some previously unknown mechanisms are elucidated. In contrast to existing models, my model produces
30 repeaters and linear clustering of seismicity. Poroelastic coupling enhances the clustering, inhibits near-
31 field seismicity over time while increasingly favoring remote triggering, and overall significantly reduces
32 the event population. Meanwhile, some seismic source statistical characteristics including the Gutenberg-
33 Richter scaling relation overall remain unaffected, and the curious *b*-value elevation for microseismicity
34 can be attributed to a mechanical origin.

35 **Keywords:** coupled hydro-mechanical modeling, seismological modeling, induced seismicity, fractured
36 porous media, poroelasticity, seismic source parameters

37 1. Introduction

38 Fluid perturbations (i.e., injection or withdrawal) within the subsurface alter the pore pressure and
 39 effective stress quasi-statically, inducing seismicity and dynamic stress release on certain fractures (in this
 40 study, I do not distinguish between a fracture and a fault, both defined as an arbitrarily long pre-existing
 41 permeable fluid pathway with frictional strength, and I shall use them inter-changeably). The occurrence
 42 of fluid-induced seismicity on a source fracture is due to the maximum shear stress resolved on it exceeds
 43 its static frictional strength. Adopting the classic linear Coulomb shear failure criterion, this can be
 44 summarized as

$$45 \quad CFF = |\tau_f| - \mu_s \sigma'_{nf} = \left[\|\boldsymbol{\sigma}'_f \cdot \underline{n}_f\|^2 - (\boldsymbol{\sigma}'_f : \underline{n}_f \otimes \underline{n}_f)^2 \right]^{1/2} - \mu_s (\boldsymbol{\sigma}'_f : \underline{n}_f \otimes \underline{n}_f) \quad (1)$$

46 where $\boldsymbol{\sigma}'_f$ is the current effective stress tensor on the fracture in the presence of fluid perturbations, σ'_{nf} , $|\tau_f|$
 47 and CFF are the effective normal stress, the maximum shear stress and the Coulomb Failure Function
 48 (i.e., Coulomb stress) resolved on the fracture, and \underline{n}_f and μ_s are the unit normal vector and the static
 49 frictional coefficient of the fracture. Hereinafter the subscript f is used to indicate fracture-related
 50 quantities.

51 If fractures themselves are known *a priori*, i.e., \underline{n} and μ_s are given, then the mechanics of fluid-induced
 52 seismicity fundamentally rests on the principle of effective stress (Dunham & Rice, 2008). For any given
 53 fluid-pressurized fracture, the current effective stress state can be decomposed as

$$54 \quad \boldsymbol{\sigma}'_f = \boldsymbol{\sigma}'_{f0} + \delta\boldsymbol{\sigma}'_f \quad (2)$$

55 where $\boldsymbol{\sigma}'_{f0}$ is the arbitrary initial effective stress on the fracture and $\delta\boldsymbol{\sigma}'_f$ is the perturbation due to fluid
 56 overpressure within the fracture.

57 The key step in the hydro-shear process described by equation (1) then lies in the calculation of $\delta\boldsymbol{\sigma}'_f$. This
 58 is traditionally done in a fluid-solid decouple manner. Specifically, the mass conservation law in the form
 59 of fluid pressure diffusion is solved separately to obtain the overpressure within the fault, δp_f . The
 60 alteration to the fluid storage capacity due to solid deformation (i.e., the full volumetric strain for the
 61 fracture itself or a fraction of the volumetric strain for the fracture-hosting rock) is not accounted for.
 62 Following the Terzaghi simple effective stress law (Terzaghi, 1936), it is then assumed that the effective
 63 stress tensor is modified through isotropic reduction of all normal components by the amount of δp_f
 64 whereas all shear components remain unchanged. Following a compression positive notation, it can be
 65 summarized as

$$\delta \boldsymbol{\sigma}'_f = -\delta p_f \mathbf{1} = \begin{bmatrix} -\delta p_f & & \\ & -\delta p_f & \\ & & -\delta p_f \end{bmatrix} \quad (3)$$

67 Substituting equations (2) and (3) into equation (1), one recovers the familiar form of the Coulomb failure
68 function with the pore pressure effect (e.g., [Byerlee, 1978](#))

$$\begin{aligned} CFF &= \left[\left\| \boldsymbol{\sigma}'_{f0} \cdot \underline{n}_f \right\|^2 - \left(\boldsymbol{\sigma}'_{f0} : \underline{n}_f \otimes \underline{n}_f \right)^2 \right]^{1/2} - \mu_s \left(\boldsymbol{\sigma}'_{f0} : \underline{n}_f \otimes \underline{n}_f - \delta p_f \right) \\ &= |\tau_{f0}| - \mu_s \left(\sigma'_{nf0} - \delta p_f \right) \end{aligned} \quad (4)$$

70 where σ'_{nf0} and $|\tau_{f0}|$ are the initial effective normal stress and maximum shear stress on the fracture from
71 $\boldsymbol{\sigma}'_{f0}$.

72 Equation (4) shows that the fluid overpressure within the fracture leads to a direct increase in its Coulomb
73 stress (or effectively, a reduction in its static frictional strength) by the amount of $\mu_s \delta p_f$. To induce
74 seismicity, i.e., the *CFF* is driven from negative to 0, the required δp_f is simply $(\sigma'_{nf0} - |\tau_{f0}| / \mu_s)$. This is
75 widely used as a paradigm in designing experiments on fluid-induced seismicity both in the laboratory
76 and on the field (e.g., [Scuderi & Collettini, 2016](#); [Mukuhira et al, 2017](#)). This decoupled approach also
77 remains as the basis of some prevalent statistical models of induced seismicity (e.g., [Shapiro et al., 2005](#);
78 [Rothert & Shapiro, 2007](#)). In this class of models, a statistically random critical pore pressure is used as a
79 proxy of the frictional strength of a pre-existing fracture and the pore pressure evolution is governed by
80 simple linear fluid diffusion; the modeled spatial-temporal distribution of seismicity, however, is often
81 inconsistent with observations. As a remedy, some nonlinear diffusion models have been developed by
82 adding a pressure-dependent diffusivity ([Hummel & Shapiro, 2012](#); [Johann et al., 2016](#); [Carcione et al.,](#)
83 [2018](#)) in an attempt for better data matching. The diffusion-based seismicity models can be further
84 extended by incorporating, e.g., random stress heterogeneity ([Goertz-Allmann & Wiemer, 2012](#)),
85 fractures following distributions derived from field observations ([Verdon et al., 2015](#)), and even empirical
86 seismic emission criteria for generating synthetic seismograms ([Carcione et al., 2015](#)). This decoupled
87 mechanism also underlies some studies that invert for distributions of permeability ([Tarrahi & Jafarpour,](#)
88 [2012](#)) and pore pressure ([Terakawa et al., 2012](#); [Terakawa, 2014](#)) from induced seismicity data.

89 Equation (4) also underlies some recent physics-based models for forecasting injection-induced
90 seismicity. For example, the RSQSim earthquake simulator, originally developed in the absence of fluid
91 flow and is aimed at improved modeling of seismicity through the inclusion of rate-and-state friction
92 ([Richards-Dinger & Dieterich, 2012](#)), has been extended for forecasting induced seismicity by combining
93 it with an analytical pressure diffusion model ([Dieterich et al., 2015](#); [Kroll et al., 2017](#)). A model based on
94 the so-called “seismogenic index”, which quantifies the seismotectonic state at an injection location

95 (Shapiro et al., 2010) and is locally calibratable using existing injection and seismicity data, has also been
96 proposed and applied to seismicity forecasting at large scales (Langenbruch & Zoback, 2016;
97 Langenbruch et al., 2018). The pressure rate used in the definition of the seismogenic index is derived
98 from the standard pressure diffusion equation decoupled from solid stress state.

99 Despite their successful applications in many cases, the decoupled class of models has two fundamental
100 drawbacks. First, they inherently cannot explain the remoting triggering of seismicity in areas not directly
101 subjected to finite pressure perturbations (Stark & Davis, 1996; Megies & Wassermann, 2014; Yeck et
102 al., 2016). They also incorrectly predict that pore pressure depletion increases the effective normal stress
103 on a fault and therefore will always inhibit seismicity. However, depletion-induced faulting has been
104 amply documented (e.g., Zoback & Zinke, 2002; Van Wees et al., 2014). The Biot theory of
105 poroelasticity (Biot, 1941) provides a viable avenue to eliminating such dilemmas and subsume all
106 observations under one paradigm. At its essence is the full monolithic coupling between the fluid and
107 solid. Specifically, the negative pressure gradient acts an equivalent body force that enters the force
108 balance law and drives changes in the solid deformation and stress; on the other hand, the volumetric
109 strain rate acts an equivalent fluid source in the mass balance law and drives changes in the fluid
110 overpressure (Segall, 2010; Jin & Zoback, 2017). Classic analytical solutions to a fully coupled linear
111 poroelastic system under various simplifying conditions have been derived (e.g., Rice and Cleary, 1976;
112 Cleary, 1977; Segall, 1985; Booker & Carter, 1986; Rudnicki, 1986; Segall & Fitzgerald, 1998; Wang &
113 Kümpel, 2003). Pioneering studies have utilized this theory to explain depletion-induced seismicity
114 (Segall, 1989; Segall et al., 1994) and more recently, probe its roles in injection-induced seismicity
115 (Altmann et al., 2014; Segall & Lu, 2015). Since then the application of the theory of poroelasticity seems
116 to have quickly arisen as a trend in establishing models of induced seismicity, and a rapidly growing body
117 of studies have been documented recently, either analytically based (Jin & Zoback, 2015a; Dempsey &
118 Suckale, 2017) or numerically based (e.g., Chang & Segall, 2016a; Chang & Segall, 2016b; Fan et al.,
119 2016; Deng et al., 2016; Chang & Segall, 2017; Zbinden et al., 2017; Postma & Jansen, 2018; Tung &
120 Masterlark, 2018; Chang & Yoon, 2018; Norbeck & Rubinstein, 2018). At a smaller scale, numerical
121 simulations of fluid-induced microseismicity, typically motivated by applications like stimulations of
122 hydrocarbon and geothermal reservoirs, have also been reported (e.g., Maillot et al., 1999; Angus et al.,
123 2010; Baisch et al., 2010; Zhao & Young, 2011; Wassing et al., 2014; Yoon et al., 2014;
124 Raziiperchikolaee et al., 2014; Riffraction et al., 2016).

125 It is worth noting that a fully coupled poroelastic model has two important distinctions from a decoupled
126 model. First, for the fluid, solid-to-fluid coupling can lead to non-monotonic solutions of the fluid
127 pressure, due to changes in the pore (and fracture) volume caused by the compression or dilation of the
128 solid skeleton. This was first observed in 2D by Mandel (1953) and later in 3D by Cryer (1963) and is
129 collectively referred to as the *Mandel-Cryer effect*. Successfully replicating this phenomenon in the

130 numerical pressure solution is often considered as an important benchmark point (e.g., [White & Borja,](#)
 131 [2011](#)). Second, for the solid, fluid-to-solid coupling generates a full and anisotropic poroelastic stress
 132 tensor instead of an isotropic stress tensor with only normal components as predicted by equation (3).
 133 Additionally, the magnitudes of the normal components differ from $-\delta p_f$. This has been documented in
 134 great details in [Jin & Zoback \(2017, 2018a, 2018b, 2019\)](#). In the context of induced seismicity, the second
 135 distinction is of our interest and it can be summarized as

$$\delta\boldsymbol{\sigma}'_f = \begin{bmatrix} \delta\sigma'_{f,xx} & \delta\sigma'_{f,xy} & \delta\sigma'_{f,xz} \\ & \delta\sigma'_{f,yy} & \delta\sigma'_{f,yz} \\ \text{symmetric} & & \delta\sigma'_{f,zz} \end{bmatrix} \quad (5)$$

137 Here, $\delta\sigma'_{f,xx}$, $\delta\sigma'_{f,yy}$, $\delta\sigma'_{f,zz}$, $\delta\sigma'_{f,xy}$, $\delta\sigma'_{f,xz}$ and $\delta\sigma'_{f,yz}$ are the six independent normal and shear components of
 138 $\delta\boldsymbol{\sigma}'_f$, which are to be solved for from the following quasi-static force balance law on the fault where the
 139 Terzaghi simple effective stress law applies (it is to be paired with the mass balance law in a
 140 monolithically coupled manner, details are not shown here, and the dependence of δp_f on the mean stress
 141 is indicated)

$$\begin{cases} \frac{\partial}{\partial x}(\delta\sigma'_{f,xx}) + \frac{\partial}{\partial y}(\delta\sigma'_{f,yx}) + \frac{\partial}{\partial z}(\delta\sigma'_{f,zx}) + \frac{\partial}{\partial x}(\delta p_f(tr(\delta\boldsymbol{\sigma}'_f))) = 0 \\ \frac{\partial}{\partial x}(\delta\sigma'_{f,xy}) + \frac{\partial}{\partial y}(\delta\sigma'_{f,yy}) + \frac{\partial}{\partial z}(\delta\sigma'_{f,zy}) + \frac{\partial}{\partial y}(\delta p_f(tr(\delta\boldsymbol{\sigma}'_f))) = 0 \\ \frac{\partial}{\partial x}(\delta\sigma'_{f,xz}) + \frac{\partial}{\partial y}(\delta\sigma'_{f,yz}) + \frac{\partial}{\partial z}(\delta\sigma'_{f,zz}) + \frac{\partial}{\partial z}(\delta p_f(tr(\delta\boldsymbol{\sigma}'_f))) = 0 \end{cases} \quad (6)$$

143 Note that here the equilibrium needs to be sought only among the perturbing state itself since the
 144 arbitrary initial state is already in balance. In the coupled approach, the coulomb failure function equation
 145 (1) thus takes a more general form with the poroelastic effect

$$\begin{aligned} CFF &= \left[\left\| (\boldsymbol{\sigma}'_{f0} + \delta\boldsymbol{\sigma}'_f) \cdot \underline{n}_f \right\|^2 - \left[(\boldsymbol{\sigma}'_{f0} + \delta\boldsymbol{\sigma}'_f) : \underline{n}_f \otimes \underline{n}_f \right]^2 \right]^{1/2} - \mu_s \left[(\boldsymbol{\sigma}'_{f0} + \delta\boldsymbol{\sigma}'_f) : \underline{n}_f \otimes \underline{n}_f \right] \\ &= |\tau_{f0} + \delta\tau_f| - \mu_s (\sigma'_{nf0} + \delta\sigma'_{nf}) \end{aligned} \quad (7)$$

147 Comparing equation (7) with equation (4), the difference between the poroelastic effect and the pore
 148 pressure effect on seismicity triggering on a source fracture becomes clear. Generally speaking, $\delta\sigma'_{nf} \neq -$
 149 δp_f . The maximum shear stress on the fracture is also modified. The sense of $\delta\tau_f$ can be the same as or
 150 opposite to τ_{f0} and one must first sum up $\delta\boldsymbol{\sigma}'_f$ and $\boldsymbol{\sigma}'_{f0}$ before calculating the *CFF*. The distinction between
 151 equations (7) and (4) are vital as they can lead to radically different predictions on the time of rupture
 152 nucleation, the co-seismic rupture velocity, rupture style and radiation pattern as well as the post-seismic
 153 distributions of displacement and stress ([Jin and Zoback, 2018a, 2018b](#)).

154 While it has become increasingly recognized that the seismicity-triggering force within the fault-hosting
 155 rock is generated in a poroelastically coupled manner, there appear to be some unfortunate
 156 misconceptions. The first misconception is that pore pressure effect and poroelastic effect are alternative
 157 to each other and the former should be accepted as the correct approach when the Biot-Willis coefficient
 158 α of the hosting rock is less than 0.3 (Johann et al., 2016). The second misconception is that the pore
 159 pressure effect and the poroelastic effect co-exist such that induced seismicity is a result of both (e.g.,
 160 Goebel et al., 2017; Barbour et al., 2017; Keranen & Weingarten, 2018; Skoumal et al., 2018; Yu et al.,
 161 2019). The reason why neither is valid becomes evident at this point. As has been shown above, the key
 162 difference between the pore pressure effect and the poroelastic effect in seismicity triggering lies in
 163 equations (3) and (6), which can now be summarized as

$$164 \quad \delta\boldsymbol{\sigma}_f + \delta p_f \mathbf{1} = \mathbf{0} \quad \text{on } \Omega_f \quad (8)$$

165 for pore pressure effect and

$$166 \quad \nabla \cdot (\delta\boldsymbol{\sigma}_f + \delta p_f \mathbf{1}) = \nabla \cdot \delta\boldsymbol{\sigma}_f + \nabla \delta p_f = \underline{\mathbf{0}} \quad \text{on } \Omega_f \quad (9)$$

167 for poroelastic effect.

168 Here $\mathbf{1}$ is the unit identity (Kronecker delta), $\mathbf{0}$ and $\underline{\mathbf{0}}$ are a second-order tensor and a vector with all 0
 169 constituents and Ω_f is the fracture domain. Equation (9) needs to be closed with appropriate boundary
 170 conditions. Obviously, the solution to equation (8) always satisfies equation (9); however, the solution to
 171 equation (9) does not always guarantee equation (8). In other words, equation (8) is sufficient but not
 172 necessary for equation (9). This is the case, for example, when δp_f is not spatially uniform (i.e., a gradient
 173 in δp_f is present, $\nabla \delta p_f \neq \underline{\mathbf{0}}$). Under this condition, one can readily see that $\nabla \delta p_f$ acts as an equivalent body
 174 force vector and produces a full stress tensor. For the solution from equation (9) to be the same as that
 175 from equation (8), two simplifying conditions are needed. First, the pressure change δp_f is uniform such
 176 that

$$177 \quad \nabla \delta p_f = \underline{\mathbf{0}} \quad (10)$$

178 and second, the domain is subjected to zero incremental traction on the boundary, described by a
 179 Neumann type boundary condition

$$180 \quad (\delta\boldsymbol{\sigma}_f + \delta p_f \mathbf{1}) \cdot \underline{\mathbf{n}}_f = \underline{\mathbf{0}} \quad \text{on } \partial\Omega_f \quad (11)$$

181 where $\partial\Omega_f$ is the fracture domain boundary. Only under the conditions specified by equations (10) and
 182 (11) can the solution to equation (9) also satisfies equation (8). Therefore, I point out that the poroelastic
 183 effect (or more broadly speaking, the poromechanical effect in the presence of material nonlinearity like

184 plasticity and non-Darcy flow) is the true and only effect; the pore pressure effect is the “reduced”
185 poroelastic effect under simplifying conditions and the two should not be considered as alternative nor co-
186 existing effects.

187 For the fault-hosting porous rock itself, the degree of poroelastic coupling is scaled by the Biot coefficient
188 α (typically below 1). [Johann et al. \(2016\)](#) hypothesize that for low-permeability rocks, α should also be
189 negligible and they cast doubt on the validity of the [Segall \(2015, 2016a\)](#) poroelastic models in which
190 $\alpha > 0.3$. This hypothesis is impertinent. α is a measurement of the rock solid’s susceptibility to the
191 influence of the fluid and vice versa. Its exact form was first rigorously derived from basic linear
192 constitutive equations as ([Nur & Byerlee, 1971](#))

$$193 \quad \alpha = 1 - \frac{K_b}{K_m} \quad (12)$$

194 where K_b and K_m are the bulk moduli of the porous rock and the solid skeleton grains, respectively.

195 The exact same expression was later re-derived from the first and second laws of thermodynamics and it
196 was shown that the Biot effective stress tensor arises naturally as power-conjugate to the rate of
197 deformation tensor of the solid phase ([Borja, 2006](#)). Low permeability does not necessarily imply low
198 porosity nor low α . The solid grains can be packed in a manner to maintain high porosity and low K_b
199 (hence high α) with poor or little interconnections between pores (hence low permeability). As a matter of
200 fact, laboratory experiments confirm that α of low-permeability shale reservoir rocks is indeed primarily
201 between 0.3 and 0.9 (e.g., [Hornby, 1995](#); [He et al., 2016](#); [Ma & Zoback, 2017](#)). Returning to the first
202 misconception discussed above, the conclusion by [Johann et al. \(2016\)](#) that the pore pressure effect can
203 approximate the poroelastic effect when $\alpha < 0.3$ is merely a coincidence in the parameter space. In the case
204 of a medium with overall low permeability, or with severe permeability contrasts (e.g., an ultra-low-
205 permeability shale embedded with high-permeability fractures), the differences between distributions of
206 pore pressure and poroelastic stress are drastic ([Jin & Zoback, 2019](#)).

207 The theory of poroelasticity is undoubtedly applicable to fluid-infiltrated and -saturated porous rock
208 across a wide range of permeability scales. Classic analytical solutions offer important insights but are
209 generally less applicable due to restricting conditions. Despite a surging number of numerical poroelastic
210 models as have been mentioned above, applications of them to induced seismicity are rather limited. They
211 are used to either analyze a single event or forecast seismicity rate based on the classic Dieterich
212 Coulomb stress rate model ([Dieterich, 1994](#)), without modeling the spatial-temporal evolutions of
213 seismicity nor their source and statistical characteristics. Notice also that these models either do not
214 explicitly include faults or include very limited number of them and treat them simply as a porous domain
215 with localized permeabilities, therefore the medium is effectively “porous” only. None offered the
216 capacity to model geometrically complex fracture networks. More importantly, some first-order fracture-

217 related physics, for example, the Poiseuille flow behavior within the fracture and the associated
218 nonlinearity due to pressure-induced hydraulic aperture variations, are not accounted for. Furthermore,
219 limited within the capacity of commercial solvers, the fracture domain is often represented with
220 exaggerated thickness (and therefore artificially enhanced along-fracture fluid flow) to facilitate equal-
221 dimensional space discretization. These simplifications come with consequences and may diminish the
222 meaningfulness of modeling outcomes (Jin & Zoback, 2016a, 2016b).

223 To date, a general mechanic-based and physically representative model of fluid-induced seismicity in a
224 geologically realistic medium is not available, due to in part difficulties in establishing a suitable
225 theoretical and computational framework for fluid-saturated, arbitrarily fractured and nonlinear
226 poroelastic solid. As a result, effects of fractures and full coupling on triggering seismicity and controlling
227 its evolutional and source characteristics also remain largely unexplored. We are therefore motivated to
228 develop the following new hydro-mechanical-seismological modeling framework. Built upon our Jin &
229 Zoback (2017) fracture-poro-mechanical computational model, this framework offers the capacity to
230 handle arbitrarily distributed fractures and the associated new physics and nonlinearity. It also integrates
231 for the first time deterministic modeling of inter-seismic, quasi-static and fluid-solid fully coupled
232 triggering and mechanics-based stochastic modeling of co-seismic shear stress drop, and offers a natural
233 way to model multiple induced seismic cycles. An important outcome of the modeling is a synthetic event
234 catalog that allows for further statistical analysis. As a general tool, the model not only is capable of
235 producing many phenomena observed in real data, but also allows for numerically uncovering some
236 otherwise unknown effects of model configuration and physics on induced seismicity. Details are
237 described below. Throughout the text, space- and time-dependent quantities in all equations are marked
238 using (\underline{x}, t) .

239 **2. Theory and Implementation**

240 **2.1 Calculating Effective Stress on Fractures**

241 As has been shown in section 1, the pivotal piece in modeling fluid induced seismicity lies in the
242 calculation of the current effective stress tensor σ'_f , defined on the fracture domain Ω_f . While it suffices to
243 use Ω_f for describing the essence of poroelastic seismicity triggering (equations (2), (7) and (9)) and its
244 fundamental difference from pore pressure triggering (equations (1), (2) and (8)), the calculation of σ'_f is
245 a different issue. Directly solving equation (9) (coupled with a mass balance law) obviously requires
246 discretizing an irregular stand-alone domain consists fractures with arbitrary locations and orientations as
247 well as lengths and thicknesses that typically differ by orders of magnitude. Additionally, the fracture
248 domain is coupled with the hosting rock through fluid and solid boundary conditions that are challenging
249 to implement. One can circumvent this dilemma by indirectly solving for σ'_f . To do so, the traction
250 continuity condition across any given rock-fracture interface can be invoked,

$$251 \quad \left[\underbrace{\boldsymbol{\sigma}(\underline{x}, t) \cdot \underline{n}_f}_{\text{hosting rock}} - \underbrace{\left(\boldsymbol{\sigma}'_f(\underline{x}, t) + p_f(\underline{x}, t) \mathbf{1} \right) \cdot \underline{n}_f}_{\boldsymbol{\sigma}_f} \right] = \underline{\mathbf{0}} \quad \forall \underline{n}_f, \underline{x} \in \partial f \quad (13)$$

252 where $\boldsymbol{\sigma}$ and $\boldsymbol{\sigma}_f$ are the current Cauchy total stress tensor within the hosting rock (i.e., matrix) and on the
 253 fracture of interest, respectively, \underline{n}_f and $\underline{\mathbf{0}}$ are the same as before, and ∂f is the matrix-fracture interface.

254 Because equation (13) holds for any fracture of arbitrary orientation \underline{n}_f , it implies the following equality

$$255 \quad \boldsymbol{\sigma}(\underline{x}, t) - \boldsymbol{\sigma}_f(\underline{x}, t) = \mathbf{0}, \quad \underline{x} \in \partial f \quad (14)$$

256 Therefore, following the simple effective stress law, the effective stress tensor on the fracture of interest
 257 can be expressed as

$$258 \quad \boldsymbol{\sigma}'_f(\underline{x}, t) = \boldsymbol{\sigma}_f(\underline{x}, t) - p_f(\underline{x}, t) \mathbf{1} = \boldsymbol{\sigma}(\underline{x}, t) - p_f \mathbf{1}(\underline{x}, t), \quad \underline{x} \in \partial f \quad (15)$$

259 To show the initial and perturbing states, equation (15) can be further expanded as

$$260 \quad \boldsymbol{\sigma}'_f(\underline{x}, t) = (\boldsymbol{\sigma}_0 + \delta \boldsymbol{\sigma}(\underline{x}, t)) - (p_{f0} + \delta p_f(\underline{x}, t)) \mathbf{1}, \quad \underline{x} \in \partial f \quad (16)$$

261 where the subscript “0” indicates initial states whereas “ δ ” suggests perturbing states. Here, δp_f is the
 262 same as in equation (3) and is also referred to as the fluid overpressure within fractures or fault-zone
 263 overpressure.

264 **2.2 Two Sources of Changes in Total Stress and Overpressure**

265 From equation (16), it can be readily seen that the focus of the problem is now diverted towards solving
 266 for the two perturbing quantities: the Cauchy total stress tensor $\delta \boldsymbol{\sigma}$ in the poroelastic hosting rock and the
 267 fluid overpressure δp_f within fractures. Because the medium undergoes both fluid perturbations externally
 268 and seismicity internally, both variables can be decomposed to reflect these two sources as

$$269 \quad \delta \boldsymbol{\sigma}(\underline{x}, t) = \delta \boldsymbol{\sigma}_p(\underline{x}, t) + \sum_j \delta \boldsymbol{\sigma}_s^{(j)}(\underline{x}, t) H(CFF^{(j)}) \quad (17)$$

$$270 \quad \delta p_f(\underline{x}, t) = \delta p_{fp}(\underline{x}, t) + \underbrace{\sum_j \delta p_{fs}^{(j)}(\underline{x}, t)}_{\approx 0} H(CFF^{(j)}) \quad (18)$$

271 Here,

$$272 \quad H(CFF) := \begin{cases} 0, & CFF < 0 \\ 1, & CFF \geq 0 \end{cases} \quad (19)$$

273 In equations (17), H is the Heaviside function, CFF is calculated according to equation (7), the subscript
274 “ p ” indicates poroelastic changes arising from external fluid perturbations, the subscript “ s ” indicates
275 seismicity-induced (i.e., fracture slip-induced) redistributions, and (j) refers to the number of episodes of
276 slip on an event-generating source fracture. Here it is worth noting that external fluid perturbations fall
277 into three categories: injection/withdraw pressure, surface flux (mass rate per unit area) and volume flux
278 (mass rate per unit volume), the former two described by fluid Dirichlet and Neumann boundary
279 conditions, respectively, and the last specified by a direct source/sink term. There appears to be some
280 growing interest on which relates to induced seismicity the most (e.g., [Barbour et al., 2017](#); [Almakari et
281 al., 2019](#); [Alba et al., 2020](#); [Hopp et al., 2020](#)). Essentially, such differentiations are about testing the
282 sensitivity of the governing law to the prescribed boundary conditions which all become parts of an
283 external fluid mass vector for a linear problem and a residual vector for a nonlinear problem. Providing a
284 universal answer should not be attempted, rather, the analysis ought to be done on a case-by-case basis.

285 Recall that mode-II slip on a source fracture yields negligible changes in the overpressure within it
286 (volumetric strain occur in the hosting rock but not on the fracture), therefore, in this study, δp_{fs} is
287 approximately 0 as is indicated in equation (18) such that $\delta p_f \approx \delta p_{fp}$ and can be solely attributed to external
288 fluid perturbations.

289 Equations (17) and (18) must be substituted into equation (16) for determining if seismicity occurs on the
290 fracture of interest according to equation (7); if yes, the seismic cycle needs to be updated ($j=j+1$) for this
291 fracture. This process ought to be iterated over all time steps for all fractures. The major computational
292 cost then arises from the calculation of external perturbations-induced changes $\delta \sigma_p$ and δp_{fp} as well as
293 seismicity-induced changes $\delta \sigma_s$. The first two variables can be obtained from our [Jin & Zoback \(2017\)](#)
294 computational model. The last variable can also be solved for in a fully dynamic spontaneous earthquake
295 rupture problem with a loading history from the former two and this can be achieved using our [Jin &
296 Zoback \(2018a, 2018b\)](#) computational model. For an arbitrarily fractured domain with a large fracture
297 population, this task is perhaps computationally intractable. In this study, I seek intermediate solutions by
298 focusing on the inter-seismic evolution of induced seismicity but not the co-seismic dynamic changes,
299 therefore, rather than solving for all three for updating fracture stress, I will instead solve only for $\delta \sigma_p$ and
300 δp_{fp} and insert them into a novel fracture stress updating algorithm to indirectly account for the effect of
301 $\delta \sigma_s$ on source fractures without considering source-to-source interactions. The details of these two steps
302 are given in the following three sections.

303 2.3 Fracture-Poro-Mechanical Modeling

304 2.3.1 Objective and Challenges

305 The objective of this section is to calculate $\delta\sigma_p$ within the hosting rock and δp_{fp} within fractures as inputs
306 for updating the Coulomb stress on fractures. Here, the total stress tensor $\delta\sigma_p$ is further decomposed as the
307 following according to the Biot effective stress law,

$$308 \quad \delta\sigma_p(\underline{x}, t) = \delta\sigma'_p(\underline{x}, t) + \alpha\delta p_p(\underline{x}, t)\mathbf{1} \quad (20)$$

309 where $\delta\sigma'_p$ and δp_p are changes in the effective stress tensor and the fluid overpressure within the hosting
310 rock due to external fluid perturbations, and α is the Biot-Willis coefficient.

311 Three major issues are posed here. First, from equations (16) and (20), it can now be seen that this step
312 indeed involves three unknown variables, $\delta\sigma'_p$, δp_p and δp_{fp} , and therefore requires solving three
313 governing equations, including one force balance law for the hosting rock and two mass conservation
314 laws for the hosting rock and fractures, respectively. This step is referred to as *fracture-poro-mechanical*
315 *modeling*. Second, $\delta\sigma'_p$ must be solved for simultaneously with the associated fluid overpressure δp_p in a
316 fully coupled manner. Third, all three variables are functions of the arbitrary network of pre-existing
317 fractures, which not only introduces additional fluid behaviors but also spans over a wide range of scales.
318 While accounting for all fractures is probably computationally intractable, the subset of fractures at a
319 scale comparable to the model domain must be deterministically resolved, as they have amply been
320 demonstrated to have a first-order control of modeling outcomes (e.g., Berkowitz, 2002; Vujevic' et al.,
321 2014; Hirthe & Graf, 2015; Hardebol et al., 2015). I hereinafter refer to these fractures as the *large-scale*
322 *deterministic fractures (LSDF)*, which can be expressed as

$$323 \quad LSDF = \bigcup_i^N F_i \quad (21)$$

324 where F_i is the i^{th} large-scale fracture and N is the total population.

325 2.3.2 Progressive Scenarios

326 To address the above issues and illustrate effects of the *LSDF* and full poroelastic coupling on seismicity,
327 three progressive scenarios are constructed, each physically more representative than the previous. In the
328 base scenario (case 1), I consider a fluid diffusion problem in a porous rock matrix Ω_m , which is governed
329 by the following mass conservation law accompanied by the Darcy's flow equation. They read

$$330 \quad \left(\phi_{m0}(\underline{x})(C_m + C_r)\right) \frac{\partial}{\partial t} \delta p_p(\underline{x}, t) + \nabla \cdot \underline{v}(\underline{x}, t) = s(\underline{x}, t) \quad \underline{x} \in \Omega_m \quad (22)$$

$$331 \quad \underline{v}(\underline{x}, t) = -\eta^{-1} \mathbf{k}_m(\underline{x}) \cdot \nabla \delta p_p(\underline{x}, t) \quad \underline{x} \in \Omega_m \quad (23)$$

332 where ϕ_{m0} is the initial matrix porosity, C_m , C_ρ are compressibilities of the matrix and the fluid,
 333 respectively, \underline{v} is the fluid velocity, s is the fluid source/sink term divided by the initial fluid density, η is
 334 the fluid viscosity, and \mathbf{k}_m is the full matrix permeability tensor permitted to be heterogeneous and fully
 335 anisotropic.

336 In the next scenario (case 2), I consider fluid diffusion in a fractured porous media by introducing the
 337 *LSDF* into the porous rock. In an equal-dimensional representation, the fractured domain is denoted as
 338 $\Omega = \Omega_m \cup \Omega_f$. For efficient computations without resolving transversal details across each fracture, [Jin &](#)
 339 [Zoback \(2017\)](#) proposed a new formulation customized for hydraulically conductive fractures. Due to its
 340 exceedingly thin nature, the fracture domain Ω_f can be reduced into a lower-dimensional domain
 341 superposed onto (instead of portioned from) the ambient matrix domain Ω_m such that $\Omega_f \subset \Omega_m = \bar{\Omega}$ where $\bar{\Omega}$
 342 is a mixed-dimensional approximation of Ω . In this manner, fractures introduce no additional degrees of
 343 freedom (i.e., the unknown overpressure is now δp_p only rather than both δp_p and δp_{fp}), and the following
 344 relation holds

$$345 \quad \delta p_{fp} \subset \delta p_p \quad (24)$$

346 However, the fluid storage capacity of the medium is now augmented due to the presence of fractures and
 347 the mass balance over the fractured domain now reads ([Jin & Zoback, 2017](#))

$$348 \quad \left(\Lambda_0(\underline{x}) \phi_{m0}(\underline{x}) (C_m + C_\rho) + (1 - \Lambda_0(\underline{x})) (C_f + C_\rho) \right) \frac{\partial}{\partial t} \delta p_p(\underline{x}, t) + \nabla \cdot \underline{v}(\underline{x}, t) = s(\underline{x}, t) \quad \underline{x} \in \bar{\Omega} \quad (25)$$

349 where Λ_0 is a locally defined geometric factor that depends on the initial hydraulic aperture of fractures
 350 and C_f is the fracture compressibility.

351 Also, the hydraulic conductivity of the medium is enhanced and the addition of a nonlinear Poiseuille
 352 flow equation is needed for describing the localized fluid behavior within fractures. It reads

$$353 \quad \underline{v}(\underline{x}, t) = -\eta^{-1} \frac{1}{12} \left(b_0 (1 + C_f \delta p_{fp}(\underline{x}, t)) \right)^2 \nabla_\tau \delta p_{fp}(\underline{x}, t) \quad \underline{x} \in \Omega_f \quad (26)$$

354 where b_0 is the initial hydraulic aperture of fractures and ∇_τ is the tangential gradient operator.

355 Poroelasticity is not considered in scenarios 1 and 2. In the last scenario (case 3), I further introduce full
 356 poroelastic coupling to the mixed-dimensional fractured domain $\bar{\Omega}$. The mass conservation law shown by
 357 equation (25) now needs a further modification to reflect a second change to the fluid storage capacity
 358 due to the solid matrix volumetric strain. Following a compression positive notation, it reads ([Jin &](#)
 359 [Zoback, 2017](#))

$$\begin{aligned}
& \left(\Lambda_0(\underline{x})\phi_{m0}(\underline{x})(C_m + C_\rho) + (1 - \Lambda_0(\underline{x}))\phi_{f0}(\underline{x})(C_f + C_\rho) \right) \frac{\partial}{\partial t} \delta p_p(\underline{x}, t) \\
& - \alpha \nabla \cdot \left(\frac{\partial}{\partial t} \delta \underline{u}_p(\underline{x}, t) \right) + \nabla \cdot \underline{v}(\underline{x}, t) = s(\underline{x}, t) \quad \underline{x} \in \bar{\Omega}
\end{aligned} \tag{27}$$

Equation (27) is to be fully and monolithically coupled with the following quasi-static force balance law

$$\nabla \cdot \left(\delta \boldsymbol{\sigma}'_p(\underline{x}, t) + \alpha \delta p_p(\underline{x}, t) \mathbf{1} \right) = \nabla \cdot \delta \boldsymbol{\sigma}'_p(\underline{x}, t) + \alpha \nabla \delta p_p(\underline{x}, t) = \underline{0} \quad \underline{x} \in \bar{\Omega} \tag{28}$$

In this study, I consider the fractured medium in its entirety as linear elastic and adopt the Hooke's law

$$\delta \boldsymbol{\sigma}'_p(\underline{x}, t) = \mathbf{D} : \nabla^{(s)} \delta \underline{u}_p(\underline{x}, t) \quad \underline{x} \in \bar{\Omega} \tag{29}$$

Here in equations (27) and (29), $\delta \underline{u}_p$ is the change to the solid matrix displacement vector due to external fluid perturbations, \mathbf{D} is the elastic stiffness tensor, $\nabla^{(s)}$ is the symmetric gradient operator and “:” indicates double tensor contraction.

Table 1 summarizes the three progress scenarios, the latter two being nonlinear. The nonlinearity is sourced from equation (26) and is two-fold, as is manifested by first the pressure-dependent hydraulic aperture and second, the fracture permeability as a quadratic function of the hydraulic aperture, therefore the medium becomes nonlinearly poroelastic. Such form of nonlinearity is typically not included in previous seismicity modeling studies.

Table 1. Three progressive scenarios

Scenarios	Governing equations				Descriptions
	Fluid		Solid		
	Conservation	Flow	Balance	Constitutive	
Case 1	(22)	(23)	N/A	N/A	Fluid diffusion in a porous medium; linear
Case 2	(25)	(23), (26)	N/A	N/A	Fluid diffusion in a fractured porous medium; nonlinear
Case 3	(27)	(23), (26)	(28)	(29)	Fully monolithically coupled fluid diffusion and solid stressing in a fractured poroelastic medium; nonlinear

In seeking for a numerical solution, [Jin & Zoback \(2017\)](#) developed a hybrid-dimensional two-field mixed finite element method for efficient space discretization while preserving the distribution of a given set of deterministic fractures; the solution of the fully coupled semi-discrete system is advanced in time in a fully coupled manner (as opposed to a sequentially coupled manner) following a fully implicit (backward Euler) finite difference scheme; within each time step, the resulting nonlinear and fully discrete equation is solved using a Newton-Raphson solver. This technique is adopted for case 3. For case 1, the discretization is done in space using a standard Galerkin finite element method and in time using a backward Euler scheme; no linearization is needed. For case 2, the discretization and linearization procedures resemble those in case 3 except for the use of a single-field interpolation scheme. To illustrate the differences, for cases 1-3, I give their respective semi-discrete forms of the governing laws shown in table 1 after space discretization. They read

$$385 \quad \tilde{\mathbf{M}} \dot{\hat{\zeta}}_p + \mathbf{K} \hat{\zeta}_p - \underline{E}_1 = \underline{0} \quad (30)$$

$$386 \quad \left(\mathbf{M} + \sum_I^N \mathbf{M}_{F_i}(\hat{\zeta}_{pF_i}) \right) \dot{\hat{\zeta}}_p + \left(\mathbf{K} + \sum_I^N \mathbf{K}_{F_i}(\hat{\zeta}_{pF_i}) \right) \hat{\zeta}_p - \underline{E}_2 = \underline{R}_2 \quad (31)$$

$$387 \quad \begin{bmatrix} \mathbf{M} + \sum_I^N \mathbf{M}_{F_i}(\hat{\zeta}_{pF_i}) & -\mathbf{C}^T \\ \mathbf{0} & \mathbf{0} \end{bmatrix} \begin{Bmatrix} \dot{\hat{\zeta}}_p \\ \underline{d}_p \end{Bmatrix} + \begin{bmatrix} \mathbf{K} + \sum_I^N \mathbf{K}_{F_i}(\hat{\zeta}_{pF_i}) & \mathbf{0} \\ \mathbf{C} & \mathbf{G} \end{bmatrix} \begin{Bmatrix} \hat{\zeta}_p \\ \underline{d}_p \end{Bmatrix} - \begin{Bmatrix} \underline{E}_3 \\ \underline{Y} \end{Bmatrix} = \underline{R}_3 \quad (32)$$

388 where $\tilde{\mathbf{M}}$ and \mathbf{M} are fluid storage capacity matrices in the absence and presence of fractures, respectively,
 389 \mathbf{K} is the hydraulic conductivity/transferability matrix, \mathbf{G} is the stiffness matrix, \mathbf{C} is the coupling matrix,
 390 \underline{E}_1 , \underline{E}_2 and \underline{E}_3 , which take different forms, are external nodal mass vectors for cases 1-3, \underline{Y} is the external
 391 nodal force vector, $\hat{\zeta}_p$ and \underline{d}_p are nodal values of δp and $\delta \underline{u}_p$, respectively, augmenting quantities
 392 associated the *LSDF* are indicated with the subscript “ F_i ” and I and N are the same as in equation (21).
 393 The detailed expressions of the above discrete matrices and vectors can be found in [Jin & Zoback \(2017\)](#).
 394 $\tilde{\mathbf{M}}$, \underline{E}_1 , \underline{E}_2 can be obtained by removing the fracture effect and/or the coupling effect from their respective
 395 counterparts.

396 Solving the fully discrete form of equations (30) - (32) gives their respective final numerical solutions.
 397 For the two cases with fractures (cases 2 and 3), the numerical solution of fracture overpressure δp_{fp} ,
 398 denoted as $\hat{\zeta}_{fp}$, is then obtained by extracting a subset of the hosting rock pressure nodal values,

$$399 \quad \hat{\zeta}_{fp} = \mathbf{Q} \hat{\zeta}_p \quad (33)$$

400 where \mathbf{Q} is a matrix with 0 and 1 constituents. Details can be found on [Jin and Zoback \(2017\)](#).

401 Additionally, for case 3, the numerical solution of $\delta \sigma'_p$ is in the so-called Voigt notation and it is
 402 calculated from \underline{d}_p as

$$403 \quad \delta \sigma'_p = \mathbf{DB} \underline{d}_p \quad (34)$$

404 where \mathbf{B} is standard finite element displacement-strain transformation matrix (e.g., [Hughes, 2012](#)).

405 2.3.3 Poroelastic Stress Invariants

406 In the fully coupled scenario (case 3), to examine and understand roles of poroelastic stressing in
 407 seismicity evolution, the distribution of *CFE* within the hosting rock is often plotted. In the presence of
 408 several faults with the same orientations, this step is straightforward (e.g., [Chang & Segall, 2016a](#)). In the
 409 case with varying fracture orientations, however, it is pragmatic to define an equivalent *CFE* calculated

410 from stress invariants. Here, two poroelastic stress invariants are calculated according to standard
411 formulations except for the use of the effective poroelastic stress tensor $\delta\sigma'_p$. Under plane strain, they read:

$$412 \quad \frac{1}{3}I_1' = \frac{1}{3}(1+\nu)(\delta\sigma'_{px} + \delta\sigma'_{py}) \quad (35)$$

$$413 \quad \sqrt{J_2'} = \sqrt{\frac{1}{6} \left[(\delta\sigma'_{px} - \delta\sigma'_{py})^2 + (\delta\sigma'_{py} - \nu(\delta\sigma'_{px} + \delta\sigma'_{py}))^2 + (\delta\sigma'_{px} - \nu(\delta\sigma'_{px} + \delta\sigma'_{py}))^2 \right] + (\delta\sigma'_{pxy})^2} \quad (36)$$

414 where ν is the Poisson's ratio, $\delta\sigma'_{px}$, $\delta\sigma'_{py}$ are the two normal components and $\delta\sigma'_{pxy}$ is the shear
415 component of $\delta\sigma'_p$, I_1' and $\sqrt{J_2'}$ are the first and second poroelastic stress invariants.

416 Using these two invariants, an *excess poroelastic shear stress* denoted as MC , is defined,

$$417 \quad MC = \sqrt{J_2'} - \sin(\phi) \frac{1}{3}I_1' \quad (37)$$

418 Here,

$$419 \quad \phi = \tan^{-1}(\mu_s) \quad (38)$$

420 Equation (37) is adapted from the invariant form of the Mohr Coulomb yield function (e.g., [Borja, 2013](#))
421 by setting the cohesion to 0 and the Lode's angle as $\pi/6$. In a sense, MC is the invariant form of CFE .

422 2.4 Inputs Preparation

423 At this point, for the two scenarios with fractures (cases 2 and 3), equation (16) can now be elaborated as
424 the following

$$425 \quad \sigma'_f(\underline{x}, t) = \left(\sigma_0 + \delta\sigma_p(\underline{x}, t) + \sum_j \delta\sigma_s^j(\underline{x}, t)H(CFF^j) \right) - \left(p_{f0} + \overbrace{\delta p_{fp}(\underline{x}, t) + \sum_j \underbrace{\delta p_{fs}^j(\underline{x}, t)}_{\approx 0}H(CFF^j)}^{\delta p_f(\underline{x}, t), \approx \delta p_{fp}(\underline{x}, t)} \right) \mathbf{1}_{\underline{x} \in \partial f} \quad (39)$$

426 Applying the simple effective stress law for fractures, equation (39) collapses into a more general form

$$427 \quad \sigma'_f(\underline{x}, t) = \sigma'_{f0} + \delta\sigma'_{fp}(\underline{x}, t) + \sum_j \delta\sigma'^j_{fs}(\underline{x}, t)H(CFF^j) \quad (40)$$

428 where $\delta\sigma'_{fp} = \delta\sigma_p - \delta p_{fp}\mathbf{1}$ and $\delta\sigma'_{fs} = \delta\sigma_s - \delta p_{fs}\mathbf{1}$ are the effective stress changes on fractures from external fluid
429 perturbations and seismicity, respectively, and their summation is $\delta\sigma'_f$ shown in equation (2). Also, $\delta\sigma'_{fs} \approx$
430 $\delta\sigma_{fs}$.

431 Here, the numerical solution of $\delta\sigma'_{fp}$ vary among scenarios and its expression is obtained from equations
 432 (3) and (33) for case 2 and equations (20), (34) for case 3. For case 1, since fractures are absent, the
 433 definition of fracture effective stress does not apply. Nevertheless, to facilitate seismicity modeling, pre-
 434 defined random critical pore pressure as described in [Shapiro et al. \(2005\)](#) can be seeded in the domain,
 435 and an equivalent $\delta\sigma'_{fp}$ (which indeed should be written as $\delta\sigma'_p$), can be defined similar to equation (3). In
 436 mixed finite element discretization, numerical solutions reside at nodes for the fluid pressure but
 437 integration points for the stress. The mixed-field elements in [Jin & Zoback \(2017\)](#) are equal-lower-order,
 438 leading to element-wise constant strain and stress. Accordingly, to compute the element-wise effective
 439 stress, the element-averaged nodal fluid pressure is used. Mapped back into the tensor notation, the above
 440 is summarized as

$$441 \quad \delta\sigma'_{fp} = \begin{cases} -\alpha \left(\hat{\zeta}_p \right)_{mean} \mathbf{1}, & \text{case 1} \\ -\left(\mathbf{Q} \hat{\zeta}_p \right)_{mean} \mathbf{1}, & \text{case 2} \\ \left(\mathbf{DB} \underline{d}_p \right)_{Voigt \rightarrow tensor} + \alpha \left(\hat{\zeta}_p \right)_{mean} \mathbf{1} - \left(\mathbf{Q} \hat{\zeta}_p \right)_{mean} \mathbf{1}, & \text{case 3} \end{cases} \quad (41)$$

442 2.5 Seismological Modeling

443 The modeling outcomes from section 2.3 provide essential inputs for seismicity modeling. The remaining
 444 task here is to iteratively determine if seismicity occurs from equation (7), and if yes, update the stress on
 445 fractures and generate a synthetic event catalog.

446 2.5.1 A Dual-Scale Discrete Fracture Network

447 A dual network of fractures, hereinafter referred to as the *DF*, is considered as the source for seismicity. It
 448 consists of two complementary subsets A and B, where the subset A, denoted as \widetilde{LSDF} , is an
 449 approximation to the *LSDF* using a series of discrete fractures and the subset B is a stochastic
 450 representation of small-scale fractures typically found in the surrounding hosting rock and is hereinafter
 451 referred to as the *SSSF*. The above description can be summarized as:

$$452 \quad DF = LSDF \cup SSSF = \left(\bigcup_a^{n_a} f_a \right) \cup \left(\bigcup_b^{n_b} f_b \right) \quad (42)$$

453 where f_a is the a^{th} fracture in the subset A, f_b is the b^{th} fracture in the subset B, and n_a and n_b are the
 454 respective populations.

455 2.5.2 Stochastic Stress Drop Modeling Constrained by Poroelastic Stressing History

456 As has been discussed in section 2.2, fracture stress will be updated first using external perturbation-
 457 induced changes and then corrected to account for slip-induced redistributions. To this end, two
 458 simplifications are made. First, source-to-source interactions are neglected, i.e., stress on a fracture is not

459 affected by slip on nearby fractures. Second, slip causes negligible changes in the effective normal stress
460 on the source fracture itself. This reads

$$461 \quad \delta\sigma'_{fs}(\underline{x}, t) : \underline{n}_f \otimes \underline{n}_f \approx 0 \quad (43)$$

462 Combined with equation (40), equation (43) implies that

$$463 \quad \sigma'_f(\underline{x}, t) : \underline{n}_f \otimes \underline{n}_f \approx (\sigma'_{f0}(\underline{x}) + \delta\sigma'_{fp}(\underline{x}, t)) : \underline{n}_f \otimes \underline{n}_f \quad (44)$$

464 Therefore the shear stress on the fracture after slip can now be re-written in the following form

$$465 \quad \sqrt{\|\sigma'_f(\underline{x}, t) \cdot \underline{n}_f\|^2 - (\sigma'_f(\underline{x}, t) : \underline{n}_f \otimes \underline{n}_f)^2} = \sqrt{\|(\sigma'_{f0} + \delta\sigma'_{fp}(\underline{x}, t)) \cdot \underline{n}_f\|^2 - ((\sigma'_{f0} + \delta\sigma'_{fp}(\underline{x}, t)) : \underline{n}_f \otimes \underline{n}_f)^2} - \sum_j \Delta\tau_j \quad (45)$$

466 Here, $\Delta\tau_j$ is the static shear stress drop on the fracture due to the j^{th} episode of slip. The constrained
467 stochastic stress drop modeling on a source fracture based on its full poroelastic loading history is
468 describe by

$$469 \quad \Delta\tau_j = r\Delta\tau_{j\max} \quad (46)$$

470 Here,

$$471 \quad \Delta\tau_{j\max} = (\mu_s - \mu_d)(\sigma'_{f0} + \delta\sigma'_{fp}(\underline{x}, t_j^*)) : \underline{n}_f \otimes \underline{n}_f \quad (47)$$

472 In equations (46) and (47), t_j^* is the time at which the j^{th} episode of slip occurs, μ_d is the fracture dynamic
473 frictional coefficient as is typically used in a slip-weakening law (Andrews, 1976), $\Delta\tau_{j\max}$ is the maximum
474 likely shear stress drop and r is a stochastic parameter between 0 and 1 in honor of potential non-full
475 degree of stress drop (see also Verdon et al., 2015). The distribution of $\Delta\tau_j$ is a convolution of
476 distributions of r and $\Delta\tau_{j\max}$. In this study, since $\Delta\tau_{j\max}$ is deterministically modeled, only the distribution
477 of r is needed, which is assumed to be uniform on [0, 1]. Equations (46) and (47) state that first, the new
478 shear stress on a fracture due to seismicity is constrained above a lower bound defined by the residual
479 frictional strength of the fracture and second, the maximum likely shear stress drop on a source fracture is
480 determined by its full inter-seismic poroelastic loading history. This is an improvement on directly
481 prescribing the shear stress drop in previous studies (e.g., Izadi & Elsworth, 2014).

482 2.5.3 Source Parameter Calculations

483 The key equations used in calculating the seismic source parameters are shown here. First, the seismic
484 moment M_0 can be calculated from the fracture dimension and the recorded $\Delta\tau$. Depending on the fracture
485 geometry and the faulting regime, various formulas are available. Here, I opt for the one suitable for a
486 rectangular dip-slip fracture (Kanamori and Anderson, 1975):

$$M_0 = \frac{\pi(\lambda + 2\mu)}{4(\lambda + \mu)} \Delta\tau W^2 L \quad (48)$$

where W is the fracture width (assumed as 1 m in numerical examples under plane strain), λ and μ are the Lamé's constant and the shear modulus of the medium.

Second, the moment magnitude M_w is calculated from M_0 following (Hanks & Boore, 1984):

$$M_w = \frac{2}{3}(\lg M_0 - 9.1) \quad (49)$$

2.5.4 Fracture Stress Updating Algorithm

Inspired by the prediction-correction type of algorithm in plasticity computational modeling, here I propose the following incremental fracture stress updating and seismicity generation algorithm. The overshoot in the inter-seismic prediction step can be minimized by reducing the time step used for matching the solutions of equations (30) - (32).

List 1. Incremental fracture stress updating algorithm

```

for fracture  $f_i$  % within the  $DF$ , equation (42)
  for time step  $t_k$ 
    get  $\sigma'_{fp}(f_i, t_k)$ ,  $\sigma'_{fp}(f_i, t_{k-1})$  % calculated and stored in sections 2.3 and 2.4
    get  $\sigma'_{fn}(f_i, t_{k-1})$ ,  $\tau_f(f_i, t_{k-1})$ ,  $CFF(f_i, t_{k-1})$  from  $t_{k-1}$ 
    predict  $\tilde{\sigma}'_{fn}(f_i, t_k)$ ,  $\tilde{\tau}_f(f_i, t_k)$ ,  $\tilde{CFF}(f_i, t_k)$  from  $\sigma'_f(f_i, t_k) = \sigma'_{f0}(f_i) + \delta\sigma'_{fp}(f_i, t_k)$  % equation (7)
    % incremental poroelastic stress compensation on the fracture (inter-seismic)
     $\sigma'_{fn}(f_i, t_k) = \sigma'_{fn}(f_i, t_{k-1}) + (\tilde{\sigma}'_{fn}(f_i, t_k) - \sigma'_{fn}(f_i, t_{k-1}))$ 
     $\tau_f(f_i, t_k) = \tau_f(f_i, t_{k-1}) + (\tilde{\tau}_f(f_i, t_k) - \tau_f(f_i, t_{k-1}))$ 
     $CFF(f_i, t_k) = CFF(f_i, t_{k-1}) + (\tilde{CFF}(f_i, t_k) - CFF(f_i, t_{k-1}))$ 
    % correction for seismicity-induced shear stress drop on the fracture, if any (co-seismic)
    if  $CFF(f_i, t_k) \geq 0$ 
       $\Delta\tau(f_i, t_k) = r(\mu_s - \mu_d)\sigma'_{fn}(f_i, t_k)$  % equations (46), (47)
       $\tau_f(f_i, t_k) = \mu_s\sigma'_{fn}(f_i, t_k) - \Delta\tau(f_i, t_k)$  % update the fracture shear stress
       $CFF(f_i, t_k) = \tau_f(f_i, t_k) - \mu_s\sigma'_{fn}(f_i, t_k) = -\Delta\tau(f_i, t_k)$  % update the fracture  $CFF$ 
      nos=nos+1 % number of seismic cycles
      record and calculate seismic source parameters % section 2.5.3
    end
  end
end

```

In list 1, the fracture f_i needs to be associated with a stress tensor $\delta\sigma'_{fp}(f_i, t)$. Since f_i can intersect multiple elements (or Gauss integration points if using high-order finite elements), here, I will use only the stress tensor from the element nearest to its center. The above algorithm automatically produces multiple seismic cycles and therefore offers a natural way of modeling repeating events. I am now at a place to

502 proceed to the seismological modeling, see figure 1 for a schematic illustration. A complete seismicity
503 catalog containing information on, e.g., the event origin time t_0 , the location \underline{x} , the shear stress drop $\Delta\tau$,
504 the seismic moment M_0 , the moment magnitude M_w , the fracture length L and the initial Coulomb stress
505 CFF_0 , can be assembled. Notice in equation (48), a unit length along the third dimension is used.
506 Additionally, the definitions of a triggered event and an induced event are given and they will be
507 elaborated later in section 4.3.3 and used there for classifying the modeled events.

508 **3. Microseismic-Scale Numerical Example Model Set-Up**

509 **3.1 Step 1 for Fracture-Poro-Mechanical Modeling**

510 As a microseismic-scale numerical example, a $200\text{ m} \times 200\text{ m}$ 2D domain is constructed representing a
511 fracture-hosting porous rock. For cases 2 and 3, a *LSDF* with 100 constituents with lengths ranging from
512 20 m to 50 m, and orientations, from 0 to 360° , is resolved, see figure 2a. The model domain is then
513 discretized in space, see figure 2b, to arrive at the semi-discrete forms given by equations (31) and (32).
514 For case 1, no fracture is present; nevertheless, for meaningful comparisons, the same mesh is used for
515 arriving at equation (30). For cases 2 and 3, the nominal model parameters, including the hydraulic and
516 mechanical properties, the coupling coefficient of the hosting rock (i.e., the Biot-Willis coefficient α), the
517 fluid and solid boundary conditions and the time-stepping parameter are identical to those in [Jin &](#)
518 [Zoback \(2017\)](#). A particular quantity of interest is the hydraulic diffusivity of the hosting rock and the
519 *LSDF* in cases 2 and 3, which are $9.95 \times 10^{-4}\text{ m}^2/\text{s}$ and $6.64\text{ m}^2/\text{s}$, respectively. For case 1, the parameters
520 are also the same except for the permeability of the hosting rock, which is 23 mD, leading to a hydraulic
521 diffusivity $D_h = 0.03\text{ m}^2/\text{s}$. The rationale behind the choice of this value is explained in section 4.2. For all
522 cases, a plane strain assumption is made.

523 **3.2 Step 2 for Seismological Modeling**

524 The next step is to set up the *DF* for the seismological modeling, see figure 3, and this involves two sub-
525 steps, see equation (42). Take cases 2 and 3 for example, the first sub-step is to approximate the *LSDF*
526 shown in figure 2a with a \widehat{LSDF} as the subset A, see figure 3a, by honoring the original locations and
527 orientations. The second sub-step is to construct a *SSSF* in the hosting rock as the subset B, see figure 3b;
528 in principle, this can be derived from a statistical model if data is available ([Jin & Zoback, 2015b](#)). In this
529 example, for simplicity and this does not change the generality of the method, I assign only one fracture
530 to each element center shown in figure 2b as the modeling of fracture locations; for subset A, the
531 orientations are the same as the associated deterministic fracture; for subset B, the orientations are
532 randomly generated following a uniform distribution on $[0, 360^\circ]$. Subsets A and B constitute the
533 complete *DF* for the seismological modeling, see figure 3c. In this process, the fracture length is
534 generated following a well-established scaling relation, which states that the number of fractures within a

535 natural fracture system scales with the fracture length according to a power law (e.g., [Watanabe &](#)
536 [Takahashi, 1995](#); [Bonnet et al., 2001](#); [Johri & Zoback, 2014](#)):

$$537 \quad N = CL^{-D} \quad (50)$$

538 where N is the number of fractures of length L , C is a site-specific constant and D is the so-called *fractal*
539 *dimension* and a typical value is between 1 and 2. In this study, $C=1.6861$ and $D=1.0015$ (further details
540 in section 4.4.2). The generated L is randomly distributed to all fractures shown in figure 3c.

541 On the other hand, the base scenario case 1 is designed not to include any fractures. Instead, the concept
542 of random critical pore pressure ([Shapiro et al., 2005](#)) pre-allocated at seismicity seeds is adopted here.
543 Nevertheless, such seeds can be explicitly visualized as equivalent fractures. The magnitude of the critical
544 pore pressure translates to the fracture orientation with respect to the initial stress state. For calculating
545 source parameters, fracture length is also randomly assigned. Therefore, the above two sub-steps are
546 repeated for case 1. For meaningful comparisons, the locations of the seeds are identical to those in cases
547 2 and 3. In the first sub-step, however, equivalent fracture orientations are random and generated
548 following a uniform distribution. The resulting two subsets of fractures are shown in figures 3d and 3e
549 and the complete DF is shown in figures 3f.

550 In all cases, $\mu_s=0.6$, $\mu_d=0.4$ and a homogenous initial stress tensor $\sigma'_o = \sigma'_{f0} = [15 \ 0; \ 0 \ 5.05]$ MPa is used.
551 The initial effective normal stress and shear stress on all fractures are then calculated, forming a Mohr
552 circle, see figure 4a, where the color indicates the associated initial Coulomb stress CFF_o . The same color
553 scale is used in figure 3 to show the susceptibility of a fracture to slip with respect to σ'_{f0} . The peak and
554 residual frictional strengths, calculated from μ_s and μ_d , respectively, are also shown in figure 4a. Figure 4a
555 also indicates that the domain is nearly critically stressed. Figures 4b and 4c show the distribution of
556 CFF_o , which is no longer uniform, despite a uniform distribution of the fracture orientation.

557 **4. Results**

558 **4.1 Fluid Pressure, Poroelastic Stress and Seismicity**

559 Figures 5 shows four snapshots of the distribution of δp_p (figures 5a-5d) and the associated seismicity
560 (figures 5e-5h) for case 1. The radial outward diffusion of δp_p with a smooth *overpressure front* ([Shapiro](#)
561 [et al., 1997](#)) activates a subset of the pre-seeded seismicity sources where the equivalent critical pore
562 pressure, $\mu_s \times CFF_o$, is breached by δp_p , leading to a similar radially progressive distribution in seismicity.
563 Note here the “front” is a loose term and it refers to an isoline where changes in a quantity become
564 visible. It is important to recognize that this case has one critical difference from the [Shapiro et al. \(2005\)](#)
565 diffusion-only statistical model, that is, instead of using a pre-defined critical pore pressure value
566 following a uniform distribution, it is the pre-defined fractures with uniformly distributed orientations that

567 are used. Because the orientation needs to be transformed through equation (1), the resulting CFF_0 and
 568 the equivalent critical pore pressure, $\mu_s \times CFF_0$, follow instead an exponential distribution, see figure 4b.
 569 Therefore, the modeled seismicity distribution here is indeed different. Also, the addition of the proposed
 570 seismological modeling framework further allows for the calculation of seismic source parameters,
 571 including M_w and $\Delta\tau$ as are shown in figures 5e-5h. Notice, however, that the modeled seismicity
 572 distribution fails to retain the evident linear feature of the pre-allocated source locations (figure 3f),
 573 illustrating a fundamental drawback of this approach.

574 Figure 6 shows the same snapshots of the same two quantities for case 2. Here, the effect of the *LSDF*
 575 (figure 2a) becomes evident. First, δp_p increases primarily along those fractures and secondarily within
 576 the hosting rock, leading to a highly non-smooth overpressure front (figures 6a-6d). Compared to case 1,
 577 δp_p here is of lower magnitude due to the *LSDF* diverting the fluid from the injector. Such a distribution
 578 leads to clear linear clustering of seismicity (figures 6e-6h), a phenomenon frequently observed in the
 579 field (e.g., [Baisch & Harjes, 2003](#); [Stabile et al., 2014](#); [Deichmann et al., 2014](#); [Block et al., 2015](#); [Chen et al., 2018](#);
 580 [Currie et al., 2018](#)). Second, the distribution of seismicity is not coincident with that of δp_p ,
 581 instead, the clustering occurs only along certain fractures. By further examining the fracture orientation
 582 (figure 3a), it can be seen that the seismicity is clustered near those that are well-oriented or sub-well-
 583 oriented with respect to σ'_0 (or σ'_{fp}) and meanwhile subjected to sufficient δp_p .

584 Figure 7 shows the results for case 3. The distribution of δp_p (figures 7a-7d) and the seismicity (figures
 585 7q-7t) are shown together with three poroelastic stress invariants $I_1'/3$ (figures 7e-7h), $\sqrt{J_2}'$ (figures 7i-7l)
 586 and MC (figures 7m-7p). Recall all three quantities are calculated from $\delta\sigma'_p$ under plane strain as
 587 discussed in section 2.3.3. Here, compared to case 2, complex effects of poroelastic coupling are
 588 elucidated. First, the distribution of δp_p is visibly different; the front of δp_p is suppressed and the
 589 magnitude is noticeably lower. Second, the poroelastic normal stress $I_1'/3$ develops, dominantly being
 590 extensional near the fluid-penetrated fractures; however, the magnitude of $I_1'/3$ is lower than that of its
 591 counterpart from the decoupled approach which predicts $I_1'/3 \approx -0.67\delta p_p$ (appendix A.1) using δp_p from
 592 case 2. Third, a pronounced shear stress field $\sqrt{J_2}'$ also develops and influences an even larger portion of
 593 the domain beyond the region subjected to $I_1'/3$ and δp_p , whereas its counterpart in case 2 is 0. Fourth, as
 594 a result, the distribution of MC is different than its counterpart in case 2, which is $0.34 \delta p_p$ (appendix
 595 A.1). Specifically, within the δp_p front (delineated in case 2, not case 3), the magnitude is lower; outside
 596 the δp_p front, it still prevails. This observation has important implications: within the fluid-pressurized
 597 region (i.e., in the near field), poroelastic coupling tends to inhibit seismicity; outside this region (i.e., in
 598 the far field), it can either remotely promote or inhibit seismicity depending on the fracture orientation.
 599 The reason behind the former is that a fracture within the fluid-pressurized region acts as preferred flow
 600 channel, leading to a discontinuous equivalent body force ($-\alpha\nabla\delta p_p$) acting away from it on the two sides,
 601 and therefore, inhibiting shear mode failure by unclamping it ([Chang & Segall, 2016a](#); [Jin & Zoback,](#)

2016b; Jin & Zoback, 2017). This is reflected by the modeled seismicity. Like in case 2, here the seismicity is clustered near fractures favorably oriented with respect to σ'_{θ} (or σ'_{ρ}) and meanwhile subjected to sufficient excess shear stress. Notice the linear clustering is further enhanced by poroelastic coupling. More importantly, the number of events in the near field is substantially reduced. Overall, the event population is reduced to only around a third of that in case 2. These observations are further elaborated in sections 4.2 and 4.3.1.

4.2 Spatial-Temporal Characteristics in the R - T Space

4.2.1 Fluid Pressure and Poroelastic Stress

The spatial-temporal characteristics of the modeled quantities are further illustrated using the so-called R - T plot, where R is the distance from the origin and T is the time since the beginning of the injection. The R - T plots of δp_p for cases 1-3 are given by figure 8. Overlaying are several iso-diffusivity profiles (gray dashed lines) calculated as $R = \sqrt{4\pi D_h T} + 5\text{m}$ where D_h is the hydraulic diffusivity; $\sqrt{4\pi D_h T}$ is a characteristic profile derived from linear diffusion from a Heaviside point source injection in an isotropic, homogeneous and porous-only medium, and it is referred to as the *seismicity triggering front* (Shapiro et al., 1997; Shapiro et al., 2002). Notice the use of such profiles should apply only to case 1 (figure 8a). Nonetheless, for reference, they are also plotted for cases 2 and 3 (figures 8b, 8c), where additionally, the green and magenta lines corresponding to D_h of the hosting rock and the *LSDF*, respectively, are also plotted. It is mentioned in section 3.1 that in case 1, $D_h = 0.03 \text{ m}^2/\text{s}$. This value is chosen such that the modeled δp_p front in the R - T space is approximately the same as that in case 2. In a sense, this value reflects the overall *effective* D_h of the fractured porous media in case 2. Case 1 shows a smooth variation of δp_p in the R - T space. In case 2, however, due to effect of fractures, the variations become non-smooth, in addition to an overall reduction in the magnitude of δp_p . The effect of poroelastic coupling is reflected by comparing case 2 and 3. The δp_p front is slightly suppressed and the magnitude of δp_p is further reduced.

To further illustrate the effect of poroelastic coupling in case 3, here I investigate the R - T characteristics of the poroelastic stress invariants, see figure 9. Although the spatial distributions of $I_1'/3$ and δp_p differ (figures 7a-7h), the delineated fronts of $I_1'/3$ (figure 9a) and δp_p (figure 8c) coincide in the R - T space. This is explained by equation (27), which states that $I_1'/3$, which scales linearly with the volumetric strain $\nabla \cdot \underline{u}_p$, diffuses together with δp_p . Poroelastic coupling does, however, reduce the magnitude of $I_1'/3$ compared to its counterpart $-0.67p$ (appendix A.1) where δp_p is given by figure 8b. The effect of poroelastic coupling further manifests itself in figure 9b, which shows the development of $\sqrt{J_2'}$ one-order of magnitude below p . This cannot be predicted by case 2. Also, it is evidently shown that the delineated front of $\sqrt{J_2'}$ well exceeds those of p and $I_1'/3$ (figures 8c and 9a). Figure 9c results from the combination

635 of figures 9a and 9b. The effect of poroelastic coupling is reflected by its difference in magnitude from its
 636 counterpart $0.34p$ (appendix A.1) where δp_p again is given by figure 8b.

637 4.2.2 Seismicity

638 Figures 10 shows the R - T distribution of the seismicity for cases 1-3 and the color indicates CFF_0 . In
 639 figure 10a, a parabolic seismicity front is clearly delineated for case 1, showing also an evident “lag”
 640 behind the δp_p front (figure 8a). This lag reflects the effect of the initials stress with respect to the static
 641 shear failure line (i.e., the peak strength, see figure 4). Here D_h corresponding to the δp_p front and the
 642 seismicity front are $0.03 \text{ m}^2/\text{s}$ and $0.015 \text{ m}^2/\text{s}$, respectively. In this case, if the seismicity front was to be
 643 used to back calculate D_h (e.g., Shapiro et al., 2002), D_h would be over-estimated by 100%. This motivates
 644 some nonlinear diffusion-based interpretations which incorporate pressure-dependent D_h (e.g., Hummel &
 645 Shapiro, 2012; Hummel & Shapiro, 2013). Here, my model is mechanics-based and it does not require the
 646 somewhat equivocal definition of “relatively large” pressure which underlines the diffusion-only
 647 statistical models (Shapiro et al., 1997). The effect of the $LSDF$ can be seen in figure 10b. Notice the
 648 increased curvature of the parabolic seismicity front, which is above the predicted characteristic profile
 649 (second grey dashed line from the top) earlier and near the injector but below this profile later and away
 650 from the injector. Hummel & Shapiro (2013) used a power-law type of pressure-dependent D_h to correct
 651 for this change. However, my model not only produces this change but also introduces additional
 652 heterogeneity. Figure 10c shows further variations by accounting for poroelastic coupling. Compared to
 653 figure 10b, here the number of events is greatly reduced, the heterogeneity becomes much more
 654 pronounced, and some “outliers” are present. These are remotely triggered events to be elaborated in
 655 section 4.3.1. Additionally, nearly all events are sourced from favorably oriented fractures. The result of
 656 case 3 also shows qualitative agreement with a dataset provided in Hummel & Shapiro (2013).

657 4.3 Event Analysis

658 4.3.1 Near-Field and Remote Events (Coupled Case 3)

659 As has been discussed in section 4.2, poroelastic coupling tends to inhibit seismicity in the fluid-
 660 pressurized area but is also capable of triggering events remotely. Such effects are further illustrated here.
 661 To this end, the pressure front used here is defined as an iso-line on which δp_p is 1% of the maximum
 662 pressure, which is the prescribed constant injection pressure p_g in this study. The pressure front
 663 demarcates the near field and the far field, the latter assumed devoid of any pressure influence. Seismicity
 664 outside the pressure front is considered remotely triggered by only the remote poroelastic stress that is
 665 simply defined as the excess poroelastic shear stress outside the pressure front,

$$666 \quad RS := H(0.01p_g - \delta p_p)MC \quad (51)$$

667 where H is the Heaviside function, MC is given by equation (37), and p_g is the fluid Dirichlet boundary
668 condition (i.e., injection pressure in this study).

669 Figures 11a – 11h are eight time slices illustrating the evolution of remote events (blue) occurring in the
670 far field (area colored by remote stress) in relation to the remaining events (magenta) located within the
671 near field (non-colored area). In each time slice, only events occurred at that time are shown. Over time,
672 poroelastic coupling inhibits near-field events and reduces their population while increasingly triggering
673 more events remotely. This transition of triggering style is further shown by figure 11i where the relative
674 sizes of the remote and near-field event populations are compared. Finally, figure 11j is the corresponding
675 R - T plot of the remote poroelastic stress superposed with near-field and remote seismicity. The space-
676 time is partitioned into two regimes, one dominated by remote triggering and the other, near-field
677 triggering. The transition, however, is non-smooth due to the presence of the $LSDF$.

678 4.3.2 Repeating Events

679 The detection of repeating events in induced seismicity catalogs have been documented by many studies
680 across scales (e.g., Baisch & Harjes, 2003; Moriya et al., 2003; Deichmann et al., 2014; Lengliné et al.,
681 2014; Duverger et al, 2015; Zaliapin & Ben-Zion, 2016; Hakso & Zoback, 2017; Cochran et al., 2018).
682 Identification of repeaters requires using cross correlation measurements to locate hypocenters as well as
683 robustly constraining rupture dimensions (e.g., Ellsworth & Bulut, 2018). Admittedly, true repeaters with
684 centroid separations less than rupture dimensions are difficult to search for, especially in small-magnitude
685 event catalogs. Nevertheless, they can be theoretically predicted. Indeed, the proposed modeling
686 framework here offers a natural way to modeling repeaters - shear stress loss on and around a source fault
687 can be compensated by poroelastic stress, provided with right combinations of fault orientations and
688 poroelastic stressing history, and this process can be driven through multiple seismic cycles. This theory is
689 especially suited for induced seismicity where fluid clearly plays a role. Here, the modeled repeater
690 groups are shown figure 12. Each location indicates a doublet pair or a multiplet group (e.g., Poupinet et
691 al., 1984; Waldhauser & Ellsworth, 2002) which contains two or more events that occur on the same
692 source location but at different time; for visibility, a small-magnitude event is always plotted within a big-
693 magnitude one (see the concentric circles). The repeating events exhibit some characteristics in space
694 similar as those discussed in section 4.1. For example, the overall distribution is radial in case 1 but are
695 clustered near favorably oriented fractures subjected to sufficient δp_p in case 2 and MC in case 3. Despite
696 the difference in the spatial pattern, the number of repeater groups and the total number of events are
697 similar between cases 1 and 2. In case 3, however, both drop significantly, suggesting poroelastic
698 coupling inhibits the occurrence of repeating events as it does to the overall seismicity. Finally, within
699 each group, an earlier event does not necessarily have a larger magnitude; the contrary is not uncommon.
700 This is due to the complex stress path and the non-full degree of stress drop as is reflected by the r in
701 equation (46). To see this, for each case, I chose one representative fracture that has generated the most

702 repeating events and plot the associated complete stress path colored with time, see figure 13. In each
 703 case, δp_p or MC suffice to drive a fracture through multiple seismic cycles within 90 minutes. However,
 704 the decoupled approach tends to over-predict both the number of seismic cycles and the number of
 705 repeater groups. Notice the increasingly unfavorable orientation of the fracture from cases 3 to 1.
 706 Additionally, within each seismic cycle, poroelastic coupling leads to a nonlinear stress path in case 3 as
 707 opposed to a linear leftward one in case 1 or 2.

708 Additionally, I analyze the number of events within each group and the associated inter-event time (i.e.,
 709 inter-seismic time), see figure 14. From figures 14a, 14c and 14e, one observes that in all cases, the
 710 repeating events are primarily doublet pairs; multiplet groups are present, and the number of events within
 711 these groups suggests that δp_p can drive a fracture through up to 8 seismic cycles within the simulated 90
 712 minutes of injection; this number is reduced if poroelastic coupling is considered. For the entire catalog,
 713 the inter-event time between any two consecutive repeating events are compiled. The results are plotted in
 714 figures 14b, 14d and 14f and they all exhibit a Poisson distribution described by $Pr=e^{-\lambda} \lambda^t / (t!)$, where Pr is
 715 the probability density function, λ is the average number of repeating events per time interval and t is the
 716 time interval (here I acknowledge a slight violation in notation; λ also means the Lamé's constant in
 717 equation (48)). Observations of such distributions have also been reported for real datasets (e.g.,
 718 [Langenbruch et al., 2011](#); [Cochran et al., 2018](#)). The best-fitting λ with a 95% confidence and the
 719 associated probability density function are shown in figure 15. Overall, variations appear small among the
 720 cases, suggesting insignificant impact of fractures and poroelastic coupling on the inter-event time.

721 4.3.3 Triggered and Induced Events

722 In figure 1, the distinction between triggered and induced events is made based on the initial stress on a
 723 fracture in relation to its peak and residual frictional strengths. This is a quantitative definition and it reads

$$724 \quad \sqrt{\|\boldsymbol{\sigma}'_{f0} \cdot \underline{n}_f\|^2 - (\boldsymbol{\sigma}'_{f0} : \underline{n}_f \otimes \underline{n}_f)^2} \leq \mu_d (\boldsymbol{\sigma}'_{f0} : \underline{n}_f \otimes \underline{n}_f), \quad \textit{induced} \quad (52)$$

$$\mu_d (\boldsymbol{\sigma}'_{f0} : \underline{n}_f \otimes \underline{n}_f) < \sqrt{\|\boldsymbol{\sigma}'_{f0} \cdot \underline{n}_f\|^2 - (\boldsymbol{\sigma}'_{f0} : \underline{n}_f \otimes \underline{n}_f)^2} \leq \mu_s (\boldsymbol{\sigma}'_{f0} : \underline{n}_f \otimes \underline{n}_f), \quad \textit{triggered}$$

725 Equation (52) states that from a loading point of view, the key difference between the two lies in that an
 726 induced event represents shear failure on a fault that is otherwise tectonically inactive with respect to the
 727 background stress state, whereas a triggered event is indicative of a fault that is nevertheless expected to
 728 produce an earthquake given the background stress state but the process towards failure is favorably
 729 accelerated. This definition is consistent with the qualitative one provided by [McGarr & Simpson \(1997\)](#).
 730 As a result, upon seismicity, a triggered event releases a substantial amount of tectonic stress whereas an
 731 induced event releases mostly anthropogenic stress.

732 The triggered and induced events are distinguished from each other according to the above definition. The
 733 results are shown in figure 16. In cases 1-3, 93.3%, 92.8% and 98.5% of the events are triggered; the
 734 remaining small number of events are induced and are distributed in close proximity to the injector, as
 735 they occur on unfavorably-oriented fractures and require a significant amount of δp_p or MC to be
 736 activated. Again, for either type of event, accounting for the *LSDF* leads to the clustering and accounting
 737 for poroelastic coupling significantly reduces the number of events.

738 4.4 Source Parameters

739 4.4.1 Stress Drop, Fracture Length and Moment Magnitude

740 Figures 17a, 17c and 17e summarize the modeled seismic source characteristics in the parameter space for
 741 cases 1-3. For each event, M_w is plotted against the associated fracture length L and colored with $\Delta\tau$. The
 742 modeled events, with M_w between -3 and -1, occur on fractures of L ranging from 0.1m and 10m, and $\Delta\tau$
 743 ranges from below 0.1 MPa to above 1 MPa, consistent with many real induced micro-earthquake
 744 datasets at a similar scale (e.g., [Goertz-Allmann et al., 2011](#); [Mukuhira, 2013](#)). Such source characteristics
 745 overall seem not affected by the *LSDF* nor poroelastic coupling. For a realistic range of $\Delta\tau$, the parameter
 746 r in equation (46) turns out to be a key controlling factor and the sensitivity of model outcomes to r
 747 remains to be explored. I will leave this for future work. Figures 17b, 17d and 17f further show the overall
 748 similar distribution of $\Delta\tau$ for cases 1-3. In each case, [0.1, 1] MPa is the dominant range. Notice, however,
 749 that case 3 sees a bigger portion of events with higher $\Delta\tau$ (e.g., above 1 MPa). The reason underlies
 750 nonlinear poroelastic loading paths with upward components, which lead to larger $\Delta\tau_{max}$ (equation (47))
 751 compared to decoupled cases, see also figures 1 and 13c.

752 4.4.2 Magnitude-Frequency Scaling

753 I have introduced a power law that describes the commonly observed scaling relation between the fracture
 754 length and the frequency (section 3.2). Meanwhile, earthquakes in nature are characterized with a
 755 universal statistical relation between the magnitude and the cumulative frequency, namely the Gutenberg-
 756 Richter law ([Gutenberg, 1956](#)), which reads:

$$757 \lg N(m > M_w) = a - bM_w \quad (53)$$

758 where $N(m > M_w)$ is the total number of events with a moment magnitude m above M_w , and a and b are
 759 constants.

760 In nature, the fractal dimension D shown in equation (50) is observed to be mostly between 1 and 2 (e.g.,
 761 [Okubo & Aki, 1987](#)). The b -value fitted from natural earthquake catalogs is commonly around 1 (e.g., [Shi
 762 & Bolt, 1982](#)) albeit a wide possible range of variations from 0.3 to 2.5, see, e.g., [El-Isa & Eaton \(2014\)](#)
 763 for a comprehensive review. Studies suggest that D and b are inherently related. For example, [Hirata
 764 \(1989\)](#) suggests a well-recognized $D = 2b$ relation. A somewhat curious yet common observation is that

765 for induced seismicity, especially microseismicity as is modeled here, b -value is frequently elevated
766 above 1 and even 2 (e.g., Vermilyen & Zoback, 2011; Bachmann et al., 2011; Bachmann et al., 2012;
767 Eaton et al., 2014; Tutuncu & Bui, 2015; Mousavi et al., 2017; Chen et al., 2018; Brudzinski &
768 Kozłowska et al., 2019), although a uni-modal distribution around 1 (Schoenball et al., 2015; Goertz-
769 Allmann, 2017) and a bi-modal distribution around both 1 and 2 (Igonin et al., 2018; Kettlety et al., 2019)
770 have also been reported.

771 In figure 18, for each case, the distribution of lengths of all fractures (figures 3c, 3f) is plotted (green),
772 together with the power law fitting line (magenta); the distribution of lengths of the activated subset of
773 fractures is also plotted (red), which clearly no longer obeys the power law decay, owing to that only
774 favorably oriented fractures are induced to slip. Nonetheless, the magnitude-frequency scaling relation
775 still holds for the induced events, as is illustrated in figure 19. For each case, the distribution of M_w , which
776 primarily varies between -3.5 and -1.0, is shown as the histogram (yellow green); the total number of
777 events (i.e., cumulative frequency) is shown by the blue-green dots, which is then used to fit the
778 Gutenberg-Richter law, yielding a b -value around 2. Notice the similarities among all three cases in both
779 figures 18 and 19, suggesting that the b -value is likely to be independent from the *LSDF* and poroelastic
780 coupling. The breaking-down in the power law distribution of the length of the activated subset of
781 fractures might be responsible for the deviation in the b -value for induced seismicity. Similar mechanical
782 origins of the b -value elevation for induced seismicity have been suggested by other studies (Tafti et al.,
783 2013; Stormo et al., 2015). In the end, the specific b -value might be jointly determined by the fracture
784 network itself (Eaton et al., 2014; Afshari Moein et al., 2018), the poroelastic properties (Wangen, 2019)
785 and the stress state (Scholz, 2015).

786 **5.Summary and Conclusions**

787 I have developed a hydro-mechanical-seismological modeling framework for fluid perturbation-induced
788 seismicity in a fluid-saturated and arbitrarily fractured nonlinear poroelastic medium. Following
789 predefined distributions characteristic of a natural fracture system, a dual network of fractures is
790 generated consisting large-scale deterministic fractures (*LSDF*) and small-scale stochastic fractures
791 (*SSSF*) within the hosting rock. The modeling consists two steps, including first the quasi-static fracture-
792 poro-mechanical modeling and second the seismological modeling. In the first step, only the *LSDF* is
793 resolved, using a fluid-solid fully coupled nonlinear computational poromechanical model customized for
794 arbitrarily fractured media. This provides a *LSDF*-controlled full poroelastic stress tensor as a pivotal
795 input for the second step, in which the complete dual network of fractures is then considered. The
796 seismicity-induced shear stress loss on a source fracture is stochastically generated as a static quantity
797 without explicitly modeling the co-seismic dynamic rupture; it is dictated by the full poroelastic stressing
798 history in conjunction with the initial stress state. A prediction-correction type of fracture stress updating

799 scheme is developed accordingly and advanced in time to produce seismicity catalogs. Three progressive
 800 cases were designed to systematically showcase model capabilities as well as effects of fractures and full
 801 poroelastic coupling on the resulting fluid overpressure, solid stress as well as seismicity and its source
 802 characteristics. Compared to the prevalent fracture-free, coupling-free and diffusion-only class of
 803 statistical models, my model produces induced seismicity with more realistic spatial-temporal and
 804 statistical characteristics frequently seen in real data. It also goes beyond the scope of most current
 805 models and provides a synthetic catalog of induced events, allowing for analyzing seismic source
 806 characteristics and establishing connections between observations and model physics.

807 Several key new findings from the numerical experiments are highlighted here.

808 (1) The spatial-temporal evolution of the pore fluid overpressure δp_p , the change in the solid effective
 809 stress tensor $\delta \sigma'_p$, the associated stress invariants I_1' and $\sqrt{J_2'}$ and the excess shear stress invariant
 810 $MC = \sqrt{J_2'} - \sin(\phi)I_1'/3$, all differ in a porous medium, a fractured porous medium and a fractured
 811 poroelastic medium. In space, the presence of the hydraulically conductive *LSDF* leads to marked
 812 localization of these quantities around it. Poroelastic coupling tends to reduce the magnitude of δp_p and I_1'
 813 near fluid-penetrated fractures but also predicts an otherwise non-existing $\sqrt{J_2'}$ within the entire domain.
 814 As a result of, MC is reduced in the near field but increased in the far field. In the R - T space, δp_p and I_1'
 815 share the same front which is below the front shared by $\sqrt{J_2'}$ and MC .

816 (2) In space, the *LSDF* leads to not only heterogeneity but also pronounced linear clustering in seismicity.
 817 The clustering occurs only near fractures favorably oriented with respect the initial stress and meanwhile
 818 subjected to sufficient excess shear stress. Poroelastic coupling further enhances the clustering; more
 819 importantly, because of the way it generates the excess shear stress, poroelastic coupling inhibits
 820 seismicity in the near field and promotes events remotely in the far field. The style of triggering is
 821 dominated by near-field triggering at an earlier time and transitions into remote triggering-dominated
 822 subsequently. Overall, poroelastic coupling significantly reduces the event population.

823 (3) External fluid perturbations and internal seismicity are the two sources driving stress changes, and
 824 together they can drive a source fracture through multiple seismic cycles on a time scale relevant to the
 825 problem. This provides a viable mechanism of fluid-induced repeating events with characteristic stepwise
 826 stress paths. Poroelastic coupling, however, tends to inhibit the occurrence of repeaters as it does to the
 827 overall seismicity, in addition to adding nonlinearity to the associated stress paths.

828 (4) Although collectively referred to as induced seismicity, the modeled events are indeed predominantly
 829 triggered events rather than induced events. Because the latter are sourced on unfavorably-oriented
 830 fractures that require significant excess shear stress, they concentrate near the source of fluid
 831 perturbations.

832 (5) Some statistical characteristics of induced seismicity appear to remain independent from the *LSDF*
 833 and poroelastic coupling. For the given set of parameters, the inter-event time between two consecutive
 834 repeater follows a Poisson's distribution, the stress drop $\Delta\tau$ predominantly falls in between 0.1 MPa and 1
 835 MPa obeying overall similar distributions and the b -value in the magnitude-frequency scaling relation is
 836 consistently around 2, irrespective of the case. However, poroelastic coupling does favor higher $\Delta\tau$ due to
 837 its upward bending of the stress path, leading to some slight differences in the distributions of $\Delta\tau$ and M_w
 838 near the end of their distribution intervals.

839 (6) In the complete dual fracture system, the fracture length and the frequency obey a realistic power law
 840 scaling relation with a characteristic fractal dimension; however, this relation breaks down for the
 841 activated subset of fractures since only favorably-oriented fractures are induced to slip. This mechanical
 842 origin might explain the curious deviation of the b -value from 1 to above 2 as has been commonly seen in
 843 induced seismicity catalogs.

844 **Acknowledgement**

845 I thank Norm Sleep, William Ellsworth and Apostolos Sarlis for discussion. The work is partially funded
 846 by the Stanford Center for Induced and Triggered Seismicity. No data were used in producing this
 847 manuscript.

848 **Appendix**

849 **A.1 Equivalent Poroelastic Stress Invariants for Cases 1 & 2**

850 For case 3, equations (35) - (37) are used to calculate $I_1'/3$, $\sqrt{J_2}'$ and MC shown in figure 7. For cases 1
 851 and 2 without the coupling effect, the pressure changes within the hosting from external fluid
 852 perturbations can be translated to an equivalent change in its effective normal stress change as $\alpha\delta p_p \mathbf{1}$. This
 853 is similar to equation (3) except for the use of Biot-Willis coefficient of the hosting rock. Substituting it
 854 into equations (35) and (36) yields the following equivalent poroelastic stress invariants,

$$855 \quad \frac{1}{3}I_1' = -\frac{2}{3}(1+\nu)\alpha\delta p_p \quad (\text{A1})$$

$$856 \quad \sqrt{J_2}' = 0 \quad (\text{A2})$$

857 Given the parameters used in this study, specifically, $\nu = 0.25$, $\alpha = 0.8$ and $\mu_s = 0.6$, equation (A1) predicts
 858 that $I_1'/3 \approx -0.67\delta p_p$ and $MC = \sqrt{J_2}' - \sin(\phi)I_1'/3 \approx 0.34\delta p_p$ for cases 1 and 2.

859 **Nomenclature**

1. Domains

Ω_f, Ω_m	fracture domain and hosting rock (matrix) domain
$\partial\Omega_f$	fracture domain boundary
∂f	fracture-hosting rock interface (also dimensionally reduced fracture domain)
$\Omega, \bar{\Omega}$	bulk model domain and its mixed-dimensional representation
$L\overline{SDF}, \widehat{L\overline{SDF}}$	a large-scale deterministic fracture network and its discrete approximation
$SSSF$	a small-scale stochastic fracture network
DF	a dual-scale fracture network
F_l, N	l^{th} large-scale deterministic fracture in $L\overline{SDF}$, total population
f_a, n_a	a^{th} discrete fracture in $\widehat{L\overline{SDF}}$, total population
f_b, n_b	b^{th} discrete fracture in $SSSF$, total population

2. Fracture domain properties & variables

CFF	Coulomb Failure Function (Coulomb stress), Pa
$ \tau_f , \tau_{f0} $	current and initial maximum shear stress, Pa
$ \tau_{f0} + \delta\tau_f $	current maximum shear stress showing decompositions, Pa
$\sigma'_{nf}, \sigma'_{nf0}, \delta\sigma'_{nf}$	current, initial and perturbing effective normal stress, Pa
\underline{n}_f	unit normal vector, [-]
μ_s, μ_d	static and dynamic frictional coefficients, [-]
σ_f	current Cauchy total stress tensor, Pa
$\sigma'_f, \sigma'_{f0}, \delta\sigma'_f$	current, initial and perturbing effective stress tensors, Pa
$\delta\sigma'_{fp}, \delta\sigma'_{fs}$	changes in the effective stress tensor due to external fluid perturbations and seismicity, Pa
$\delta\sigma'_{fxx}, \delta\sigma'_{fyy}, \delta\sigma'_{fzz}$	normal components of $\delta\sigma'_f$, Pa
$\delta\sigma'_{fxy}, \delta\sigma'_{fxz}, \delta\sigma'_{fyz}$	shear components of $\delta\sigma'_f$, Pa
$p_f, p_{f0}, \delta p_f$	current and initial fluid pressure and fluid overpressure, Pa
$\delta p_{fp}, \delta p_{fs}$	fluid overpressure due to external fluid perturbations and seismicity, Pa
b_0	initial hydraulic aperture, m
C_f	compressibility, Pa^{-1}
$\Delta\tau_j, \Delta\tau_{jmax}$	static shear stress drop from the j^{th} episode of slip and its maximum likely value, Pa
r	a random variable, [-]
L, W	length and width, m
D	fractal dimension, [-]
C	a site-specific parameter for characterizing fracture length distributions, [-]

3. Porous hosting rock (matrix) domain properties & variables

K_m	bulk modulus of solid grains/skeleton, Pa
K_b	bulk modulus, Pa

α	Biot-Willis coefficient, [-]
ϕ_{m0}	initial porosity, [-]
C_m	compressibility, Pa ⁻¹
λ, μ	Lame's constant and shear modulus, Pa
ϕ	frictional angle, °
\mathbf{k}_m	permeability tensor, m ²
$\boldsymbol{\sigma}, \boldsymbol{\sigma}_0, \delta\boldsymbol{\sigma}$	current, initial and perturbing Cauchy total stress tensors, Pa
$\delta\boldsymbol{\sigma}_p, \delta\boldsymbol{\sigma}_s$	changes in the Cauchy total stress tensor due to external fluid perturbations and seismicity, Pa
$\delta\boldsymbol{\sigma}'_p, \delta p_p$	changes in the effective stress tensor and fluid overpressure due to external fluid perturbations, Pa
$I_1', \sqrt{J_2'}$	first and second poroelastic stress invariants, Pa
MC	excess poroelastic shear stress, Pa
RS	remote poroelastic stress, Pa
$\delta\boldsymbol{u}_p$	change in the displacement vector due to external fluid perturbations, m
\mathbf{D}	elastic stiffness tensor, Pa

4. Other properties and variables

\boldsymbol{v}	fluid velocity vector, m/s
η	fluid viscosity, Pa·s
s	external fluid source/sink term divided by the initial fluid density, s ⁻¹
Λ_0	geometric factor reflecting effects of fractures on medium fluid storage capacity, [-]
p_g	fluid Dirichlet boundary value (injection pressure), Pa
M_0	seismic moment, N·m
M_w	moment magnitude, [-]
a, b	Gutenberg-Richter constants, [-]

5. Numerical discretization (fractures)

\mathbf{M}_{F_I}	fluid storage capacity matrix of the I^{th} large-scale deterministic fracture
\mathbf{K}_{F_I}	hydraulic conductivity matrix of the I^{th} large-scale deterministic fracture

6. Numerical discretization (hosting rock/matrix)

$\tilde{\mathbf{M}}, \mathbf{M}$	fluid storage capacity matrix in the absence and presence of fractures
\mathbf{K}	hydraulic conductivity matrix
\mathbf{C}	coupling matrix
\mathbf{G}	elastic stiffness matrix
\mathbf{Q}	a matrix for extracting fracture nodal pressure from matrix nodal pressure in a hybrid-dimensional approach
\mathbf{B}	standard finite element displacement-strain transformation matrix

$\hat{\xi}_p, \underline{d}_p$	nodal values of δp_p and $\delta \underline{u}_p$
$\underline{F}_1, \underline{F}_2, \underline{F}_3$	external nodal mass vectors
\underline{Y}	external nodal force vector
$\underline{R}_2, \underline{R}_3$	residual vectors

7. Math operators & identities

$tr(\cdot)$	trace (diagonal sum)
$H(\cdot)$	Heaviside function
$\nabla, \nabla^{(s)}, \nabla_\tau$	gradient, symmetric gradient and tangential gradient operators
$\nabla \cdot$	divergence operator
\cdot	dot product
$:$	double tensor contraction
\otimes	Dyadic product
$\mathbf{1}$	unit identity (Kronecker delta)

860

861 Reference

- 862 Afshari Moein, M. J., Tormann, T., Valley, B., & Wiemer, S. (2018). Maximum magnitude forecast in hydraulic
863 stimulation based on clustering and size distribution of early microseismicity. *Geophysical Research*
864 *Letters*, 45(14), 6907-6917.
- 865 Gómez Alba, S., Vargas, C. A., & Zang, A. (2020). Evidencing the relationship between injected volume of water
866 and maximum expected magnitude during the Puerto Gaitán (Colombia) earthquake sequence from 2013 to
867 2015. *Geophysical Journal International*, 220(1), 335-344.
- 868 Almakari, M., Dublanchet, P., Chauris, H., & Pellet, F. (2019). Effect of the Injection Scenario on the Rate and
869 Magnitude Content of Injection - Induced Seismicity: Case of a Heterogeneous Fault. *Journal of Geophysical*
870 *Research: Solid Earth*, 124(8), 8426-8448.
- 871 Altmann, J. B., Müller, B. I. R., Müller, T. M., Heidbach, O., Tingay, M. R. P., & Weißhardt, A. (2014). Pore
872 pressure stress coupling in 3D and consequences for reservoir stress states and fracture
873 reactivation. *Geothermics*, 52, 195-205.
- 874 Andrews, D. J. (1976). Rupture velocity of plane strain shear cracks. *Journal of Geophysical Research*, 81(32),
875 5679-5687.
- 876 Angus, D. A., Kendall, J. M., Fisher, Q. J., Segura, J. M., Skachkov, S., Crook, A. J. L., & Dutko, M. (2010).
877 Modelling microseismicity of a producing reservoir from coupled fluid-flow and geomechanical simulation.
878 *Geophysical Prospecting*, 58(5), 901-914.
- 879 Bachmann, C. E., Wiemer, S., Goertz - Allmann, B. P., & Woessner, J. (2012). Influence of pore - pressure on the
880 event - size distribution of induced earthquakes. *Geophysical Research Letters*, 39(9).
- 881 Bachmann, C. E., Wiemer, S., Woessner, J., & Hainzl, S. (2011). Statistical analysis of the induced Basel 2006
882 earthquake sequence: introducing a probability-based monitoring approach for Enhanced Geothermal
883 Systems. *Geophysical Journal International*, 186(2), 793-807.
- 884 Baisch, S., & Harjes, H. P. (2003). A model for fluid-injection-induced seismicity at the KTB,
885 Germany. *Geophysical Journal International*, 152(1), 160-170.

- 886 Baisch, S., Vörös, R., Rotherth, E., Stang, H., Jung, R., & Schellschmidt, R. (2010). A numerical model for fluid
887 injection induced seismicity at Soultz-sous-Forêts. *International Journal of Rock Mechanics and Mining*
888 *Sciences*, 47(3), 405-413.
- 889 Barbour, A. J., Norbeck, J. H., & Rubinstein, J. L. (2017). The effects of varying injection rates in Osage County,
890 Oklahoma, on the 2016 M w 5.8 Pawnee earthquake. *Seismological Research Letters*, 88(4), 1040-1053.
- 891 Berkowitz, B. (2002). Characterizing flow and transport in fractured geological media: A review. *Advances in Water*
892 *Resources*, 25(8), 861-884.
- 893 Biot, M. A. (1941). General theory of three - dimensional consolidation. *Journal of applied physics*, 12(2), 155-164.
- 894 Block, L. V., Wood, C. K., Yeck, W. L., & King, V. M. (2015). Induced seismicity constraints on subsurface
895 geological structure, Paradox Valley, Colorado. *Geophysical Journal International*, 200(2), 1172-1195.
- 896 Bonnet, E., Bour, O., Odling, N. E., Davy, P., Main, I., Cowie, P., & Berkowitz, B. (2001). Scaling of fracture
897 systems in geological media. *Reviews of Geophysics*, 39(3), 347-383.
- 898 Booker, J. R., & Carter, J. P. (1986). Analysis of a point sink embedded in a porous elastic half space. *International*
899 *Journal for Numerical and Analytical Methods in Geomechanics*, 10(2), 137-150.
- 900 Borja, R. I. (2006). On the mechanical energy and effective stress in saturated and unsaturated porous
901 continua. *International Journal of Solids and Structures*, 43(6), 1764-1786.
- 902 Borja, R. I. (2013). *Plasticity: modeling & computation*. Berlin: Springer.
- 903 Brudzinski, M. R., & Kozłowska, M. (2019). Seismicity induced by hydraulic fracturing and wastewater disposal in
904 the Appalachian Basin, USA: a review. *Acta Geophysica*, 67(1), 351-364.
- 905 Byerlee, J. (1978). Friction of rocks. In *Rock friction and earthquake prediction* (pp. 615-626). Basel: Birkhäuser.
- 906 Carcione, J. M., Currenti, G., Johann, L., & Shapiro, S. (2018). Modeling fluid injection induced microseismicity in
907 shales. *Journal of Geophysics and Engineering*, 15(1), 234.
- 908 Carcione, J. M., Da Col, F., Currenti, G., & Cantucci, B. (2015). Modeling techniques to study CO₂-injection
909 induced micro-seismicity. *International Journal of Greenhouse Gas Control*, 42, 246-257.
- 910 Chang, K. W., & Segall, P. (2016a). Injection - induced seismicity on basement fractures including poroelastic
911 stressing. *Journal of Geophysical Research: Solid Earth*, 121(4), 2708-2726.
- 912 Chang, K. W., & Segall, P. (2016b). Seismicity on basement fractures induced by simultaneous fluid injection–
913 extraction. *Pure and Applied Geophysics*, 173(8), 2621-2636.
- 914 Chang, K. W., & Segall, P. (2017). Reduction of Injection-Induced Pore-Pressure and Stress in Basement Rocks
915 Due to Basal Sealing Layers. *Pure and Applied Geophysics*, 174(7), 2649-2661.
- 916 Chang, K. W., & Yoon, H. (2018). 3 - D Modeling of Induced Seismicity Along Multiple Faults: Magnitude, Rate,
917 and Location in a Poroelasticity System. *Journal of Geophysical Research: Solid Earth*, 123(11), 9866-9883.
- 918 Chen, H., Meng, X., Niu, F., Tang, Y., Yin, C., & Wu, F. (2018). Microseismic monitoring of stimulating shale gas
919 reservoir in SW China: 2. Spatial clustering controlled by the preexisting faults and fractures. *Journal of*
920 *Geophysical Research: Solid Earth*, 123(2), 1659-1672.
- 921 Cleary, M. P. (1977). Fundamental solutions for a fluid-saturated porous solid. *International Journal of Solids and*
922 *Structures*, 13(9), 785-806.
- 923 Cochran, E. S., Ross, Z. E., Harrington, R. M., Dougherty, S. L., & Rubinstein, J. L. (2018). Induced earthquake
924 families reveal distinctive evolutionary patterns near disposal wells. *Journal of Geophysical Research: Solid*
925 *Earth*, 123(9), 8045-8055.
- 926 Cryer, C. W. A. (1963). A comparison of the three-dimensional consolidation theories of Biot and Terzaghi. *The*
927 *Quarterly Journal of Mechanics and Applied Mathematics*, 16(4), 401-412.

- 928 Currie, B. S., Free, J. C., Brudzinski, M. R., Leveridge, M., & Skoumal, R. J. (2018). Seismicity induced by
929 wastewater injection in Washington County, Ohio: influence of preexisting structure, regional stress regime,
930 and well operations. *Journal of Geophysical Research: Solid Earth*, 123(5), 4123-4140.
- 931 Deichmann, N., Kraft, T., & Evans, K. F. (2014). Identification of fractures activated during the stimulation of the
932 Basel geothermal project from cluster analysis and focal mechanisms of the larger magnitude
933 events. *Geothermics*, 52, 84-97.
- 934 Deichmann, N., Kraft, T., & Evans, K. F. (2014). Identification of faults activated during the stimulation of the
935 Basel geothermal project from cluster analysis and focal mechanisms of the larger magnitude
936 events. *Geothermics*, 52, 84-97.
- 937 Dempsey, D., & Suckale, J. (2017). Physics - based forecasting of induced seismicity at Groningen gas field, the
938 Netherlands. *Geophysical Research Letters*, 44(15), 7773-7782.
- 939 Deng, K., Liu, Y., & Harrington, R. M. (2016). Poroelastic stress triggering of the December 2013 Crooked Lake,
940 Alberta, induced seismicity sequence. *Geophysical Research Letters*, 43(16), 8482-8491.
- 941 Dieterich, J. (1994). A constitutive law for rate of earthquake production and its application to earthquake
942 clustering. *Journal of Geophysical Research: Solid Earth*, 99(B2), 2601-2618.
- 943 Dieterich, J. H., Richards - Dinger, K. B., & Kroll, K. A. (2015). Modeling injection - induced seismicity with the
944 physics - based earthquake simulator RSQSim. *Seismological Research Letters*, 86(4), 1102-1109.
- 945 Dunham, E. M., & Rice, J. R. (2008). Earthquake slip between dissimilar poroelastic materials. *Journal of*
946 *Geophysical Research: Solid Earth*, 113(B9).
- 947 Duverger, C., Godano, M., Bernard, P., Lyon - Caen, H., & Lambotte, S. (2015). The 2003 - 2004 seismic swarm in
948 the western Corinth rift: Evidence for a multiscale pore pressure diffusion process along a permeable fracture
949 system. *Geophysical Research Letters*, 42(18), 7374-7382.
- 950 Eaton, D. W., Davidsen, J., Pedersen, P. K., & Boroumand, N. (2014). Breakdown of the Gutenberg - Richter
951 relation for microearthquakes induced by hydraulic fracturing: influence of stratabound fractures. *Geophysical*
952 *Prospecting*, 62(Vertical Seismic Profiling and Microseismicity Frontiers), 806-818.
- 953 El-Isa, Z. H., & Eaton, D. W. (2014). Spatiotemporal variations in the b-value of earthquake magnitude-frequency
954 distributions: Classification and causes. *Tectonophysics*, 615, 1-11.
- 955 Ellsworth, W. L., & Bulut, F. (2018). Nucleation of the 1999 Izmit earthquake by a triggered cascade of
956 foreshocks. *Nature Geoscience*, 11(7), 531-535.
- 957 Fan, Z., Eichhubl, P., & Gale, J. F. (2016). Geomechanical analysis of fluid injection and seismic fault slip for the
958 Mw4. 8 Timpson, Texas, earthquake sequence. *Journal of Geophysical Research: Solid Earth*, 121(4), 2798-
959 2812.
- 960 Goebel, T. H. W., Weingarten, M., Chen, X., Haffener, J., & Brodsky, E. E. (2017). The 2016 Mw5. 1 Fairview,
961 Oklahoma earthquakes: Evidence for long-range poroelastic triggering at > 40 km from fluid disposal
962 wells. *Earth and Planetary Science Letters*, 472, 50-61.
- 963 Goertz-Allmann, B. P., & Wiemer, S. (2012). Geomechanical modeling of induced seismicity source parameters and
964 implications for seismic hazard assessment. *Geophysics*, 78(1), KS25-KS39.
- 965 Goertz - Allmann, B. P., Gibbons, S. J., Oye, V., Bauer, R., & Will, R. (2017). Characterization of induced
966 seismicity patterns derived from internal structure in event clusters. *Journal of Geophysical Research: Solid*
967 *Earth*, 122(5), 3875-3894.
- 968 Goertz - Allmann, B. P., Goertz, A., & Wiemer, S. (2011). Stress drop variations of induced earthquakes at the
969 Basel geothermal site. *Geophysical Research Letters*, 38(9).
- 970 Gutenberg, B. (1956). The energy of earthquakes. *Quarterly Journal of the Geological Society*, 112(1-4), 1-14.

- 971 Hakso, A., & Zoback, M. (2017). Utilizing multiplets as an independent assessment of relative microseismic
972 location uncertainty. *The Leading Edge*, 36(10), 829-836.
- 973 Hanks, T. C., & Boore, D. M. (1984). Moment - magnitude relations in theory and practice. *Journal of Geophysical*
974 *Research: Solid Earth*, 89(B7), 6229-6235.
- 975 Hardebol, N. J., Maier, C., Nick, H., Geiger, S., Bertotti, G., & Boro, H. (2015). Multiscale fracture network
976 characterization and impact on flow: A case study on the Latemar carbonate platform. *Journal of Geophysical*
977 *Research: Solid Earth*, 120(12), 8197-8222.
- 978 He, J., Rui, Z., & Ling, K. (2016). A new method to determine Biot's coefficients of Bakken samples. *Journal of*
979 *Natural Gas Science and Engineering*, 35, 259-264.
- 980 Hirata, T. (1989). A correlation between the b value and the fractal dimension of earthquakes. *Journal of*
981 *Geophysical Research: Solid Earth*, 94(B6), 7507-7514.
- 982 Hirthe, E. M., & Graf, T. (2015). Fracture network optimization for simulating 2D variable-density flow and
983 transport. *Advances in Water Resources*, 83, 364-375.
- 984 Hopp, C., Sewell, S., Mroczek, S., Savage, M., & Townend, J. (2020). Seismic response to evolving injection at the
985 Rotokawa geothermal field, New Zealand. *Geothermics*, 85, 101750.
- 986 Hornby, B.E., The elastic properties of shales, Ph.D. dissertation, University of Cambridge, Cambridge, England,
987 1995.
- 988 Hughes, T. J. (2012). *The finite element method: linear static and dynamic finite element analysis*. Courier
989 Corporation.
- 990 Hummel, N., & Shapiro, S. A. (2012). Microseismic estimates of hydraulic diffusivity in case of non-linear fluid-
991 rock interaction. *Geophysical Journal International*, 188(3), 1441-1453.
- 992 Hummel, N., & Shapiro, S. A. (2013). Nonlinear diffusion-based interpretation of induced microseismicity: A
993 Barnett Shale hydraulic fracturing case study. *Geophysics*, 78(5), B211-B226.
- 994 Igonin, N., Zecevic, M., & Eaton, D. W. (2018). Bilinear Magnitude - Frequency Distributions and Characteristic
995 Earthquakes During Hydraulic Fracturing. *Geophysical Research Letters*, 45(23), 12-866.
- 996 Izadi, G., & Elsworth, D. (2014). Reservoir stimulation and induced seismicity: Roles of fluid pressure and thermal
997 transients on reactivated fractured networks. *Geothermics*, 51, 368-379.
- 998 Jin, L., & Zoback, M. D. (2015a). An Analytical Solution for Depletion-induced Principal Stress Rotations In 3D
999 and its Implications for Fracture Stability. In *AGU Fall Meeting Abstracts*.
- 1000 Jin, L., & Zoback, M. D. (2015b). Identification of fracture-controlled damage zones in microseismic data—an
1001 example from the Haynesville shale. *SEG Technical Program Expanded Abstracts 2015*, 726-730.
- 1002 Jin, L., & Zoback, M. D. (2016a). Including a stochastic discrete fracture network into one-way coupled
1003 poromechanical modeling of injection-induced shear re-activation. In *50th US Rock Mechanics/Geomechanics*
1004 *Symposium*. American Rock Mechanics Association.
- 1005 Jin, L., & Zoback, M. D. (2016b). Impact of Poro-Elastic Coupling and Stress Shadowing on Injection-Induced
1006 Microseismicity in Reservoirs Embedded With Discrete Fracture Networks. In *AAPG Annual Convention and*
1007 *Exhibition*.
- 1008 Jin, L., & Zoback, M. D. (2017). Fully Coupled Nonlinear Fluid Flow and Poroelasticity in Arbitrarily Fractured
1009 Porous Media: A Hybrid - Dimensional Computational Model. *Journal of Geophysical Research: Solid*
1010 *Earth*, 122(10), 7626-7658.
- 1011 Jin, L., & Zoback, M. D. (2018a). Modeling Induced Seismicity: Co-Seismic Fully Dynamic Spontaneous Rupture
1012 Considering Fault Poroelastic Stress. In *52nd US Rock Mechanics/Geomechanics Symposium*. American Rock
1013 Mechanics Association.

- 1014 Jin, L., & Zoback, M. D. (2018b). Fully Dynamic Spontaneous Rupture Due to Quasi - Static Pore Pressure and
1015 Poroelastic Effects: An Implicit Nonlinear Computational Model of Fluid - Induced Seismic Events. *Journal of*
1016 *Geophysical Research: Solid Earth*, 123(11), 9430-9468.
- 1017 Jin, L., & Zoback, M. D. (2019). Depletion-Induced Poroelastic Stress Changes in Naturally Fractured
1018 Unconventional Reservoirs and Implications for Hydraulic Fracture Propagation. *In SPE Annual Technical*
1019 *Conference and Exhibition. Society of Petroleum Engineers*.
- 1020 Johann, L., Dinske, C., & Shapiro, S. A. (2016). Scaling of seismicity induced by nonlinear fluid - rock interaction
1021 after an injection stop. *Journal of Geophysical Research: Solid Earth*, 121(11), 8154-8174.
- 1022 Johri, M., Zoback, M. D., & Hennings, P. (2014). A scaling law to characterize fracture-damage zones at reservoir
1023 depths Fracture Damage Zones at Depth. *AAPG Bulletin*, 98(10), 2057-2079.
- 1024 Kanamori, H., & Anderson, D. L. (1975). Theoretical basis of some empirical relations in seismology. *Bulletin of*
1025 *the seismological society of America*, 65(5), 1073-1095.
- 1026 Keranen, K.M. & Weingarten, M. (2018). Induced Seismicity. *Annual Review of Earth and Planetary Sciences*. 46,
1027 149-174.
- 1028 Kettlety, T., Verdon, J. P., Werner, M. J., Kendall, J. M., & Budge, J. (2019). Investigating the role of elastostatic
1029 stress transfer during hydraulic fracturing-induced fault activation. *Geophysical Journal International*, 217(2),
1030 1200-1216.
- 1031 Kroll, K. A., Richards - Dinger, K. B., & Dieterich, J. H. (2017). Sensitivity of induced seismic sequences to rate -
1032 and - state frictional processes. *Journal of Geophysical Research: Solid Earth*, 122(12), 10-207.
- 1033 Langenbruch, C., & Zoback, M. D. (2016). How will induced seismicity in Oklahoma respond to decreased
1034 saltwater injection rates?. *Science advances*, 2(11), e1601542.
- 1035 Langenbruch, C., Dinske, C., & Shapiro, S. A. (2011). Inter event times of fluid induced earthquakes suggest their
1036 Poisson nature. *Geophysical Research Letters*, 38(21).
- 1037 Langenbruch, C., Weingarten, M., & Zoback, M. D. (2018). Physics-based forecasting of man-made earthquake
1038 hazards in Oklahoma and Kansas. *Nature communications*, 9(1), 3946.
- 1039 Lengliné, O., Lamourette, L., Vivin, L., Cuenot, N., & Schmittbuhl, J. (2014). Fluid - induced earthquakes with
1040 variable stress drop. *Journal of Geophysical Research: Solid Earth*, 119(12), 8900-8913.
- 1041 Ma, X., & Zoback, M. D. (2017). Laboratory experiments simulating poroelastic stress changes associated with
1042 depletion and injection in low - porosity sedimentary rocks. *Journal of Geophysical Research: Solid*
1043 *Earth*, 122(4), 2478-2503.
- 1044 Maillot, B., Nielsen, S., & Main, I. (1999). Numerical simulation of seismicity due to fluid injection in a brittle
1045 poroelastic medium. *Geophysical Journal International*, 139(2), 263-272.
- 1046 Mandel, J. (1953). Consolidation des sols (étude mathématique). *Geotechnique*, 3(7), 287-299.
- 1047 McGarr, Arthur F. and Simpson, David (1997). A broad look at induced and triggered seismicity. *In: Rockburst and*
1048 *seismicity in mines* (pp. 385-396). Rotterdam: Balkema.
- 1049 Megies, T., & Wassermann, J. (2014). Microseismicity observed at a non-pressure-stimulated geothermal power
1050 plant. *Geothermics*, 52, 36-49.
- 1051 Moriya, H., Niitsuma, H., & Baria, R. (2003). Multiplet-clustering analysis reveals structural details within the
1052 seismic cloud at the Soultz geothermal field, France. *Bulletin of the Seismological Society of America*, 93(4),
1053 1606-1620.
- 1054 Mousavi, S. M., Ogwari, P. O., Horton, S. P., & Langston, C. A. (2017). Spatio-temporal evolution of frequency-
1055 magnitude distribution and seismogenic index during initiation of induced seismicity at Guy-Greenbrier,
1056 Arkansas. *Physics of the Earth and Planetary Interiors*, 267, 53-66.

- 1057 Mukuhira, Y., Asanuma, H., Niitsuma, H., & Häring, M. O. (2013). Characteristics of large-magnitude microseismic
1058 events recorded during and after stimulation of a geothermal reservoir at Basel, Switzerland. *Geothermics*, 45,
1059 1-17.
- 1060 Mukuhira, Y., Dinske, C., Asanuma, H., Ito, T., & Häring, M. O. (2017). Pore pressure behavior at the shut - in
1061 phase and causality of large induced seismicity at Basel, Switzerland. *Journal of Geophysical Research: Solid
1062 Earth*, 122(1), 411-435.
- 1063 Norbeck, J. H., & Rubinstein, J. L. (2018). Hydromechanical earthquake nucleation model forecasts onset, peak, and
1064 falling rates of induced seismicity in Oklahoma and Kansas. *Geophysical Research Letters*, 45(7), 2963-2975.
- 1065 Nur, A., & Byerlee, J. (1971). An exact effective stress law for elastic deformation of rock with fluids. *Journal of
1066 geophysical research*, 76(26), 6414-6419.
- 1067 Okubo, P. G., & Aki, K. (1987). Fractal geometry in the San Andreas fracture system. *Journal of Geophysical
1068 Research: Solid Earth*, 92(B1), 345-355.
- 1069 Postma, T., & Jansen, J. D. (2018). The Small Effect of Poroelastic Pressure Transients on Triggering of
1070 Production - Induced Earthquakes in the Groningen Natural Gas Field. *Journal of Geophysical Research: Solid
1071 Earth*, 123(1), 401-417.
- 1072 Poupinet, G., Ellsworth, W. L., & Frechet, J. (1984). Monitoring velocity variations in the crust using earthquake
1073 doublets: An application to the Calaveras Fracture, California. *Journal of Geophysical Research: Solid
1074 Earth*, 89(B7), 5719-5731.
- 1075 Raziperchikolaee, S., Alvarado, V., & Yin, S. (2014). Microscale modeling of fluid flow - geomechanics -
1076 seismicity: Relationship between permeability and seismic source response in deformed rock joints. *Journal of
1077 Geophysical Research: Solid Earth*, 119(9), 6958-6975.
- 1078 Rice, J. R., & Cleary, M. P. (1976). Some basic stress diffusion solutions for fluid - saturated elastic porous media
1079 with compressible constituents. *Reviews of Geophysics*, 14(2), 227-241.
- 1080 Richards - Dinger, K., & Dieterich, J. H. (2012). RSQSim earthquake simulator. *Seismological Research
1081 Letters*, 83(6), 983-990.
- 1082 Riffraction, J., Dempsey, D., Archer, R., Kelkar, S., & Karra, S. (2016). Understanding Poroelastic Stressing and
1083 Induced Seismicity with a Stochastic/Deterministic Model: an Application to an EGS Stimulation at Paralana,
1084 South Australia, 2011. In *Proc. 41st Stanford Workshop on Geothermal Reservoir Engineering*, SGP-TR-209.
- 1085 Rothert, E., & Shapiro, S. A. (2007). Statistics of fracture strength and fluid - induced microseismicity. *Journal of
1086 Geophysical Research: Solid Earth*, 112(B4).
- 1087 Rudnicki, J. W. (1986). Fluid mass sources and point forces in linear elastic diffusive solids. *Mechanics of
1088 Materials*, 5(4), 383-393.
- 1089 Schoenball, M., Davatzes, N. C., & Glen, J. M. (2015). Differentiating induced and natural seismicity using space -
1090 time - magnitude statistics applied to the Coso Geothermal field. *Geophysical Research Letters*, 42(15), 6221-
1091 6228.
- 1092 Scholz, C. H. (2015). On the stress dependence of the earthquake b value. *Geophysical Research Letters*, 42(5),
1093 1399-1402.
- 1094 Scuderi, M. M., & Collettini, C. (2016). The role of fluid pressure in induced vs. triggered seismicity: Insights from
1095 rock deformation experiments on carbonates. *Scientific Reports*, 6, 24852.
- 1096 Segall, P. (1985). Stress and subsidence resulting from subsurface fluid withdrawal in the epicentral region of the
1097 1983 Coalinga earthquake. *Journal of Geophysical Research: Solid Earth*, 90(B8), 6801-6816.
- 1098 Segall, P. (1989). Earthquakes triggered by fluid extraction. *Geology*, 17(10), 942-946.
- 1099 Segall, P. (2010). *Earthquake and volcano deformation*. NJ: Princeton University Press.

- 1100 Segall, P., & Fitzgerald, S. D. (1998). A note on induced stress changes in hydrocarbon and geothermal
1101 reservoirs. *Tectonophysics*, 289(1), 117-128.
- 1102 Segall, P., & Lu, S. (2015). Injection - induced seismicity: Poroelastic and earthquake nucleation effects. *Journal of*
1103 *Geophysical Research: Solid Earth*, 120(7), 5082-5103.
- 1104 Segall, P., Grasso, J. R., & Mossop, A. (1994). Poroelastic stressing and induced seismicity near the Lacq gas field,
1105 southwestern France. *Journal of Geophysical Research: Solid Earth*, 99(B8), 15423-15438.
- 1106 Shapiro, S. A., Dinske, C., Langenbruch, C., & Wenzel, F. (2010). Seismogenic index and magnitude probability of
1107 earthquakes induced during reservoir fluid stimulations. *The Leading Edge*, 29(3), 304-309.
- 1108 Shapiro, S. A., Huenges, E., & Borm, G. (1997). Estimating the crust permeability from fluid - injection - induced
1109 seismic emission at the KTB site. *Geophysical Journal International*, 131(2).
- 1110 Shapiro, S. A., Rentsch, S., & Rothert, E. (2005). Characterization of hydraulic properties of rocks using probability
1111 of fluid-induced microearthquakes. *Geophysics*, 70(2), F27-F33.
- 1112 Shapiro, S. A., Rothert, E., Rath, V., & Rindschwentner, J. (2002). Characterization of fluid transport properties of
1113 reservoirs using induced microseismicity. *Geophysics*, 67(1), 212-220.
- 1114 Shi, Y., & Bolt, B. A. (1982). The standard error of the magnitude-frequency b value. *Bulletin of the Seismological*
1115 *Society of America*, 72(5), 1677-1687.
- 1116 Skoumal, R. J., Ries, R., Brudzinski, M. R., Barbour, A. J., & Currie, B. S. (2018). Earthquakes induced by
1117 hydraulic fracturing are pervasive in Oklahoma. *Journal of Geophysical Research: Solid Earth*, 123(12), 10-
1118 918.
- 1119 Stabile, T. A., Giocoli, A., Perrone, A., Piscitelli, S., & Lapenna, V. (2014). Fluid injection induced seismicity
1120 reveals a NE dipping fracture in the southeastern sector of the High Agri Valley (southern Italy). *Geophysical*
1121 *Research Letters*, 41(16), 5847-5854.
- 1122 Stark, M. A., & Davis, S. D. (1996). Remotely triggered microearthquakes at The Geysers geothermal field,
1123 California. *Geophysical research letters*, 23(9), 945-948.
- 1124 Stormo, A., Lengliné, O., & Schmittbuhl, J. (2015). Mechanical origin of b-value changes during stimulation of
1125 deep geothermal reservoirs. *Geothermal Energy*, 3(1), 1.
- 1126 Tafti, T. A., Sahimi, M., Aminzadeh, F., & Sammis, C. G. (2013). Use of microseismicity for determining the
1127 structure of the fracture network of large-scale porous media. *Physical Review E*, 87(3), 032152.
- 1128 Tarrahi, M., & Jafarpour, B. (2012). Inference of permeability distribution from injection - induced discrete
1129 microseismic events with kernel density estimation and ensemble Kalman filter. *Water Resources*
1130 *Research*, 48(10).
- 1131 Terakawa, T. (2014). Evolution of pore fluid pressures in a stimulated geothermal reservoir inferred from
1132 earthquake focal mechanisms. *Geophysical Research Letters*, 41(21), 7468-7476.
- 1133 Terakawa, T., Miller, S. A., & Deichmann, N. (2012). High fluid pressure and triggered earthquakes in the enhanced
1134 geothermal system in Basel, Switzerland. *Journal of Geophysical Research: Solid Earth*, 117(B7).
- 1135 Terzaghi, Karl (1936). Relation Between Soil Mechanics and Foundation Engineering: Presidential
1136 Address. *Proceedings, First International Conference on Soil Mechanics and Foundation Engineering, Boston*.
1137 3, 13-18.
- 1138 Tung, S., & Masterlark, T. (2018). Delayed poroelastic triggering of the 2016 October Visso earthquake by the
1139 August Amatrice earthquake, Italy. *Geophysical Research Letters*, 45(5), 2221-2229.
- 1140 Tutuncu, A. N., & Bui, B. T. (2015). Coupled geomechanical and fluid flow modeling for injection induced
1141 seismicity prediction. In *SEG Technical Program Expanded Abstracts 2015* (pp. 4848-4852). Society of
1142 Exploration Geophysicists.

- 1143 Van Wees, J. D., Buijze, L., Van Thienen-Visser, K., Nepveu, M., Wassing, B. B. T., Orlic, B., & Fokker, P. A.
1144 (2014). Geomechanics response and induced seismicity during gas field depletion in the
1145 Netherlands. *Geothermics*, 52, 206-219.
- 1146 Verdon, J. P., Stork, A. L., Bissell, R. C., Bond, C. E., & Werner, M. J. (2015). Simulation of seismic events
1147 induced by CO₂ injection at In Salah, Algeria. *Earth and Planetary Science Letters*, 426, 118-129.
- 1148 Vermynen, J., & Zoback, M. D. (2011, January). Hydraulic fracturing, microseismic magnitudes, and stress
1149 evolution in the Barnett Shale, Texas, USA. In *SPE Hydraulic Fracturing Technology Conference*. Society of
1150 Petroleum Engineers.
- 1151 Vujević, K., Graf, T., Simmons, C. T., & Werner, A. D. (2014). Impact of fracture network geometry on free
1152 convective flow patterns. *Advances in Water Resources*, 71, 65-80.
- 1153 Waldhauser, F., & Ellsworth, W. L. (2002). Fracture structure and mechanics of the Hayward fracture, California,
1154 from double - difference earthquake locations. *Journal of Geophysical Research: Solid Earth*, 107(B3).
- 1155 Wang, R., & Kumpel, H. J. (2003). Poroelasticity: Efficient modeling of strongly coupled, slow deformation
1156 processes in a multilayered half-space. *Geophysics*, 68(2), 705-717.
- 1157 Wangen, M. (2019). A 3D model of hydraulic fracturing and microseismicity in anisotropic stress
1158 fields. *Geomechanics and Geophysics for Geo-Energy and Geo-Resources*, 5(1), 17-35.
- 1159 Wassing, B. B. T., Van Wees, J. D., & Fokker, P. A. (2014). Coupled continuum modeling of fracture reactivation
1160 and induced seismicity during enhanced geothermal operations. *Geothermics*, 52, 153-164.
- 1161 Watanabe, K., & Takahashi, H. (1995). Fractal geometry characterization of geothermal reservoir fracture
1162 networks. *Journal of Geophysical Research: Solid Earth*, 100(B1), 521-528.
- 1163 White, J. A., & Borja, R. I. (2011). Block-preconditioned Newton–Krylov solvers for fully coupled flow and
1164 geomechanics. *Computational Geosciences*, 15(4), 647.
- 1165 Yeck, W. L., Weingarten, M., Benz, H. M., McNamara, D. E., Bergman, E. A., Herrmann, R. B., ... & Earle, P. S.
1166 (2016). Far - field pressurization likely caused one of the largest injection induced earthquakes by reactivating a
1167 large preexisting basement fracture structure. *Geophysical Research Letters*, 43(19).
- 1168 Yoon, J. S., Zang, A., & Stephansson, O. (2014). Numerical investigation on optimized stimulation of intact and
1169 naturally fractured deep geothermal reservoirs using hydro-mechanical coupled discrete particles joints model.
1170 *Geothermics*, 52, 165-184.
- 1171 Yu, H., Harrington, R. M., Liu, Y., & Wang, B. (2019). Induced Seismicity Driven by Fluid Diffusion Revealed by
1172 a Near - Field Hydraulic Stimulation Monitoring Array in the Montney Basin, British Columbia. *Journal of*
1173 *Geophysical Research: Solid Earth*, 124(5), 4694-4709.
- 1174 Zaliapin, I., & Ben - Zion, Y. (2016). Discriminating characteristics of tectonic and human - induced
1175 seismicity. *Bulletin of the Seismological Society of America*, 106(3), 846-859.
- 1176 Zbinden, D., Rinaldi, A. P., Urpi, L., & Wiemer, S. (2017). On the physics - based processes behind production -
1177 induced seismicity in natural gas fields. *Journal of Geophysical Research: Solid Earth*, 122(5), 3792-3812.
- 1178 Zhao, X., & Paul Young, R. (2011). Numerical modeling of seismicity induced by fluid injection in naturally
1179 fractured reservoirs. *Geophysics*, 76(6), WC167-WC180.
- 1180 Zoback, M. D., & Zinke, J. C. (2002). Production-induced normal fractureing in the Valhall and Ekofisk oil fields.
1181 *In The Mechanism of Induced Seismicity* (pp. 403-420). Basel: Birkhäuser.

1182 Figure Captions

1183 **Figure 1.** Schematic illustration (not to scale) of the hydro-mechanical-seismological modeling of fluid-
 1184 induced seismicity plotted in the fracture effective normal stress-shear stress space. Based on the peak and
 1185 residual frictional strengths of a fracture, as are depicted by the red and green lines, the space is divided
 1186 into two parts defining the initial stress regime for a triggered event and an induced event, respectively (to
 1187 be elaborated in section 4.3.3). The blue and magenta dots are given as two examples, both located on a
 1188 Mohr circle defined by σ'_{f0} . For either type of event, the modeling consists two steps. The first step is to
 1189 predict the fracture stress by compensating the fracture with σ'_{fp} , which requires the pore pressure
 1190 modeling for case 1, the fracture-pore pressure modeling for case 2 and the fracture-poro-mechanical
 1191 modeling for case 3, the latter two resolving the *LSDF*. The outcome of this step is indicated by the green
 1192 and red arrows. The second step, which does not vary among the three cases, is to stochastically model $\Delta\tau$
 1193 on source fracture as indicated by the dashed arrows to approximately account for the effect of σ'_{fs} ;
 1194 meanwhile, $\Delta\tau$ remains constrained on a range $\Delta\tau_{\max}$ as is indicated by the yellow arrows and it is
 1195 computed from the poroelastic loading history σ'_{fp} in conjunction with σ'_{f0} . Two consecutive seismic
 1196 cycles j and $j+1$ are shown, and the complete stress updating scheme is given in list 1.

1197 **Figure 2.** (a) The model domain for cases 2 and 3. It consists of a *LSDF* embedded within an otherwise
 1198 porous matrix. The color suggests the index I (see equation (21)). For case 1, the *LSDF* is removed from
 1199 the domain. (b) Conforming space discretization of the fractured domain and the resulting unstructured
 1200 triangular finite elements used in arriving at the semi-discrete forms. For case 3, all elements represent the
 1201 porous hosting rock; the grey elements are the standard two-field (fluid pressure, solid displacement)
 1202 mixed FE elements; the colored elements are ‘hybrid’ mixed elements in which at least one edge is also
 1203 used as a lower-dimensional element to discretize the fractures; the color of an element indicates the I^{th}
 1204 deterministic fracture with which it is associated. If a hybrid element conforms to multiple fractures, only
 1205 the largest I is used for coloring. For case 2, the elements have similar meanings as in case 3 except they
 1206 are no longer mixed (i.e., only used for interpolating the fluid pressure). For case 1, all elements are the
 1207 standard single-field elements. Adapted from Jin & Zoback (2017).

1208 **Figure 3.** The dual fracture network (*DF*, equation (42)) consisting of 12800 fractures used for the
 1209 seismicity modeling, shown together with its two subsets A and B. (a)-(c) Cases 2 and 3, and (d)-(f) case
 1210 1. In case 1, fractures are essentially explicit visualizations of seismicity seeds assigned with random
 1211 critical pore pressure values. Figures 3a shows the subset A with deterministic fracture locations and
 1212 orientations as an approximation to the *LSDF* shown in figure 2a; figure 3b shows the subset B as a
 1213 stochastic realization of fractures in the hosting rock; figure 3c shows the hybrid deterministic-stochastic
 1214 *DF* in which the fracture length distribution follows a realistic power-law scaling relation. Figures 3d-3f
 1215 resemble figures 3a-3c except for the stochastic fracture orientation in figure 3d. In all figures, the warm

1216 color indicates the fracture is favorably oriented with respect to σ'_{f0} whereas the cool color indicates
 1217 otherwise.

1218 **Figure 4.** The initial stress used for the seismological modeling. In figure 4a, the initial effective normal
 1219 stress and shear stress on all fractures (figures 3c, 3f) are plotted. Because the fractures sample all likely
 1220 orientations, a Mohr circle is formed. The color indicates CFF_0 . The peak and the residual strengths are
 1221 also shown for reference (same as those in figure 1). The geometric meaning of CFF_0 is shown for one
 1222 fracture as an example. Figures 4b, 4c show the histograms of CFF_0 for case 1 and cases 2-3,
 1223 respectively.

1224 **Figure 5.** Snapshots of the spatial distribution of the modeled quantities at four time steps for case 1. (a)-
 1225 (d) The fluid overpressure δp_p and (e)-(f) the seismicity sized with M_w and colored with $\Delta\tau$. Only the 100
 1226 m \times 100 m area around the center is shown. The time is indicated at the top of each plot.

1227 **Figure 6.** Same as figure 5, but for case 2. The *LSDF* is shown in the background.

1228 **Figure 7.** Snapshots of the spatial distribution of the modeled quantities at four time steps for case 3. (a)-
 1229 (d) The fluid overpressure δp_p , (e)-(h) the first poroelastic stress invariant $I_1'/3$, (i)-(l) the second
 1230 deviatoric poroelastic stress invariant $\sqrt{J_2'}$, (m)-(p) the excess poroelastic shear stress invariant $MC=\sqrt{J_2'}$ -
 1231 $\sin(\phi)I_1'/3$ and (q)-(t) the seismicity sized with M_w and colored with $\Delta\tau$. Only the 100 m \times 100 m area
 1232 around the center is shown. The time is indicated at the top of each plot. The *LSDF* is shown in the
 1233 background.

1234 **Figure 8.** Space-time plots of the fluid overpressure δp_p . (a) Case 1, (b) case 2 and (c) case 3. The
 1235 distance is only plotted from 0 to 45 m. The color scale is the same as in figures 5-7. Several
 1236 characteristic diffusion profiles are shown (see text) as references, including the green and magenta lines
 1237 calculated using the diffusivity of the hosting rock and the fractures, respectively. The differences
 1238 between cases 1 and 2 show the effect of the *LSDF* and the differences between cases 2 and 3 show the
 1239 effect of poroelastic coupling.

1240 **Figure 9.** Space-time plots of the poroelastic stress invariants for case 3. (a) $I_1'/3$, (b) $\sqrt{J_2'}$ and (c)
 1241 $MC=\sqrt{J_2'}$ - $\sin(\phi)I_1'/3$. The distance is only plotted from 0 to 45 m and the characteristic diffusion profiles
 1242 are the same as those in figure 13. The color scale is the same as figure 8. The counterparts of the three
 1243 quantities in case 2 without the coupling effect can be obtained by multiplying the δp_p in figure 8b with -
 1244 0.67, 0 and 0.34 (appendix A.1).

1245 **Figure 10.** Space-time plots of all seismic events, sized with M_w and colored with CFF_0 . (a), (d) Case 1,
 1246 (b), (e) case 2 and (c), (f) case 3. The distance is only plotted from 0 to 45 m and the reference
 1247 characteristic diffusion profiles are the same as those in figure 13. The differences between cases 1 and 2

1248 show the effect of the *LSDF* and the differences between cases 2 and 3 show the effect of poroelastic
1249 coupling.

1250 **Figure 11.** Evolution of near-field events versus remotely triggered events in the fully coupled case 3. (a)
1251 - (h) Snapshots of the distribution of remotely triggered events (blue dots) overlaying areas undergoing
1252 poroelastic stressing (magnitude shown by the color) and negligible pressure changes, together with near-
1253 field events (magenta dots) overlaying areas (non-colored) where pore pressure changes are present. (i)
1254 The population of remote events (blue) relative to that of near-field events (magenta) plotted against time.
1255 Over time, the predominant triggering style transitions from near-field triggering to remote triggering. (j)
1256 *R-T* plot of the remote stress superposed with seismicity. The colored domain indicates possible space-
1257 time for remote triggering whereas non-colored domain indicates space-time for near-field triggering.
1258 Near-field events dominates at smaller distances and earlier time while remote events take over at greater
1259 distance and later time.

1260 **Figure 12.** Repeating events sized with M_w and colored with t_0 . (a) Case 1, (b) case 2 and (c) case 3. Only
1261 the $100\text{ m} \times 100\text{ m}$ area around the center is shown. The number of groups and the total number of events
1262 are indicated at the top left. The *LSDF* in the background for cases 2 and 3.

1263 **Figure 13.** Representative complete stress paths. (a) Case 1, (b) case 2 and (c) case 3. The color indicates
1264 the time. The number of seismic cycles is 6 in cases 1 and 2 and 3 in case 3. The pore pressure effect and
1265 the poroelastic effect are indicated.

1266 **Figure 14.** Characteristics of the repeating events. (a)-(b) Case 1, (c)-(d) case 2 and (e)-(f) case 3. Figures
1267 14a, 14c and 14e show the location of each group containing repeating events, colored with the number of
1268 events within that group (i.e., the number of seismic cycles the associated fracture has undergone).
1269 Figures 14b, 14d and 14f are histograms showing the distribution of the inter-event time between two
1270 consecutive repeating events.

1271 **Figure 15.** Poisson's distribution of the inter-event time between consecutive repeating events and the
1272 associated parameters.

1273 **Figure 16.** Triggered and induced events sized with M_w and colored with t_0 . (a)-(b) Case 1, (c)-(d) case 2
1274 and (e)-(f) case 3. Only the $100\text{ m} \times 100\text{ m}$ area around the center is shown. The number of events is
1275 indicated at the top left. The *LSDF* is shown in the background.

1276 **Figure 17.** The top row shows relationships among M_w , L and $\Delta\tau$ of all modeled events. Overlaying are
1277 four contours corresponding to $\Delta\tau=0.01\text{ MPa}$, 0.1 MPa , 1 MPa and 10 MPa . The bottom row shows the
1278 histograms of $\Delta\tau$ together with the cumulative frequency using 1000 equal-sized bins on the range $[0.01,$
1279 $10]\text{ MPa}$. Additionally, the number of events with $\Delta\tau \leq 0.01\text{ MPa}$, $0.01\text{ MPa} < \Delta\tau \leq 0.1\text{ MPa}$, $0.1\text{ MPa} < \Delta\tau \leq 1$

1280 MPa and $\Delta\tau > 1$ MPa are counted and the percentages are shown. (a), (b) Case 1, (c), (d) case 2 and (e), (f)
1281 case 3.

1282 **Figure 18.** Histogram of fracture lengths using 1000 equal-sized bins, plotted on a log-log scale as
1283 discrete sequences. The green sequence indicates the distribution of lengths of all fractures, which follows
1284 a power law decay as is fitted with the magenta line. The fitting parameters are also shown, specifically,
1285 the fractal dimension D is 1. The red sequence shows the length distribution of activated fractures only
1286 (fractures undergone at least one seismic cycle). Because it is primarily the favorably oriented fractures
1287 that are activated, the distribution no longer follows a power law decay. (a) Case 1, (b) case 2 and (c) case
1288 3.

1289 **Figure 19.** Histogram of the modeled M_w (yellow green). The bin size is 0.05, and the y-axis is on a log-
1290 scale. The associated distribution of N follows the classic Gutenberg-Richter law (blue green); data points
1291 with a M_w above -2 are used for fitting (the magenta line), yielding a b -value around 2, which is
1292 commonly observed for induced micro-seismicity. (a) Case 1, (b) case 2 and (c) case 3.

Figure 1.

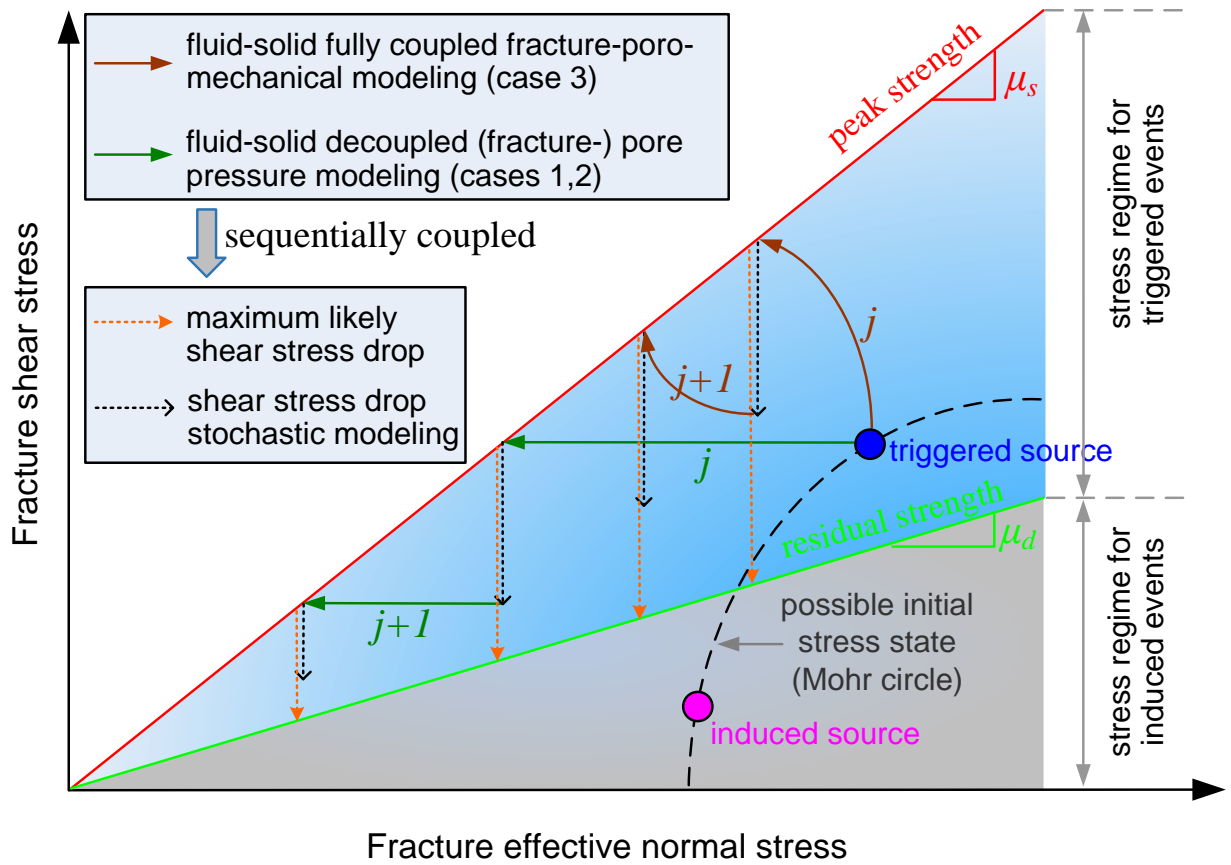


Figure 2.

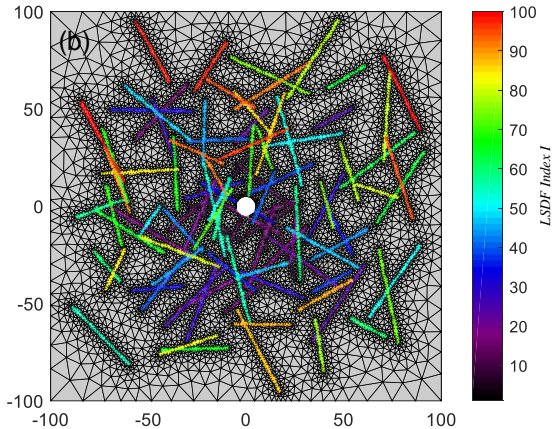
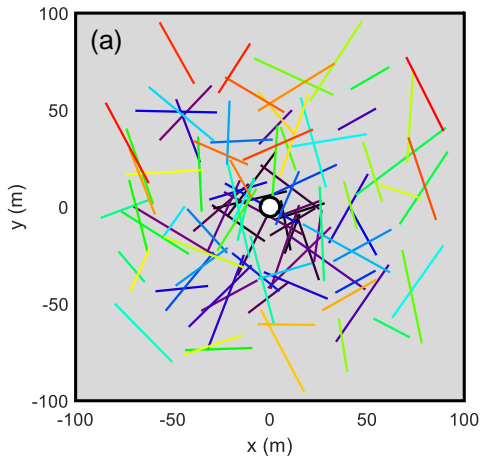


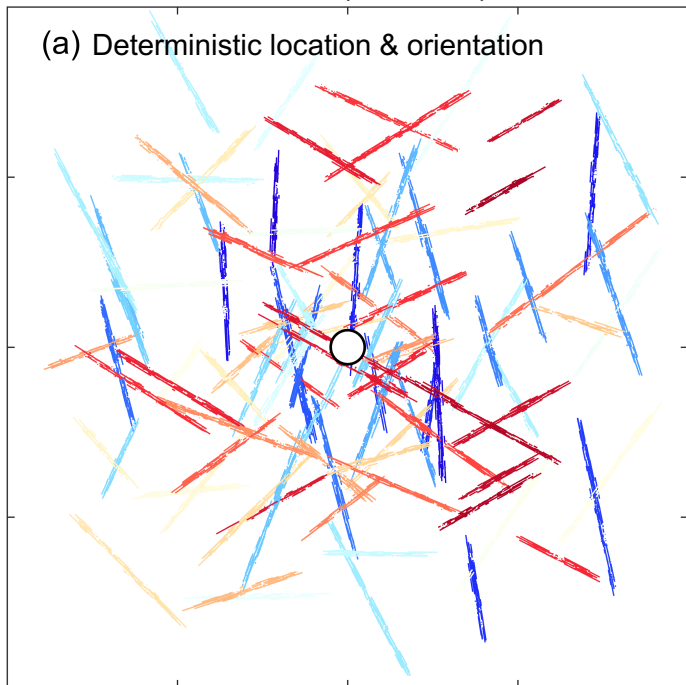
Figure 3.

Subset A (Case 2,3)

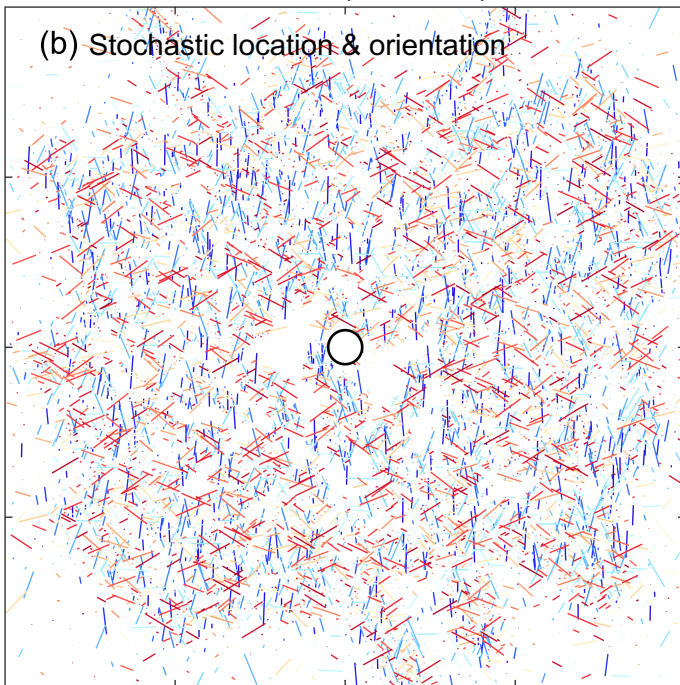
Subset B (Case 2,3)

Subsets A & B (Case 2,3)

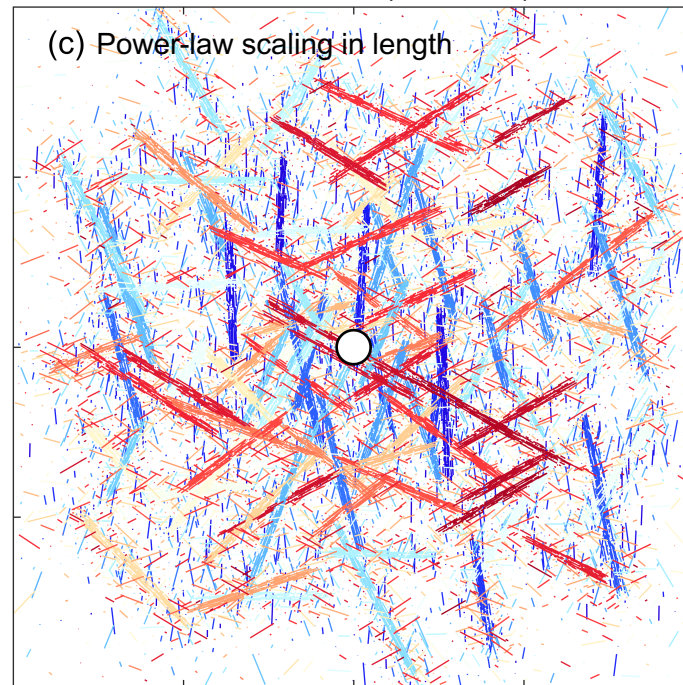
(a) Deterministic location & orientation



(b) Stochastic location & orientation



(c) Power-law scaling in length



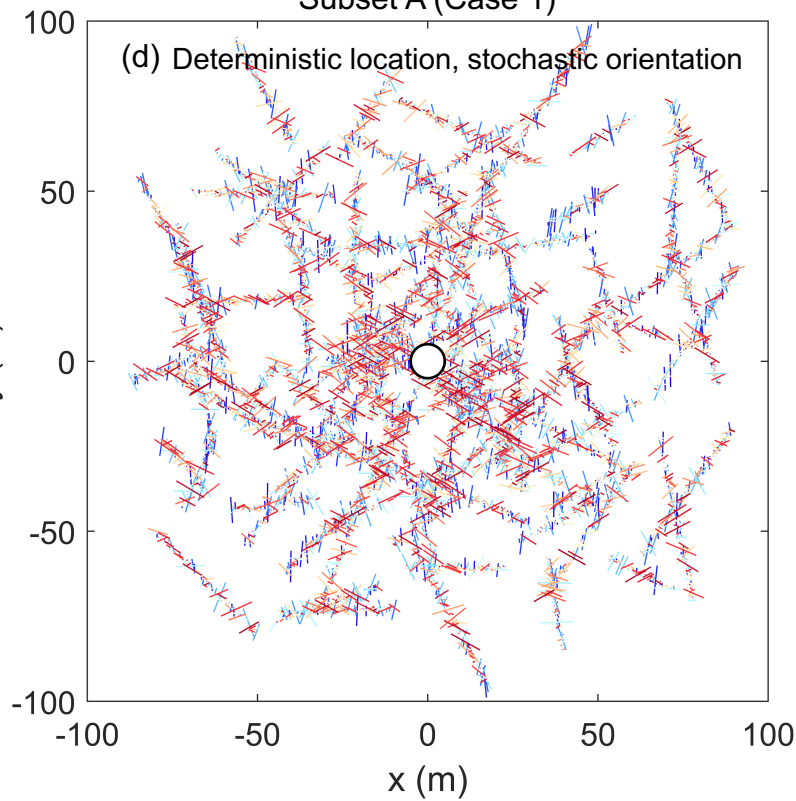
Subset A (Case 1)

Subset B (Case 1)

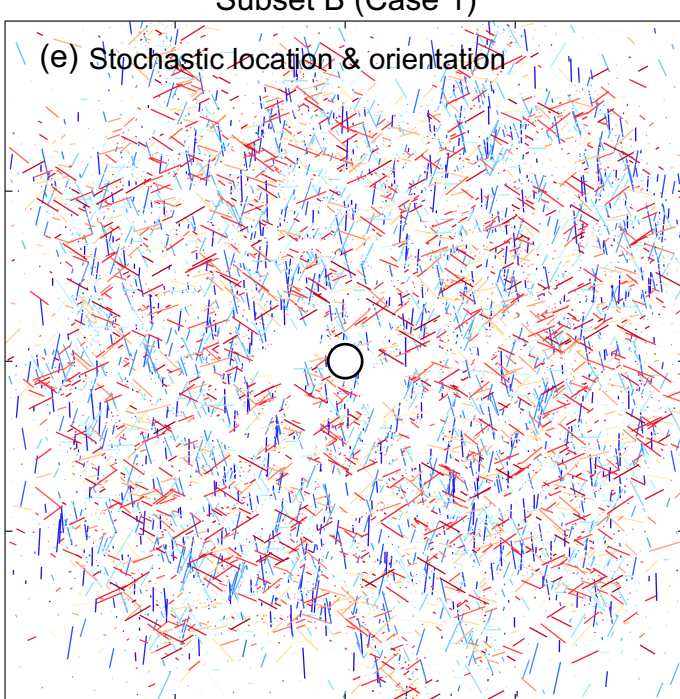
Subsets A & B (Case 1)

orientation

(d) Deterministic location, stochastic orientation



(e) Stochastic location & orientation



(f) Power-law scaling in length

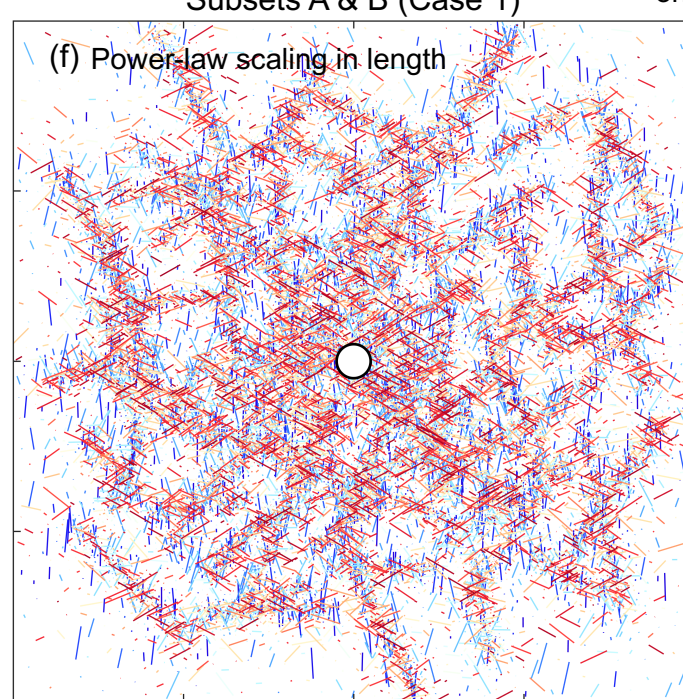


Figure 4.

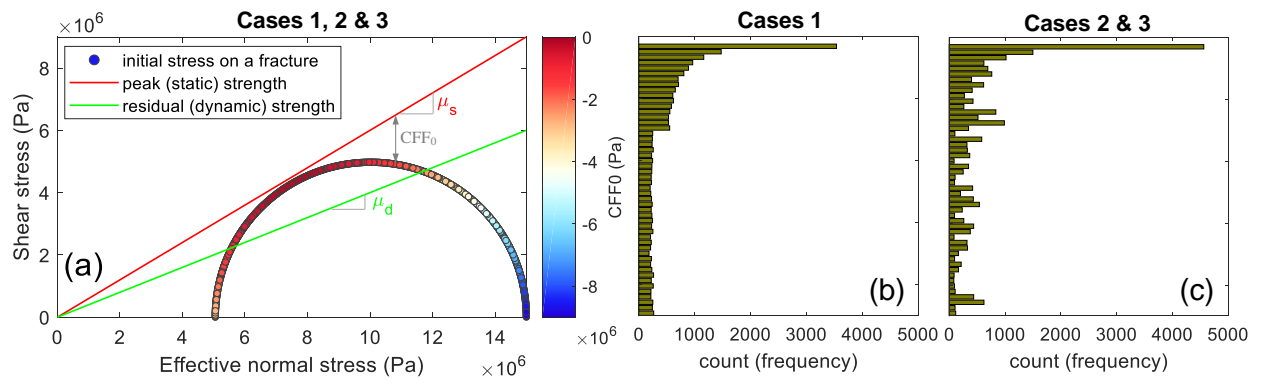


Figure 5.

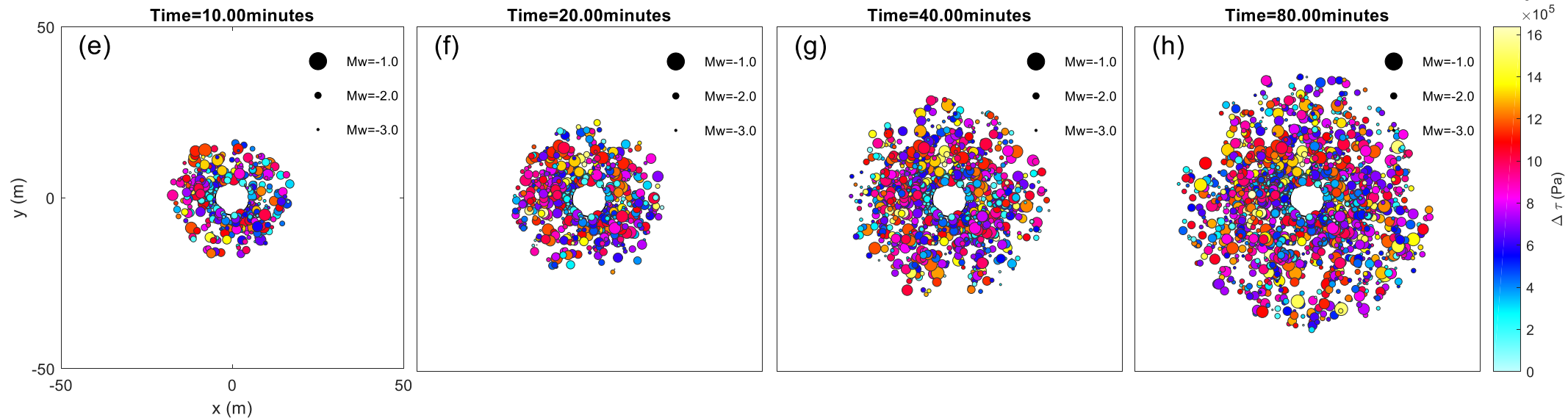
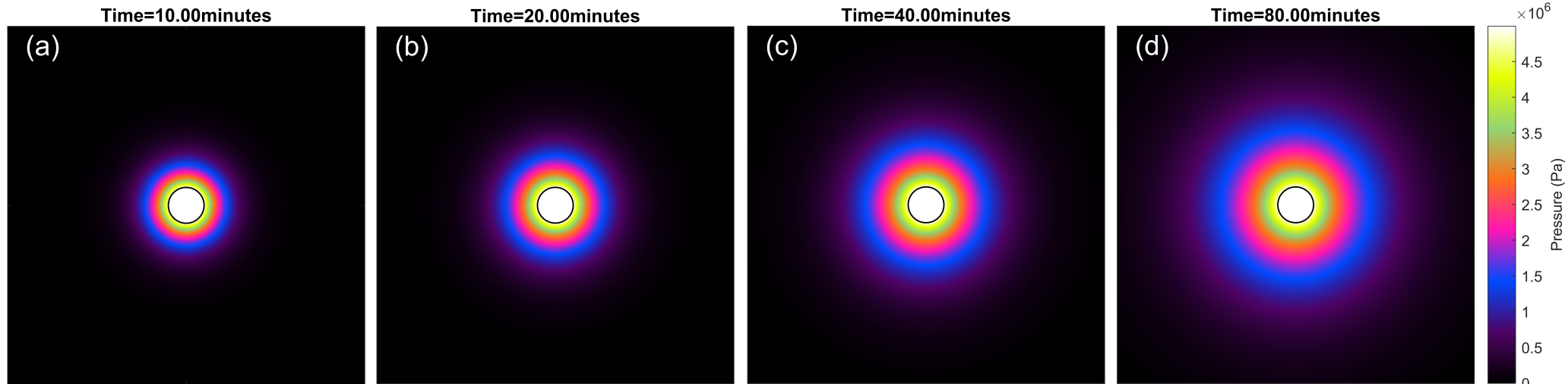


Figure 6.

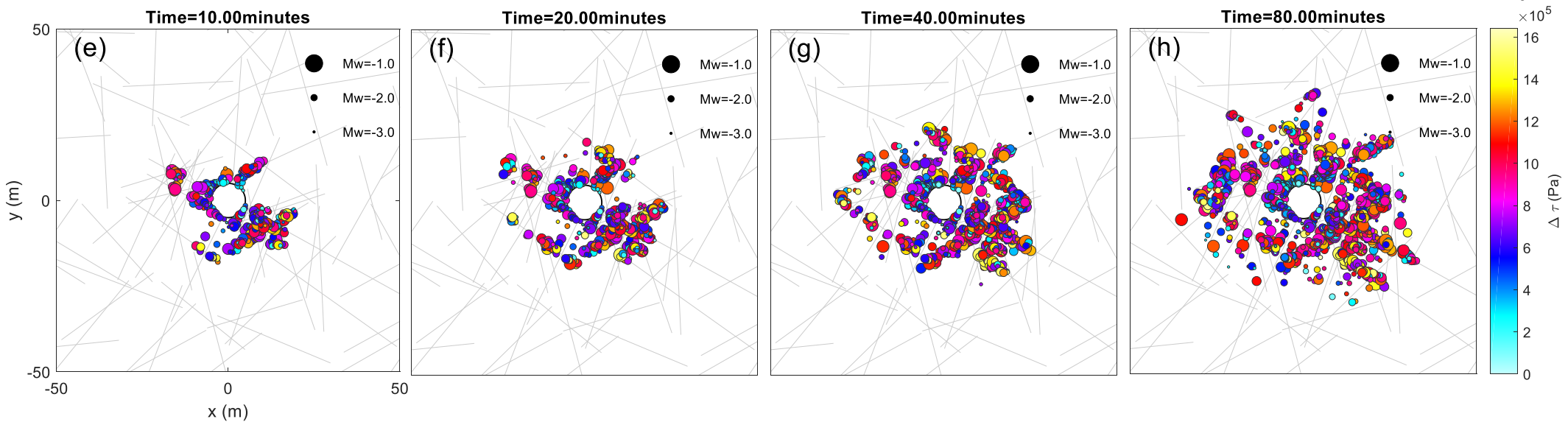
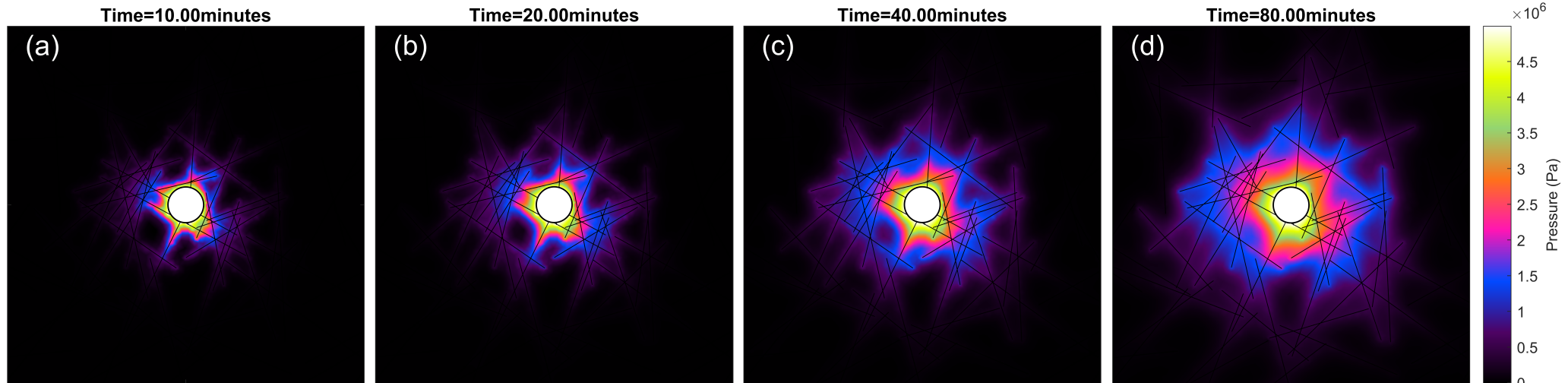


Figure 7.

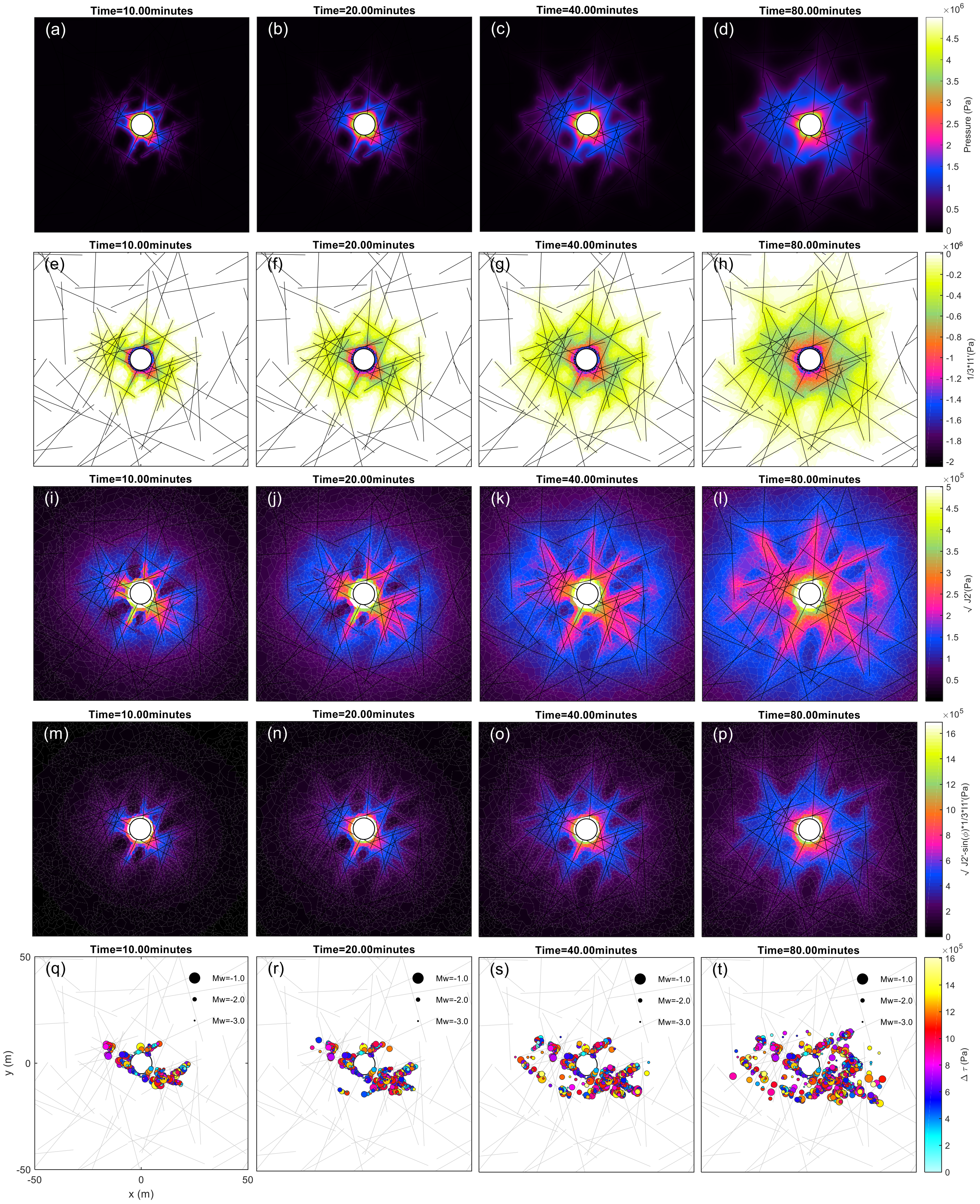


Figure 8.

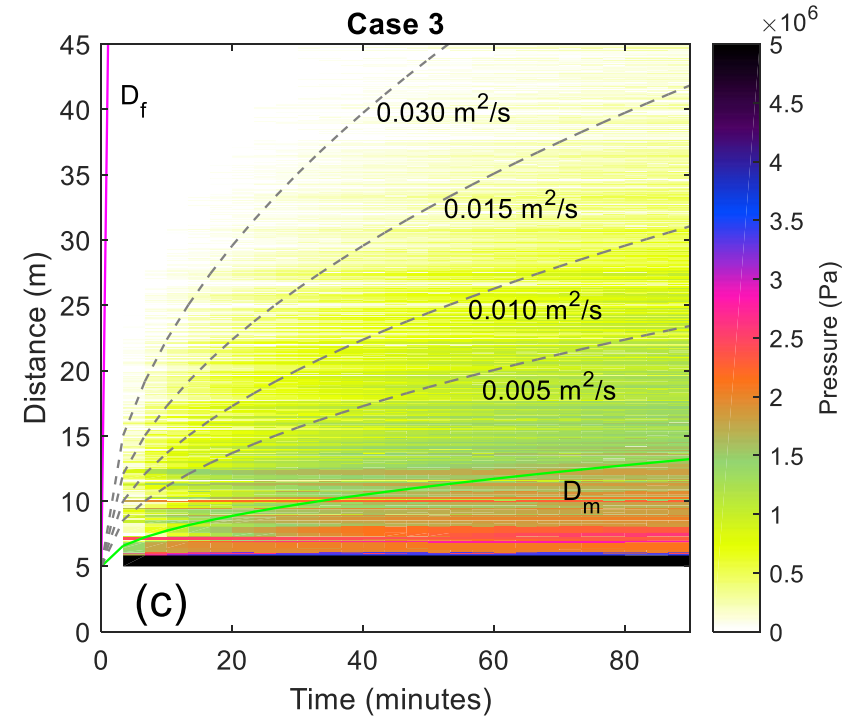
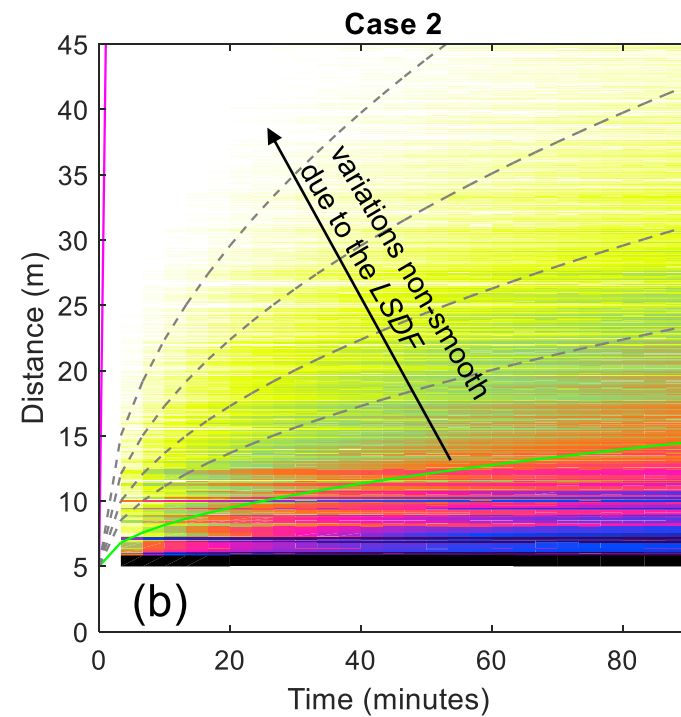
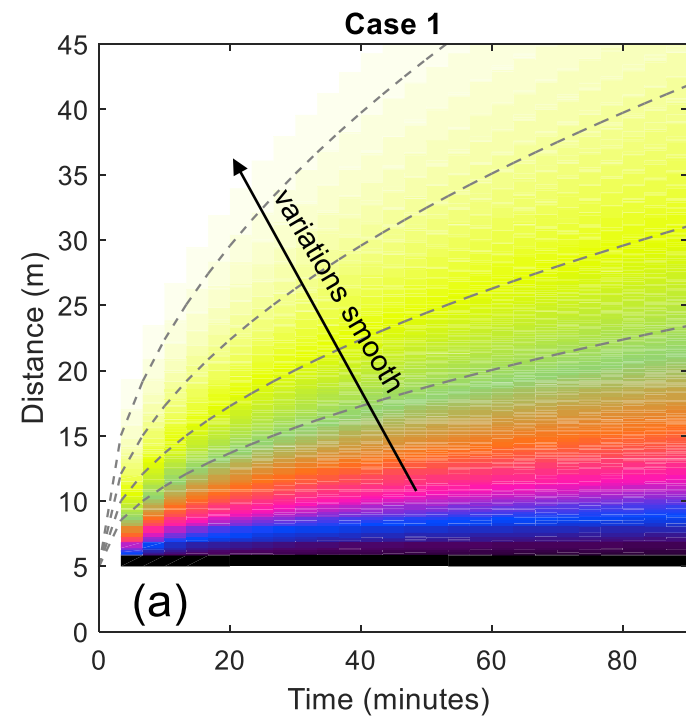


Figure 9.

Figure 10.

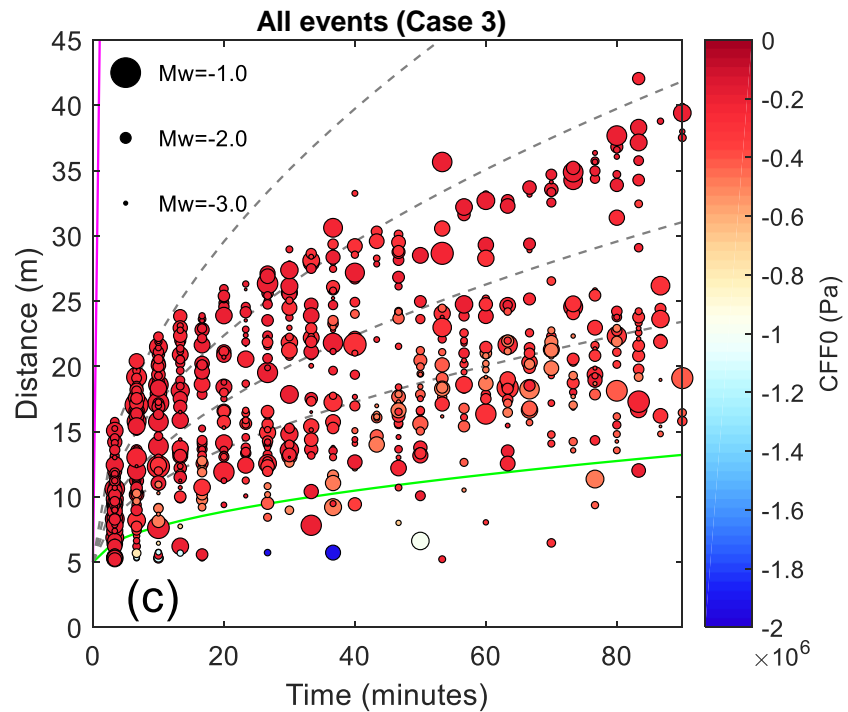
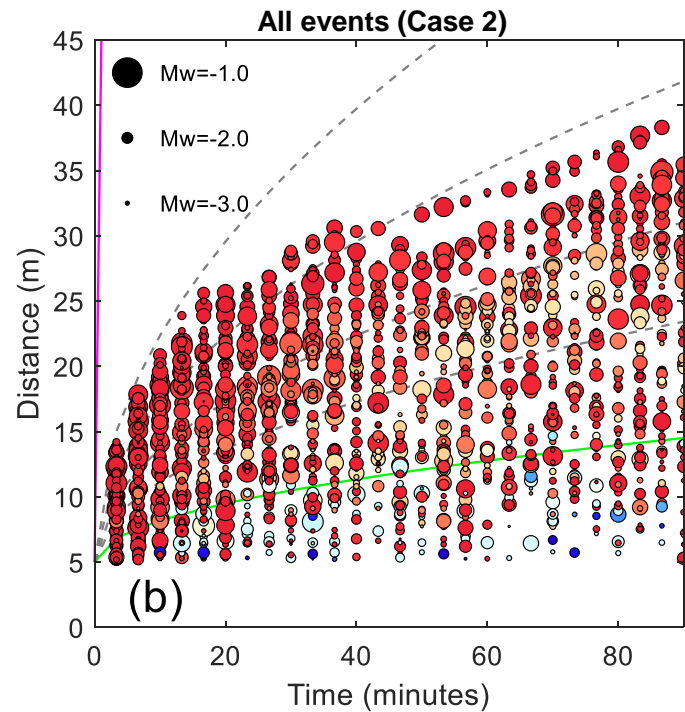
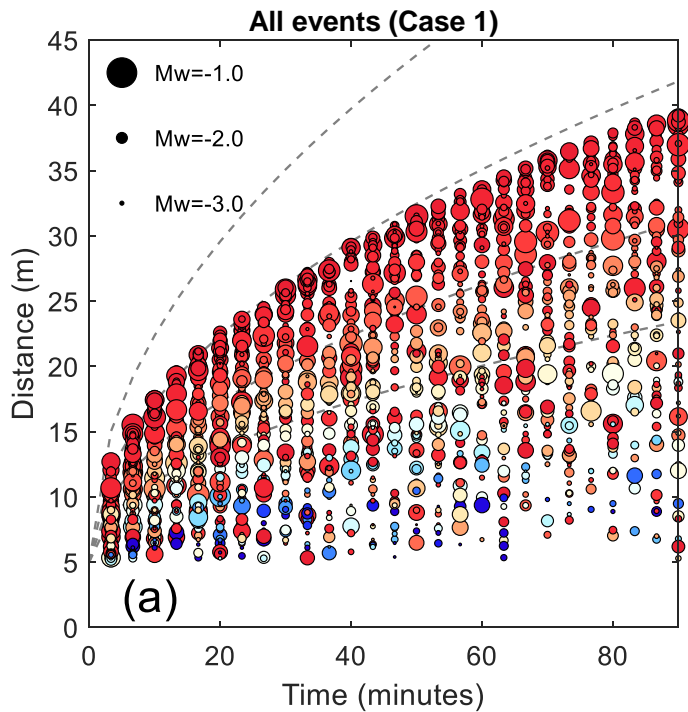


Figure 11.

Figure 12.

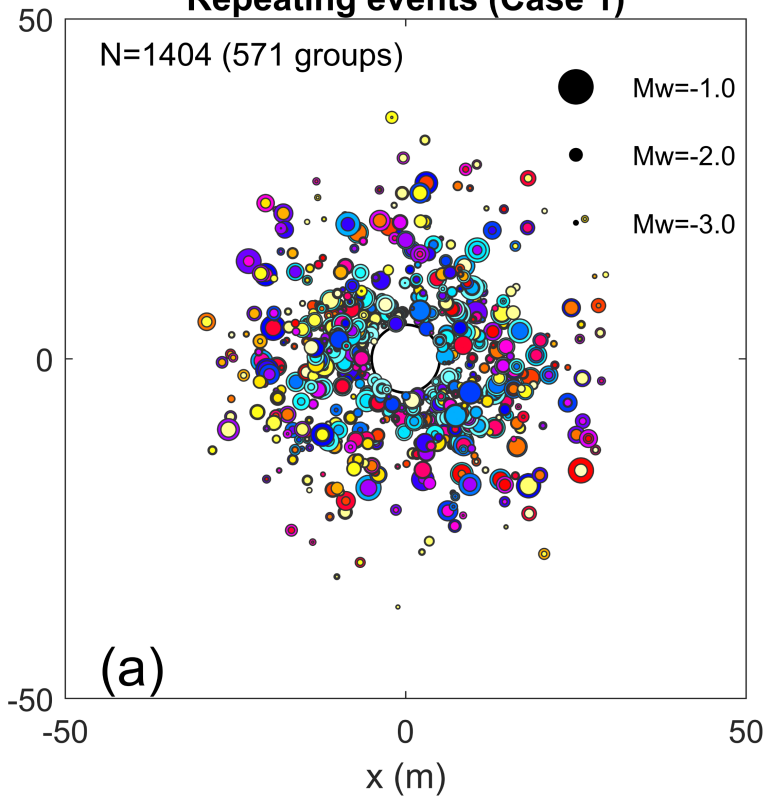
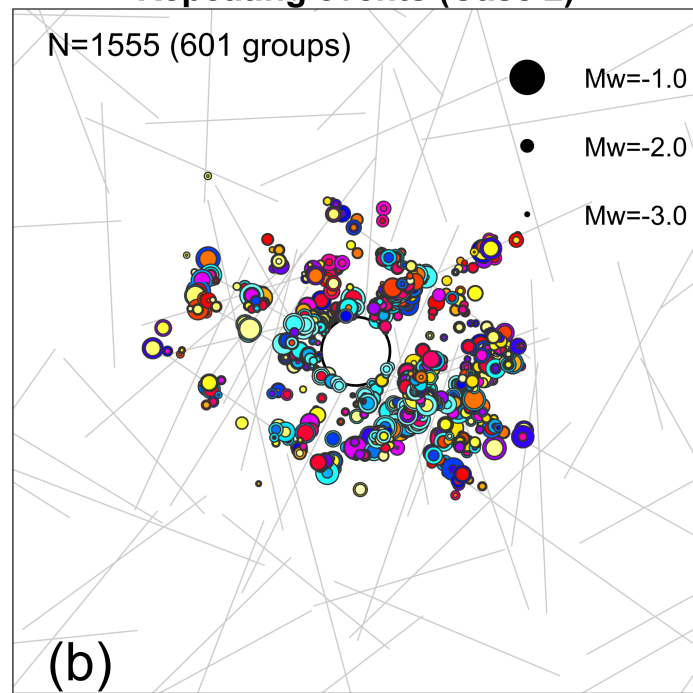
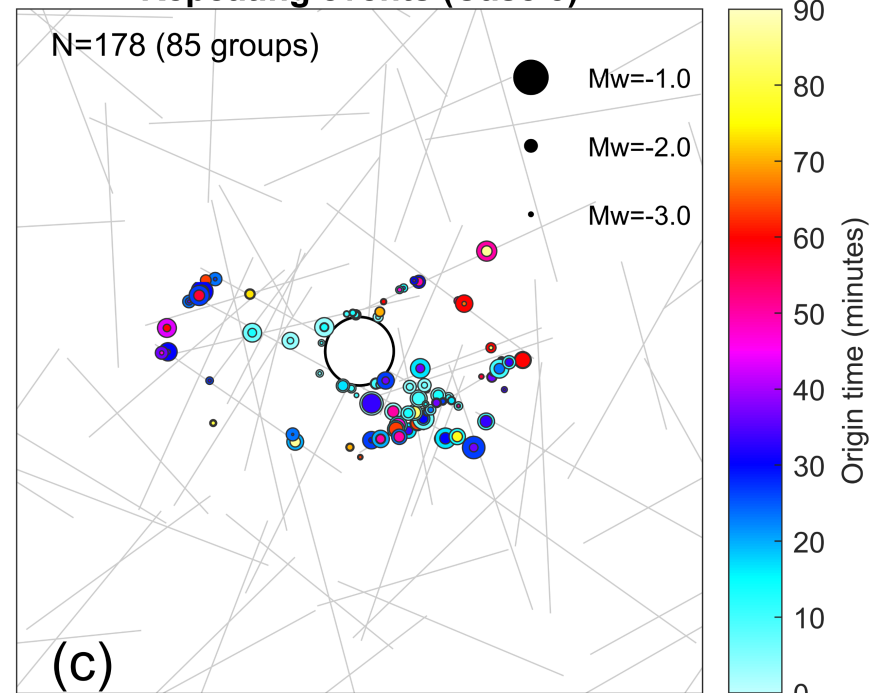
Repeating events (Case 1)**Repeating events (Case 2)****Repeating events (Case 3)**

Figure 13.

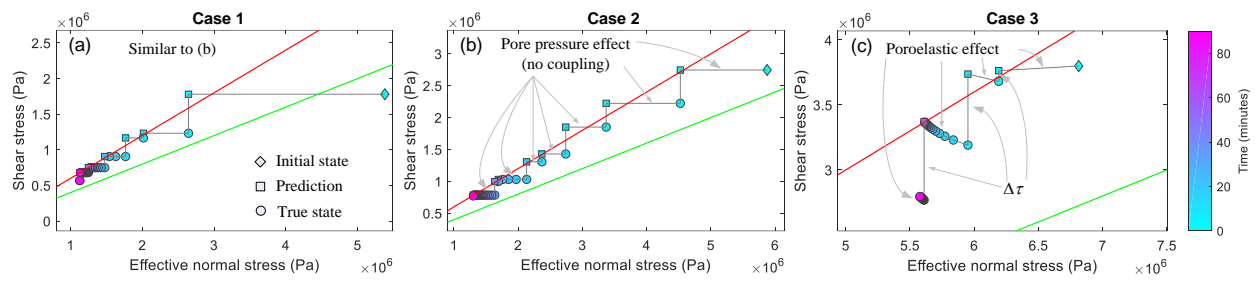


Figure 14.

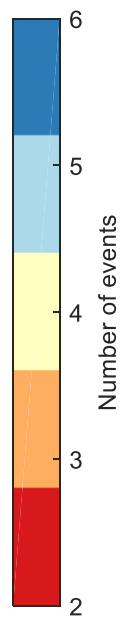
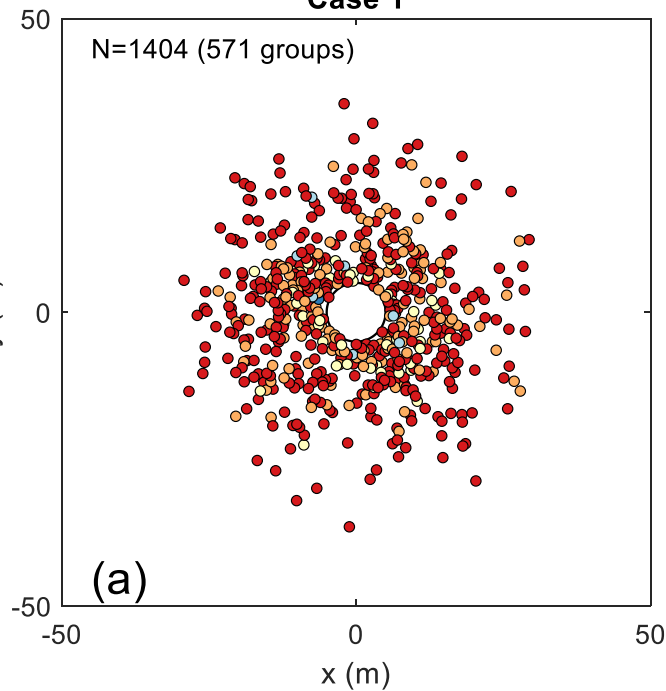
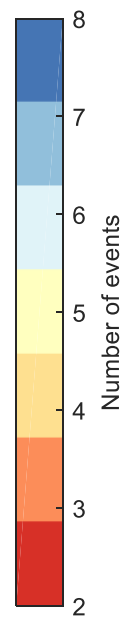
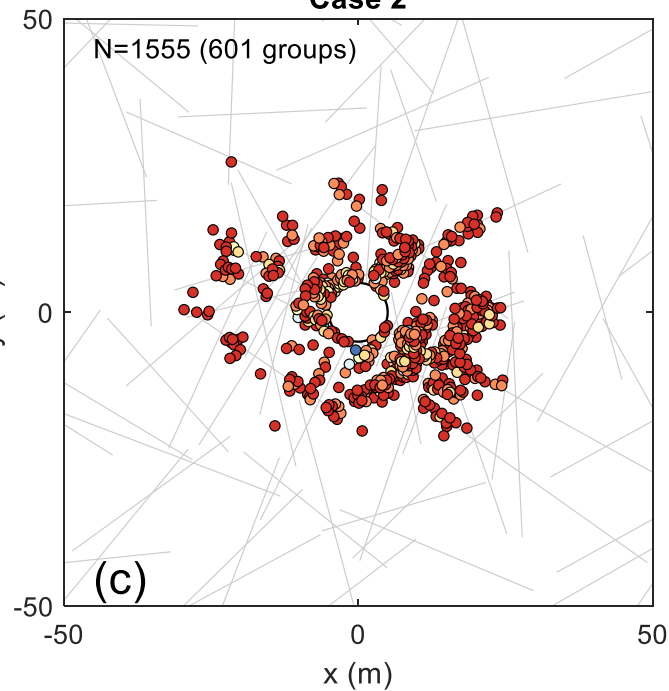
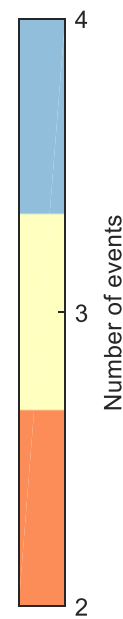
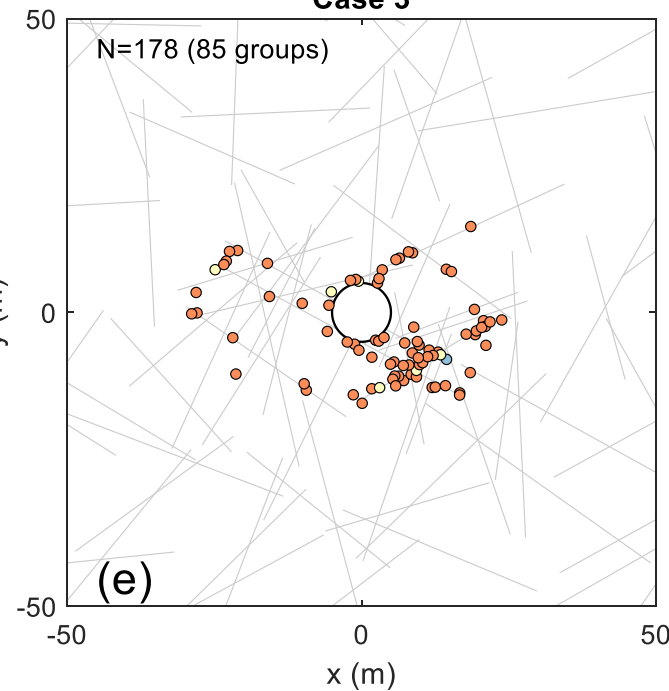
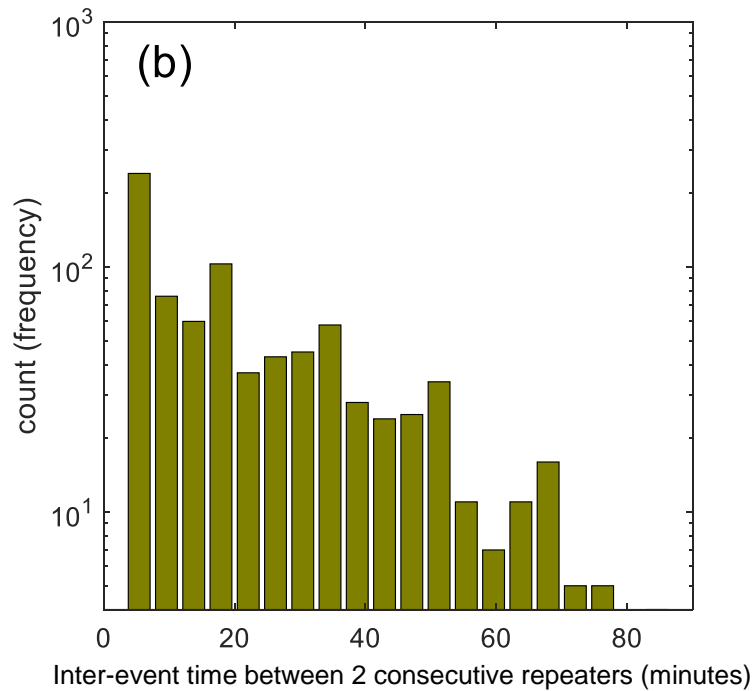
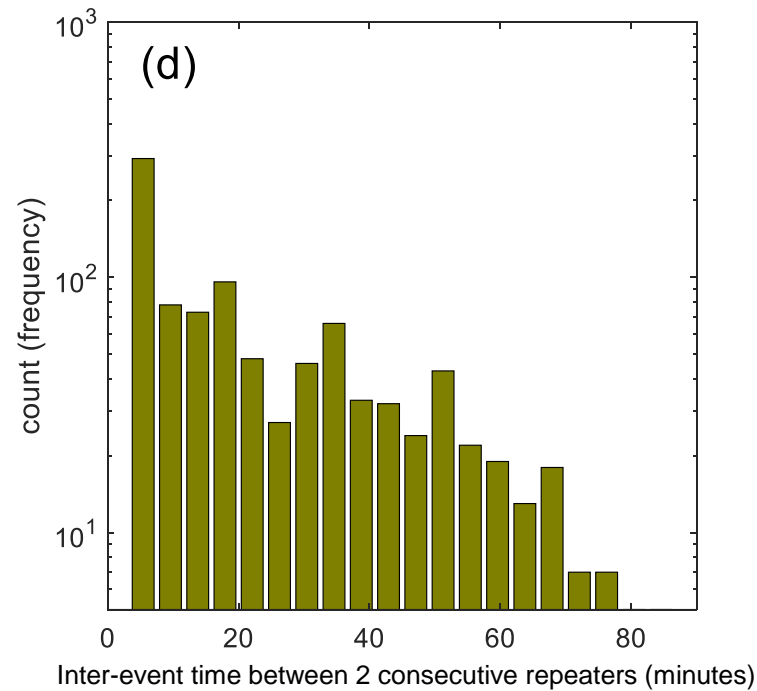
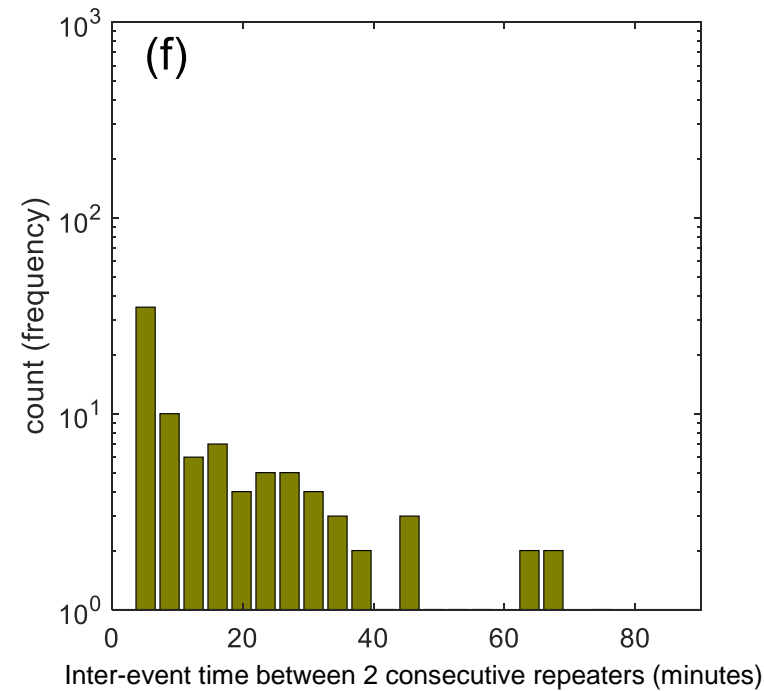
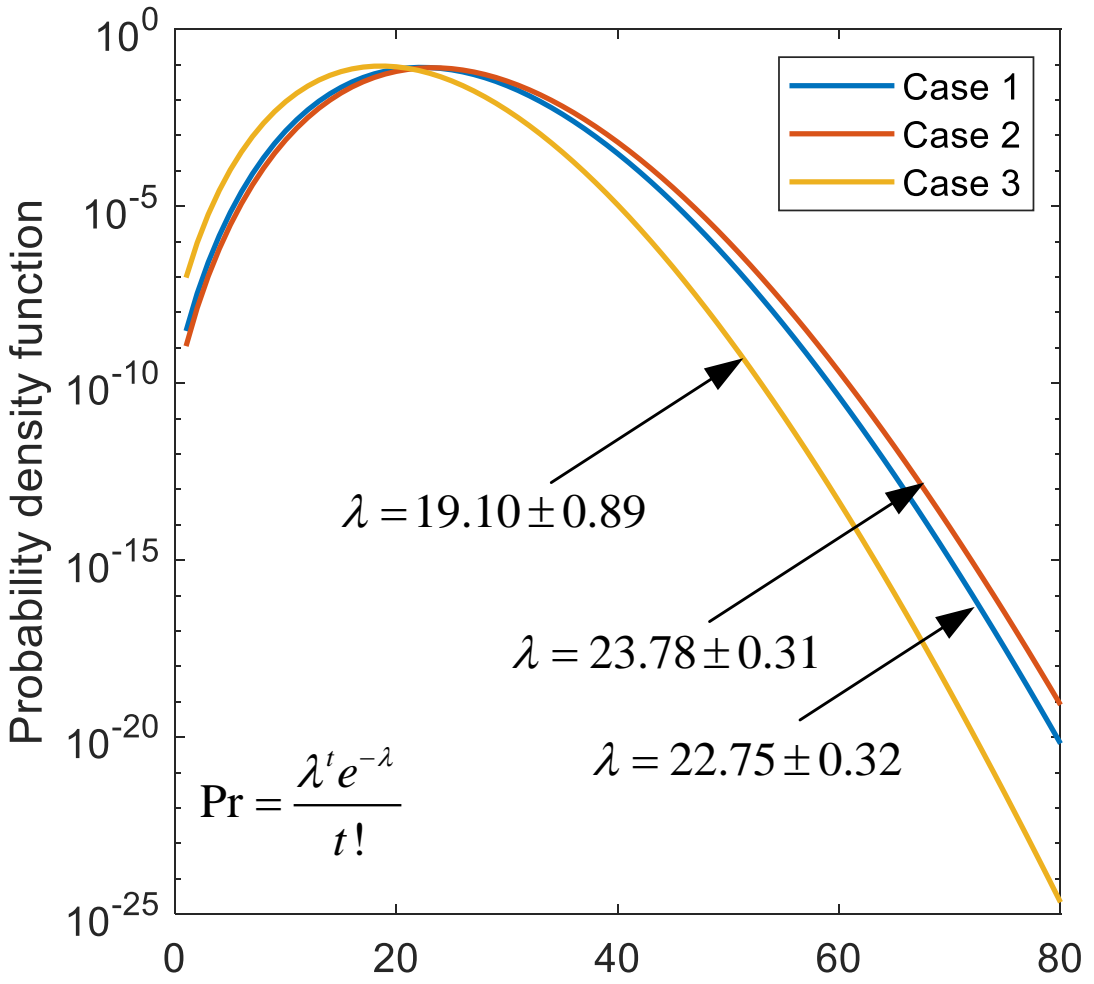
Case 1**Case 2****Case 3****(b)****(d)****(f)**

Figure 15.



Inter-event time between 2 consecutive repeaters (minutes)

Figure 16.

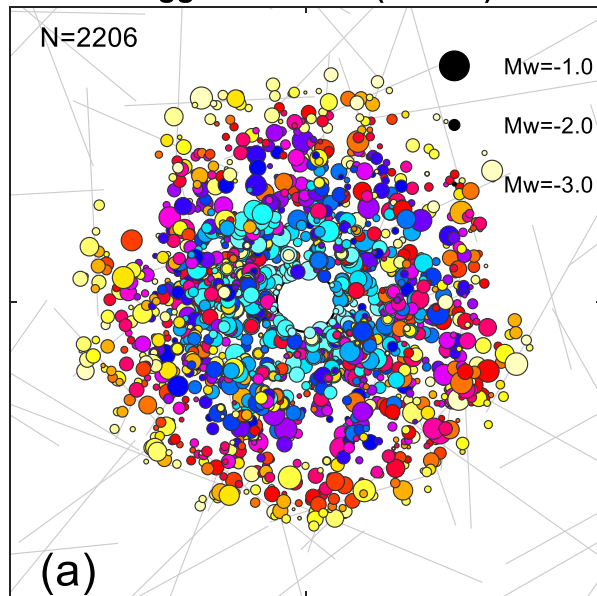
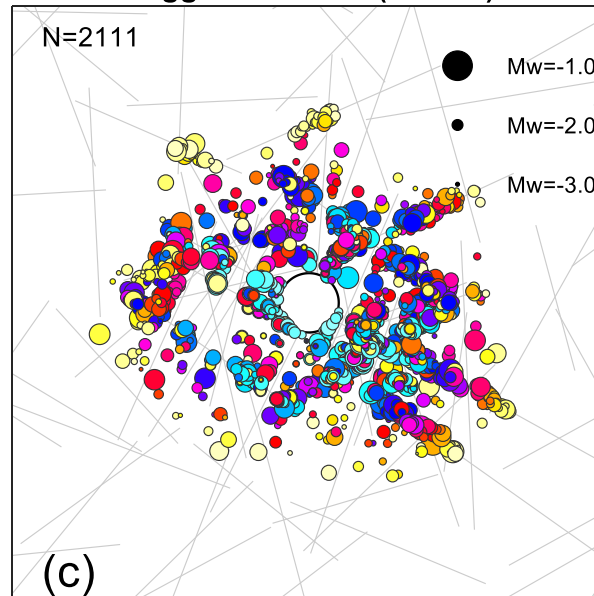
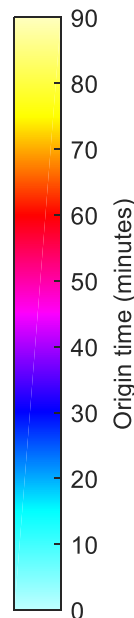
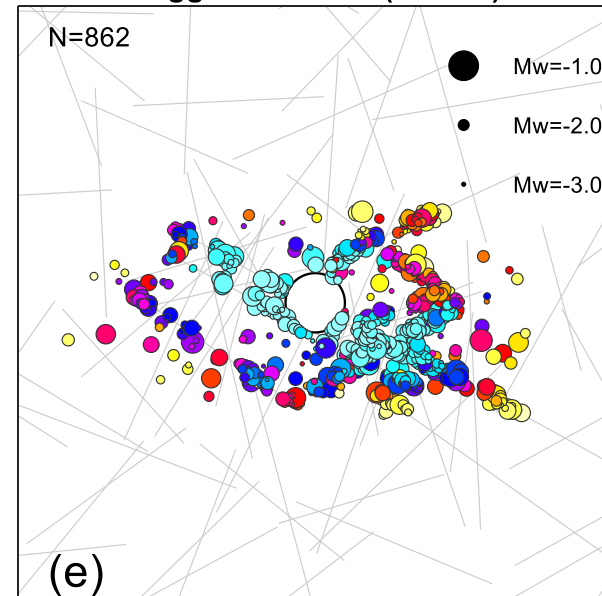
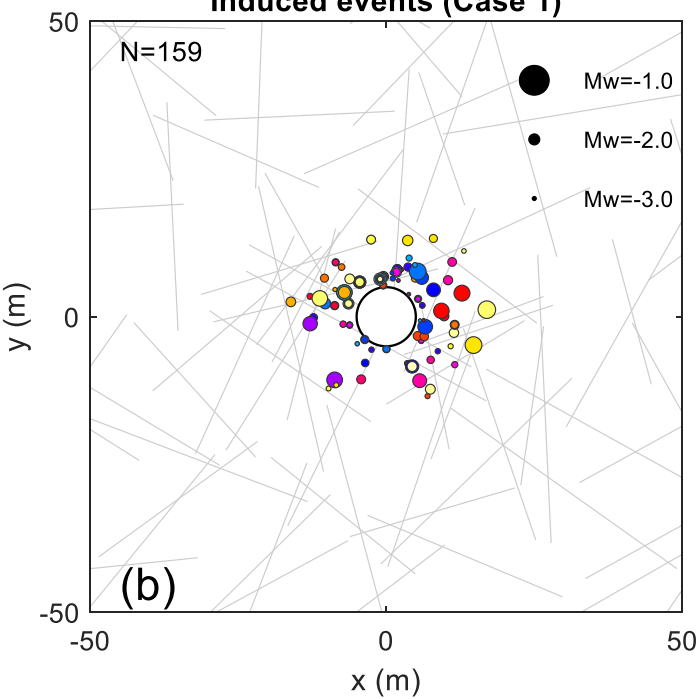
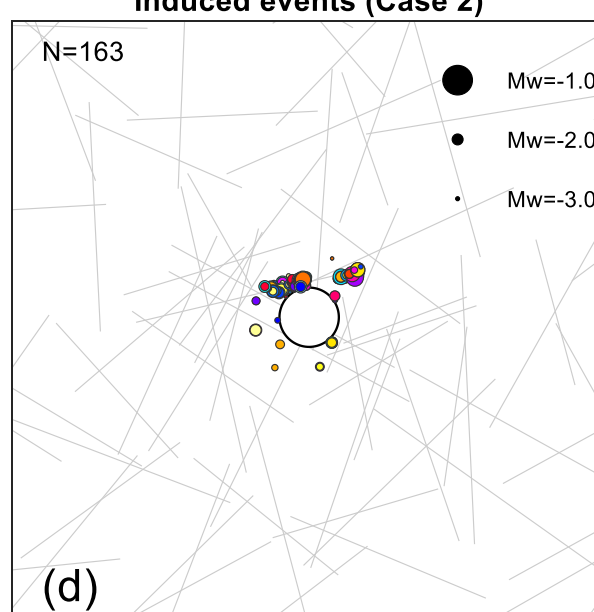
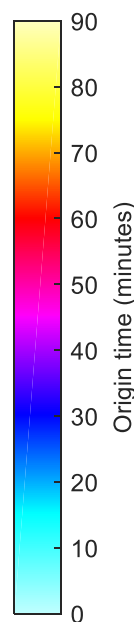
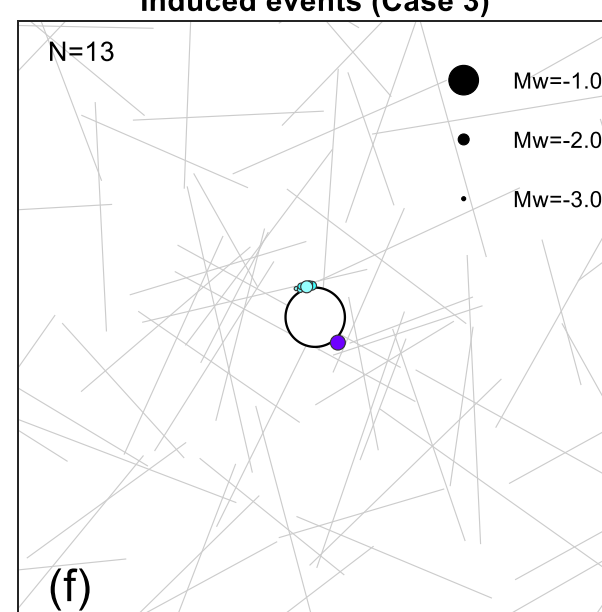
Triggered events (Case 1)**Triggered events (Case 2)****Triggered events (Case 3)****Induced events (Case 1)****Induced events (Case 2)****Induced events (Case 3)**

Figure 17.

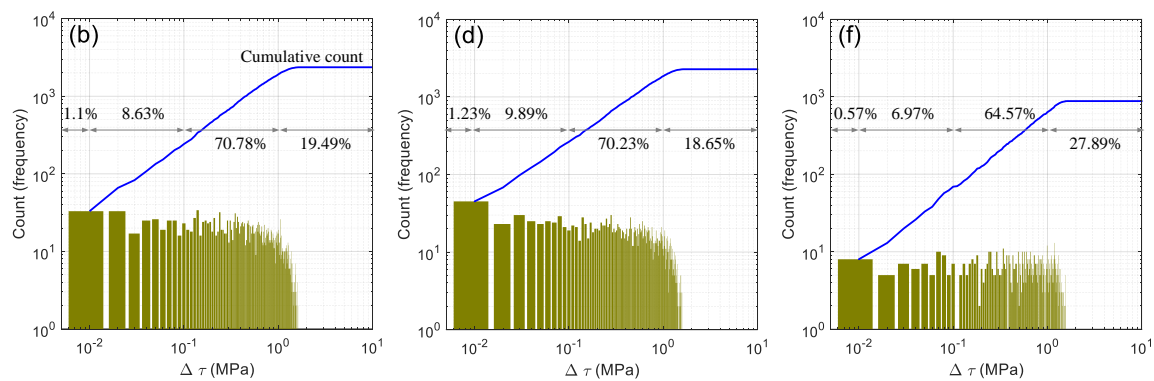
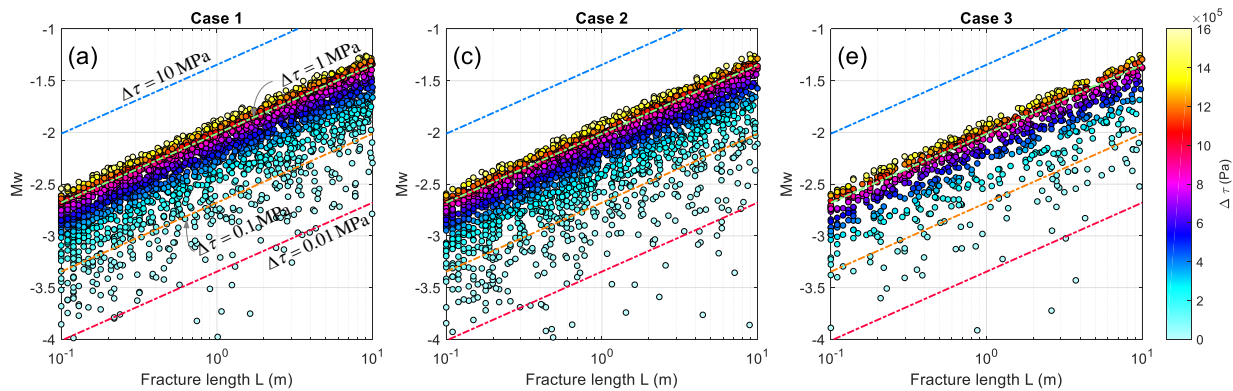


Figure 18.

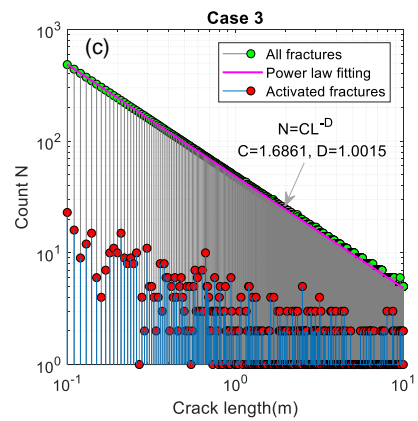
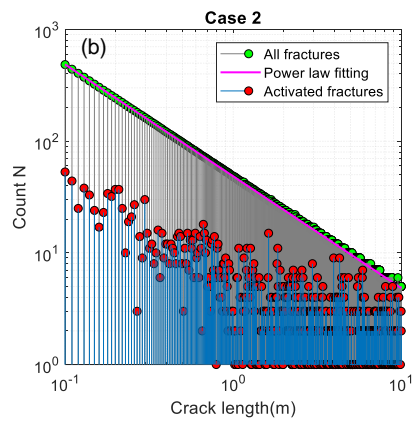
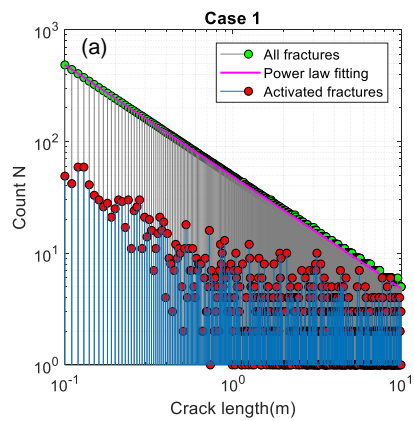


Figure 19.

